University of New Hampshire
University of New Hampshire Scholars' Repository

Master's Theses and Capstones   Student Scholarship

Winter 2008

The reduction of broadband crosstalk interference between multiple conductors in a backplane interconnect and its performance impact on gigabit digital communication signals

Prescott Brandon Atkinson
University of New Hampshire, Durham

Follow this and additional works at: https://scholars.unh.edu/thesis

THE REDUCTION OF BROADBAND CROSSTALK INTERFERENCE BETWEEN MULTIPLE

CONDUCTORS IN A BACKPLANE INTERCONNECT AND ITS PERFORMANCE IMPACT ON

GIGABIT DIGITAL COMMUNICATION SIGNALS

BY

PRESCOTT BRANDON ATKINSON

B.S.E.E., University of New Hampshire, December 2004

THESIS

Submitted to the University of New Hampshire

In Partial Fulfillment of

The Requirements for the Degree of

Master of Science

in

Electrical Engineering

December 2008

UMI Number: 1463209

INFORMATION TO USERS

The quality of this reproduction is dependent upon the quality of the copy submitted. Broken or indistinct print, colored or poor quality illustrations and photographs, print bleed-through, substandard margins, and improper alignment can adversely affect reproduction.
    In the unlikely event that the author did not send a complete manuscript and there are missing pages, these will be noted. Also, if unauthorized copyright material had to be removed, a note will indicate the deletion.

UMI®

This thesis has been examined and approved.

Kondapunte Swaprasad
Thesis Director, Dr. Kondagunta U. Sivaprasad
Professor of Electrical Engineering

Dr. Charles H. Bianchi
Affiliate Associate Professor of Electrical Engineering

Dr. Allen D. Drake
Associate Professor of Electrical Engineering

Mr. Mark W. Gailus
Principal Electrical Engineer, Amphenol TCS

Sept 4, 2008
Date

ACKNOWLEDGEMENTS

TABLE OF CONTENTS

LIST OF TABLES

LIST OF FIGURES

LIST OF ACRONYMS

3D – Three Dimensional

BER – Bit Error Ratio

FEXT – Far-End Crosstalk

FIM – Finite Integral Method

ICR – Insertion Loss-Crosstalk Ratio

MTL – Multiconductor Transmission Line

NEXT – Near-End Crosstalk

NRZ – Non Return to Zero

PCB – Printed Circuit Board

PSC – Peak Superposition Crosstalk

PSNEXT – Power-Sum Near-End Crosstalk

SMA – Subminiature Type-A Connector

SMT – Surface Mount Technology

SMTL – Stacked Microstrip Transmission Line

SOLT – Short-Open-Load-Through

TDR – Time Domain Reflectometry

TEM – Transverse Electromagnetic

VNA – Vector Network Analyser

XTLK - Crosstalk

ABSTRACT

THE REDUCTION OF BROADBAND CROSSTALK INTERFERENCE BETWEEN MULTIPLE

CONDUCTORS IN A BACKPLANE INTERCONNECT AND ITS PERFORMANCE IMPACT ON

GIGABIT DIGITAL COMMUNICATION SIGNALS

By

Prescott B. Atkinson

University of New Hampshire, December 2008

Crosstalk interference from signal transmission between transmission line conductors limits channel throughput as amplitude distortion in an experimental backplane connector. Shared return conductor microstrip connectors arranged in stacks have resonant frequencies that are determined largely by cavity dimensions of the return conductor geometries. If an input waveform to the connector excites these resonant frequencies, the resonant energy will couple to other signal conductors in the connector and will result in crosstalk interference. Lossy materials can be used to reduce the resonant crosstalk interference in connectors.

Quasi-conductor and magnetic absorber materials were used to reduce the resonant crosstalk in an experimental connector. Full-wave computer simulation was used to calculate connector S-parameters and was compared with measurement. Empirical equations were developed to relate experimental S-parameters of connector lossy material configurations with system bit-error-rate, channel Q, and eye pattern height at the data rate of 10.6Gbps.

CHAPTER I

INTRODUCTION

1.1 <u>System Background</u>

Currently baseband multi-gigabit digital information is often delivered across wireline transmission media such as printed circuit board (PCB) stripline and miniature high-bandwidth twinaxial cable discrete pairs. Computer hardware that relies on these wireline technologies includes internet backbones, high-capacity switches and routers, and supercomputers. These devices have numerous high-density, high-throughput transmission channels to communicate with their various subsystem components. The collection of these transmission channels implemented in PCB stripline is most commonly referred to as a backplane or motherboard.

PCB stripline has become the de facto standard digital data transportation medium for high-throughput wireline components in backplane systems. High density multilayer PCB stripline technology is fabricated with dozens of stacked and pressed layers of precision copper etchings over dielectric layers to create a backplane or motherboard. PCB stripline is used to carry data between silicon components of the backplane system. The delivery of serial data between silicon integrated circuitry and wireline transmission media such as PCB stripline and cable bundles occurs over a high-density interconnect system intermediary, or connector. The interconnect system should meet or exceed transmission and crosstalk interference specifications for the channel receiver when all components are cascaded in the passive channel.

1.2 Connector Subsystem

Typical PCB connector topologies include open pin field arrays, miniature parallel plate waveguides, high-density coplanar waveguides, and dense microstrips over large common plate return conductors. Board-to-board connectors can be designed for right-angle or mezzanine-type PCB orientations. High-density connector systems, such as these are typically composed of stamped sheet metal transmission line components, are either suspended inside of a large piece of injection-molded dielectric, or composed of smaller injection-molded dielectric wafers that are collected together by means of a shroud or metal organizer. All the above mentioned transmission line topologies are designed to support quasi-TEM modes of propagation. The great majority of these connector systems also include a separable interface to facilitate the periodic installation and removal of line cards in backplane systems and attachment of dense cable bundles. The stacked microstrip-type transmission line connectors mentioned previously shall heretofore be referred to as the stacked microstrip transmission line (SMTL) type, and are the focus of this study.

When considering connectors that are intended for attachment to multilayer PCBs, a transmission line structure known as a via, a hollow or solid metal cylinder that passes through many PCB layers, has become the most common channel used to deliver signals between the PCB stripline transmission lines of different backplane layers. If a PCB connector is designed with surface mount technology (SMT) in mind, then via diameters can be quite small, which is advantageous for impedance tuning to the target system transmission line impedance. If the connectors of an interconnect system are

2

designed to be attached to a PCB with press-fit technology, then the vias must have a plating inner diameter large enough to properly accept an individual connector press pin, and are therefore genereally larger than vias used for SMT interconnect systems.

As a result of using SMT and press-fit technology to attach connectors to PCBs with via signal feeds and return conductors, practical SMTL connector systems have discrete attachment geometries for maintaining a return path for signal transmission between PCBs. The use of discrete pin attachment to PCBs is the natural result of compromise between reliability and ease of attachment, and the cost of connector fabrication and board attachment processes. Gaps formed by discrete pin attachment of the SMTL connector return conductors can allow leakage fields from signal transmission into the imperfect resonators formed by adjacent SMTL shield conductors. A result of these imperfect resonators is resonant crosstalk interference between signal lines, and in practice these types of resonances generally occur above 1GHz. EMI problems from poorly shielded cable connectors pose a problem similar to resonant SMTL return path structures, in that leakage currents are responsible for interference. The imperfect attachment of SMTL connector return conductors, if not studied and anticipated, can create impairments in the integrity of the transmitted signal and undesirable crosstalk interference from neighbouring transmission lines. Similarly, the separable interface nature of practical SMTL connectors can also be a source of signal energy leakage, setting up conditions for channel throughput impairment in the form of crosstalk. In the case of the SMTL, the effective cavity dimensions of the transmission line return current conductors largely determine certain resonant crosstalk interference characteristics.

3

1.3 Description of Study

This thesis considers a structure which is a simplified scale model SMTL PCB

connector with plate return conductors attached to the launch return conductor of multiple

SMTL transmission line feeds. The two launch return conductors at either end of the

SMTL connector act as simple PCB surface ground planes. An illustration of an SMTL

structure is shown in Figure 1.
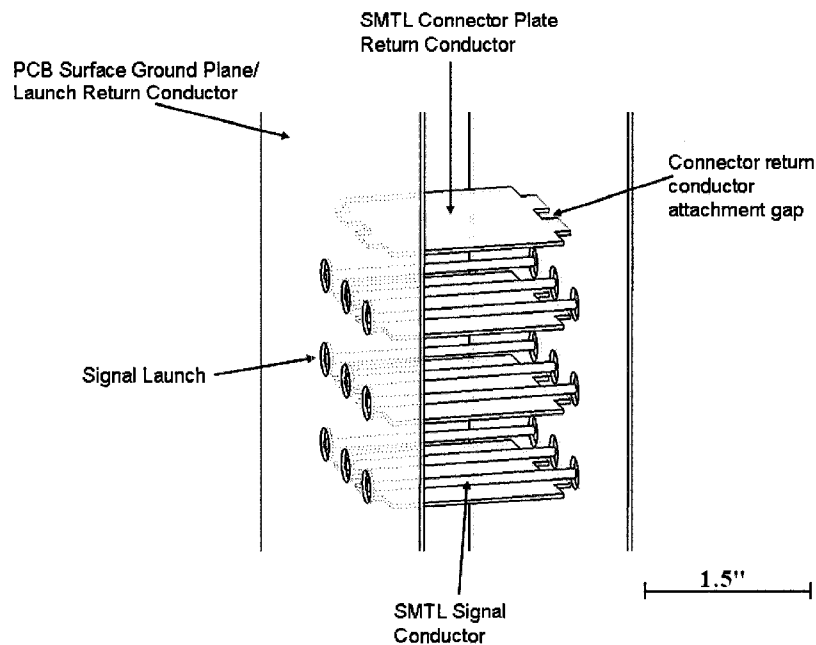
Figure 1: Illustration of a hypothetical shielded PCB-to-PCB connector.

Gaps where the connector return conductors attach to the launch PCB ground

planes will allow for significant resonant crosstalk interference between transmission

lines in the SMTL connector. The structure return conductors act like imperfect

resonators in the bandwidth of interest, 0 - 10GHz, where resonant energy couples to

signal conductors in the structure cavities. The resonance frequencies are associated with

the electrical length of the structure transmission lines. Individual transmission lines in

the structure will have a similar propagation delay to existing commercial SMTL

connectors and will therefore have similar resonant crosstalk characteristics in the 0 - 10GHz frequency range, which can be excited by signal transmission. The crosstalk interference and transmission characteristics of a baseline SMTL will be presented in the form of scattering matrix elements from computer simulation and will be compared with the results obtained from measurements of the physical fixture. The baseline fixture consists of signal conductors and bare plate return conductors with air dielectric. The effect of cumulative resonant crosstalk on a transmission channel will be analysed to understand its effect on limiting the channel performance.

One of the ways to reduce the effect of crosstalk interference from neighbour lines on the transmit channel is to attenuate unwanted resonant crosstalk frequencies in SMTL connectors by the use of lossy materials. Lossy materials having a broad range of properties may be used in connector applications, as illustrated by the ideas enumerated in U.S. Patent 6786771, granted to Gailus[1] and held by Amphenol Corporation. However, in the literature there is no study available to determine the choice of lossy material to be used in a connector application that will be effective and will perform adequately for an SMTL application.

In particular, the focus of this thesis is studying the phenomenon of resonant crosstalk as an impairment to channel throughput, and the mitigation of this impairment using lossy material. The sources of interference from multiconductor transmission line (MTL) crosstalk will not be considered as they are much less in magnitude than the resonant crosstalk. This thesis seeks to examine the usage of lossy material slabs of various quantified electromagnetic constitutive parameters at a uniform material thickness in an SMTL connector, with the purpose of reducing resonant crosstalk

interference. The suppression study will be accomplished by affixing a lossy material

slab to a conductor face in each of the experimental connector structure return conductor

cavities. The thesis will also study the characterisation of materials with various physical

loss mechanisms and constitutive parameters, and will model them in the experimental

connector platform with full-wave 3D simulation so as to find agreement between

modeled and known material constitutive parameters.

1.4 Review & Literature

1.4.1. Lossy Material Review

Two types of lossy material will be examined within the thesis for the purpose of

reducing the resonant crosstalk in a connector. Both types of lossy material consist of an

insulator plastic called the material matrix, in which microscopic lossy material particles

are distributed homogenously on the macroscopic scale.

The first type of materials that will be examined is filled with varying percentages

of highly conductive material. The filler in this type of material may be either

nonmagnetic or magnetic. These materials support eddy currents or enhance conductor

loss. The physical process of loss for this class of material is known as metallic

conduction loss.

The second type of material consists of nonconductive filler compounds that have

ferromagnetic loss properties. These materials have loss characteristics that are often

highly frequency-dependent. The physical loss process of this class of material is

dominated by magnetic alignment-relaxation loss and to a lesser extent material electric

dipole loss.

The conductive lossy materials examined in the thesis have very conductive filler materials, carbon or nickel, where nickel has significant ferromagnetic properties and carbon does not. The range of conductivity examined in the conductive type of material covers 1.5 S/m through 1500 S/m bulk conductivity. Conductor-insulator mixtures can be characterised as lossy dielectrics where the effective relative dielectric constant and loss tangent of a mixture are determined by a physical model. Factors such as assumed conductor particle geometry, percentage volume concentration, and uniform particle distribution are incorporated into these models. Rothwell[2] compares several such physical models, and shows how the various models diverge as the material bulk conductivity increases. Youngs[3] presents a physical model for so-called artificial dielectrics and compares the model to measurement data. A specific limitation to the model presented by Youngs is that the accuracy of the loss model diverges from measurement data as the dielectric is doped with higher concentrations of conductor particles. If ferromagnetic metals are used as the conductor particles in an artificial dielectric, then the effective dielectric loss tangent of the mixture will be enhanced by magnetic relaxation dissipation. Gurevich[4] is a resource that can explain the process of magnetic relaxation dissipation in pure metallic materials, which were used in one of the experimental materials of this study. Lederer et al.[5] presents a model to separate the magnetic loss process effects and conductor eddy current loss effects for artificial dielectrics composed of magnetic conductor particles and insulators, of similar composition to a material sample examined in this study.

The nonconductive class of lossy materials examined in this thesis is of a similar physical filler distribution to the conductive class, except that the filler is a high

performance ferrite powder. Ferrites such as these are generally soft ferrite material. Kasap[6] provides a general description of soft ferrite materials. Soft ferrite material has minimal remnant magnetisation when a strong DC magnetic field bias to the material has been applied and removed. The application of a strong magnetic field to the nonconductive magnetic materials in this thesis experimentally determined that these materials could be assumed to be a soft ferrite since they did not exhibit physical force attraction to unmagnetised iron slugs. Baden Fuller[7] and von Aulock et al[8] both describe low bias field ferrite loss, the magnetic loss process of this class of material in the microwave frequency regime. This dominant loss process can be, to a first approximation, modeled by the Landau-Lifshitz equation. The Landau-Lifshitz equation is well-described by Gurevich[9]. In his classic publication on dielectrics, Von Hipple[10] describes the less significant physical process of dielectric loss in this type of material.

1.4.2. Crosstalk Interference Problem

A review of topics in the literature is necessary for understanding the importance of crosstalk and undesirable resonance as impairments to the performance of a connector as a digital communication channel. A comprehensive text concerning MTL coupling by Paul[11] is suggested reading for thorough understanding of the subject. A majority of topics in the literature concerning crosstalk are problems that analyse MTL crosstalk, where coupling coefficients are determined from the per-unit-length matrix parameters of the particular transmission line conductor geometries in uniform cross-section. For signaling frequencies below 5GHz, Gailus et al.[12] have shown that 2-D cross-sectional characteristics from successive length partitions of non-uniform MTL connector systems

8

can be cascaded, and can provide good agreement with measured crosstalk data of the connector. This process is often referred to as 2½-D modeling of connectors. Limitations of the so-called 2½-D approach for connector models become apparent between 2GHz and 5GHz when the electrical length of the connector subsystem approaches the order of the operational frequency wavelength, and so this method is not sufficient to characterize the high frequency performance of connectors. A numerical full-wave 3-D solution for a multiport connector system then becomes necessary to accurately model throughput performance at higher frequencies and quantify crosstalk characteristics of a connector system. Some of these crosstalk characteristics in connectors are of the resonant phenomenon type considered in this thesis. Various methodologies have been implemented in software to create a baseband, full-wave electromagnetic numerical solution that can be applied to cascaded circuit models of multiport connector systems. Some methods described in the literature for full-wave modeling include the treatment of the Time-Domain Finite Integral Method (FIM) by Jiao et al.[13] and Ulrich[14], the Finite Element Method Frequency-Domain (FEM) by Pantic et al.[15], and the Finite Difference Time Domain Method (FDTD) by Lo Vetri et al.[16].

MTL crosstalk as a source of digital communication channel interference has been studied for specific configurations in the literature. Stripline transmission lines located between the power and ground planes in a PCB are modeled by Engen et al.[17]. This paper uses a technique based on MTL theory to separate the TEM modes of propagation along the striplines and the parallel plate waveguide TEM propagation modes of the split reference power and ground planes, which are also return conductors for the stripline. The paper is relevant to this thesis since it quantifies coupling or

crosstalk between the TEM modes of the stripline and the split reference parallel plate waveguide of the PCB. The technique can be used to investigate and model the conversion between stripline and parallel plate TEM modes of propagation at return path discontinuities. Because the paper discusses a theory just to model coupling between the stripline and parallel plate modes, it does not discuss methods to reduce or mitigate this undesirable coupling.

Some studies deal with the loading or termination schemes of particular uniform MTL geometries. Broydé et al[18] deal with true matching of all MTL modes in a MTL system of n+1 conductors by adjusting transmitter, receiver, and termination characteristics appropriately to suppress crosstalk and echo. The viability of this technique is demonstrated in SPICE. This is a unified approach for the determination of ideal transmitter system components with a perfect ground return conductor, but does not consider the mitigation of resonant crosstalk.

In a study on MTL crosstalk reduction, Ciamulski et al[19] minimizes MTL crosstalk in an arbitrary interconnect system with termination and source networks. While it is a study concerning crosstalk reduction, this study is not appropriate for our application since it deals with direct-coupled crosstalk rather than resonant crosstalk.

Another study by Kim et al.[20] demonstrates the use of an embedded capacitance in the PCB footprint of a CAT-5E modular jack to reduce 100MHz near-end crosstalk in unshielded twisted pair transmission line cable bundles. The capacitive coupling in the untwisted length of this connector was accomplished by augmenting the capacitance in the connector PCB footprint to balance intrinsic connector mutual capacitances in the modular connector. While this study concerns the reduction of crosstalk, it pertains only

to the reduction of relatively low frequency crosstalk in the untwisted segment of transmission line in a CAT-5E modular connector using MTL analysis.

A simple model of resonance in multi-layer PCBs has been documented by Tarvainenn[21] using structure dimensions and dielectric material properties. This paper demonstrates that guard vias used to minimise coupling between signal vias in a PCB can be rendered ineffective if the cavity formed by parallel plate return conductor structures of the PCB is resonant. In other words, this paper demonstrates that a PCB resonant ground system can act as a mechanism for crosstalk interference between distant signal conductors on a PCB. The paper focuses on characterizing resonances due to the return conductors of the PCB, but does not suggest methods to reduce this resonant behaviour.

Goergieva et al.[22] discusses PCB structures such as the large split-ground plane and PCB shielding covers, and their influence on digital system performance and signal transmission in the form of resonant crosstalk that can couple to various signal lines. This paper investigates numerical modeling of resonant crosstalk for two specific PCB scenarios, but also does not examine the reduction of this resonant crosstalk.

Yuasa et al.[23] have addressed the suppression of resonance in PCB parallel plane return conductor structures by efficiently using stitching via patterns to remove unwanted resonance. This approach of using shorting conductors to mitigate cavity resonance is seen as impractical for a shielded connector application since the cost of implementing shorting conductors in practice is prohibitive and somewhat difficult.

1.4.3. Communication System Performance

The performance of a connector channel transmitting baseband digital information can be characterized from the statistical distribution of voltage states. One measure of communication system performance is the bit-error-ratio (BER). If the statistical distributions of the digital voltage states in the time domain have Gaussian characteristics, the BER of a channel can easily be determined [Couch[24]], provided the input signal has identical characteristics for rising and falling edges. Q is another measure of the channel performance [Derickson[25]], and can be used also to approximately calculate the channel BER. Frequency domain characteristics of a communication channel may also be used to determine channel performance. To determine if a 10Gbps channel has a BER less than 10^{-12}, IEEE[26] developed an empirical formula derived from experiment, which uses insertion loss and crosstalk magnitude spectral characteristics.

In summary, Chapter 1 discussed background information concerning how data are transmitted between PCBs through the connectors, different types of quasi-TEM PCB connector waveguides, and provided a high-level description of the simplified experiment that is performed to study the role of lossy materials in reducing resonant crosstalk in an SMTL connector. The chapter also summarized different lossy materials that are used as a variable in the experiments and how existing studies from the literature relate to this thesis.

CHAPTER II

COVERED MICROSTRIP RETURN CONDUCTOR RESONANCE

In practical applications where microstrip signal conductors share common return conductors as is the case in PCB-to-PCB connectors, signal transmission may excite resonance in the connector return conductor geometries. A result of this resonance is resonant crosstalk, which can degrade the performance of transmission lines in a digital communication system such as a connector. For example, Taravainen (2000) shows resonant crosstalk levels of about -15dB of coupling between terminated pass-through vias spaced 60mm apart on a thin PCB with multiple ground planes in the 0-10GHz frequency range.

In this chapter a simple transmission line consisting of two microstrip signal conductors with a common primary and secondary return conductor will be studied to represent a simple connector between ideal PCB ground planes. Apertures in the primary return conductor at the ideal PCB ground plane interface resemble how connector return conductors connect to PCB ground planes in a practical sense. Due to the apertures present between the primary return conductor and ideal PCB ground planes, resonant frequencies in the range of 0-10GHz occur, rather than in the 30-40GHz range when apertures are not present for the ideal attachment of return conductors. The apertures will allow leakage currents from signal transmission to resonate in the cavity formed by the primary return conductor in the 0-10GHz frequency range. The primary return conductor

cavity will represent an imperfect resonator formed by return conductors of adjacent transmission lines in a practical SMTL implementation. Return conductor resonance will result in resonant crosstalk between the microstrip signal conductors. A lossy material slab will finally be used within the primary return conductor cavity to suppress the resonance and therefore reduce the magnitude of resonant crosstalk.

Figure 2 shows the simple microstrip PCB connector with ideal return conductor attachment to an ideal PCB ground plane. The connector consists of a secondary return conductor plate, two microstrip signal conductors, and a hollow box with open sides is the primary return conductor.
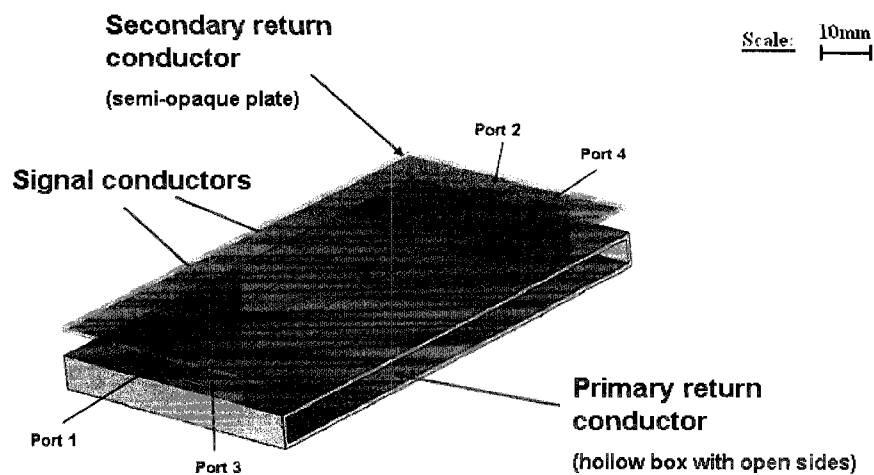
Figure 2: 3D drawing of the simplified ideal connector having air dielectric, which is a 4-port network.

Figure 3 shows the simulated electromagnetic boundary conditions on the six Cartesian planes of the simple ideal connector. For the simulation, the four open conditions are implemented with a vacuum buffer separating the conductor solids from

the open (perfect absorber) simulation boundary planes normal to the y- and z-axes by

7mm. At the two-port launch planes of the connector there is a PEC-like port excitation

boundary. These boundaries act like two ideal PCB surface ground planes.
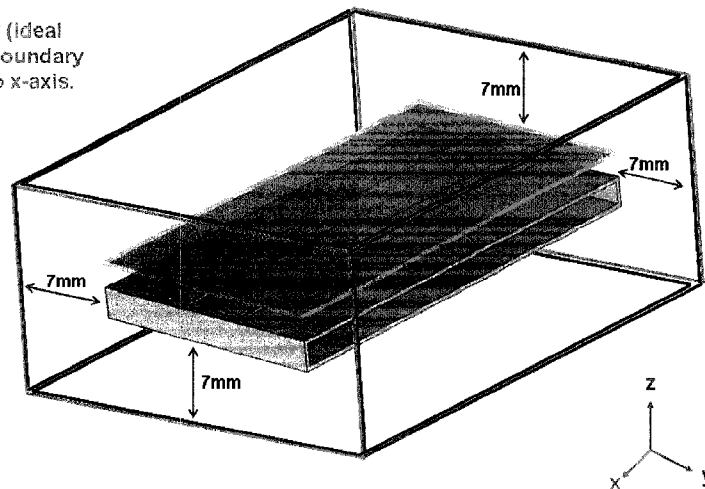
Figure 3: 3D drawing showing the connector simulation boundaries.

Figure 4 shows the dimensional characteristics of the PCB connector simulation

with ideal return conductor attachments. The length of the structure in the direction of

propagation is 100mm. The air gap between the primary and secondary return

conductors is 5mm. Likewise the height of the air gap in the primary return conductor

box is 5mm. The signal conductors are spaced apart sufficiently so that the MTL

crosstalk coefficient between them is negligible. The return conductors are 1mm in

thickness, while the signal conductors are 0.50mm in thickness. The bottom faces of the

signal conductors are spaced 1.50mm above the primary return conductor top face.

15
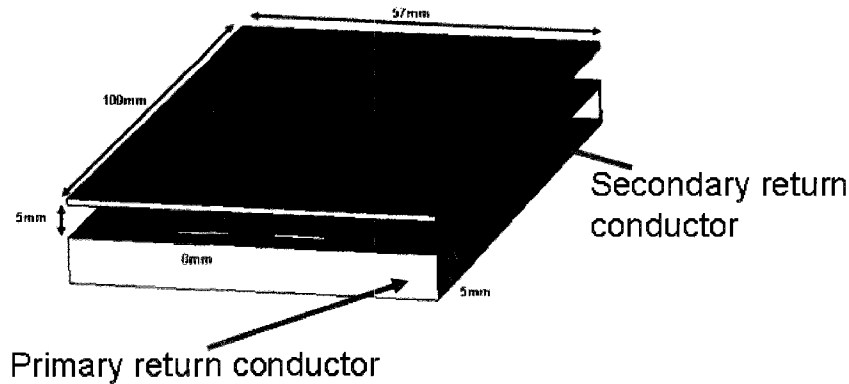
Figure 4: 3D drawing of the simulated connector geometry dimensions.

The air gap of 5mm between the primary and secondary return conductor surfaces should support a $\lambda/2$ resonance at 30GHz when apertures in the primary return conductor are not present. This half-wave frequency is likely to be higher than 30GHz since the presence of two microstrip signal conductors interferes with the 5mm air gap and reduces the effective electrical length between conductor geometries in the cross-section. Because no closed-form solution is readily available to predict this resonance frequency, an electromagnetic simulation was performed on this ideal connector.

A full-wave transient electromagnetic simulation package called CST Microwave Studio was used to obtain a numerical solution for the connector S-parameters[27]. Fields are calculated using FIM techniques. The solid geometries were drawn with the simulation environment. The multi-port transient response was obtained at each circuit port using a 40GHz bandwidth Gaussian impulse input shape. The structure S-parameters were then calculated by the simulator by performing the fast Fourier transform (FFT) on the transient port impulse responses. In order for the FFT to be accurate, the port transient responses were allowed to decay approximately to zero in the

16

simulation. CST Microwave Studio ensures accuracy by employing additional zero-padding to the transient port responses.

The S-parameters of the structure in Figure 5, which use the port numbering convention from Figure 2, show that the return conductor geometries of the connector resonate at 35GHz and result in resonant crosstalk between the two signal conductors. For these S-parameters, port 1 is excited and the magnitude responses at ports 1 through 4 are shown. Crosstalk below 35GHz in this ideal connector is negligible in magnitude.
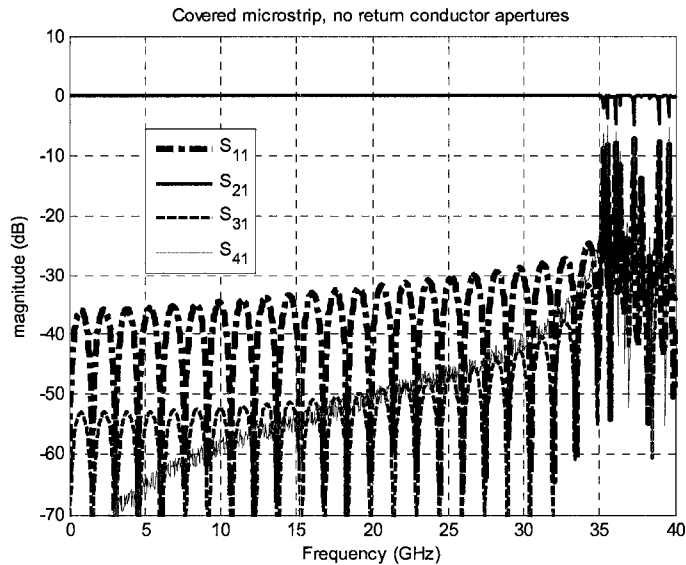
Figure 5: Scattering parameters of the simulated connector with ideal return conductor attachments to the PCB ground plane.

Figure 6 shows the dimensional characteristics of aperture cuts in the primary return conductor used to represent the practical attachment of the connector return conductors to ideal PCB ground planes. Figure 7 is a 3D drawing of the connector simulation with practical return conductor attachment to ideal PCB ground planes.
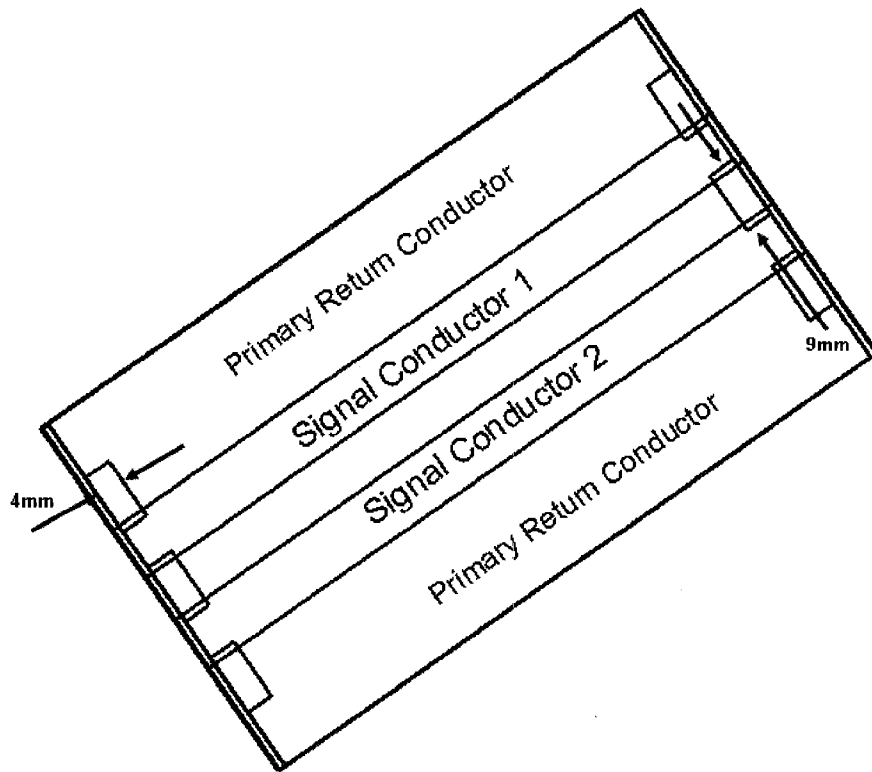
Figure 6: Diagram of aperture cuts in the primary return conductor. This is a top-down view with the secondary return conductor hidden from view for the sake of clarity.
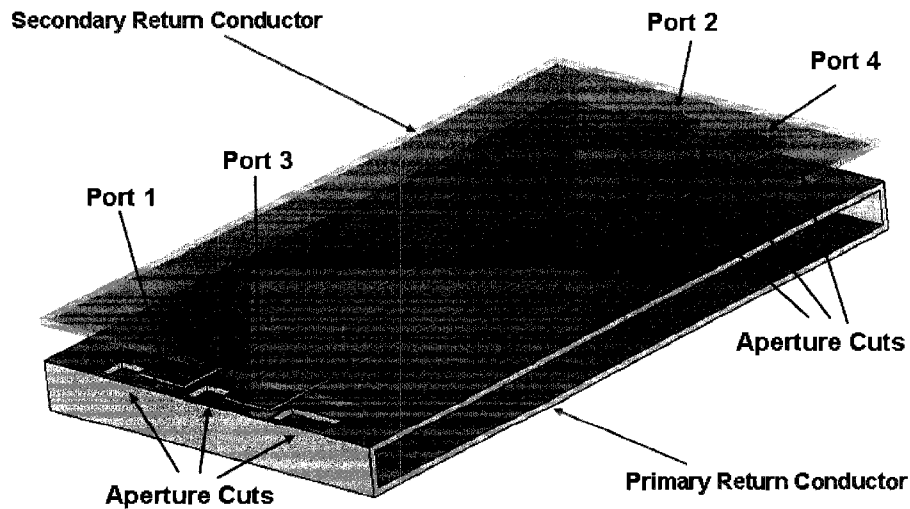
Figure 7: 3D drawing of the connector simulation with practical attachment of return conductors to an ideal PCB ground plane.

Full-wave simulation of this transmission line with practical return conductor

geometry reveals the presence of one well-defined harmonic resonant phenomenon,

manifesting at 1.475GHz, 2.95GHz, 4.425GHz, 5.9GHz, 7.4GHz, and 8.875GHz in the

scattering parameters of the structure. As expected, this harmonic resonance is attributed

primarily to the length dimension of the return conductors, specifically the primary return

conductor cavity. Resonant crosstalk at all of the listed harmonic frequencies exceeds an

arbitrary -35dB figure of merit for crosstalk in the frequency range of interest, 0 - 10GHz.

This structure with aperture cuts, outside of resonance, also exhibits good transmission

characteristics and small crosstalk magnitude. Figure 8 shows harmonic resonant

crosstalk between the two signal conductors, $|S_{31}|$ and $|S_{41}|$, in the frequency range of 0 -

10GHz, using the port numbering convention as shown in Figure 7 when port 1 is

excited.
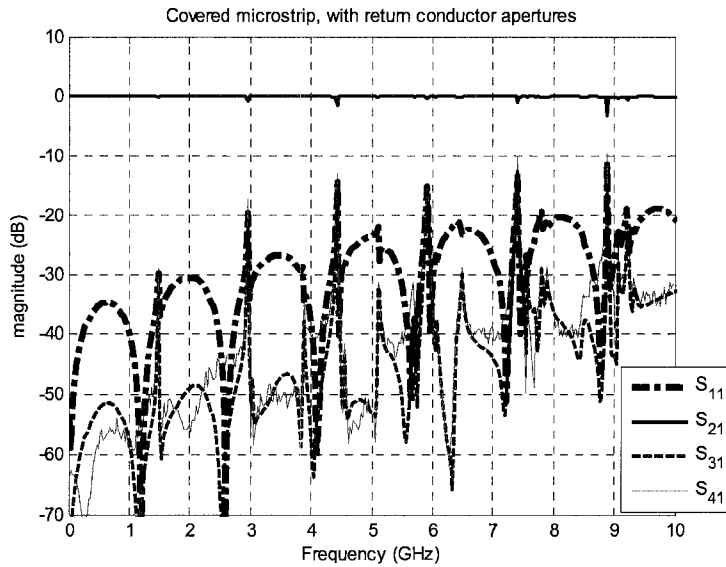
Figure 8: S-parameters of the simple connector with practical return conductor.

To further reinforce the physical understanding that signal transmission leakage

currents resonate in the primary return conductor cavity, the tool of vector surface current

visualisation in the full-wave simulator was utilized at resonance as well as at a frequency

slightly outside of resonance in Figure 9. At the 2.95GHz resonance, current

visualisation shows strong surface current intensity in the lower return conductor air

cavity and strong coupling between the driven signal conductor (ports 1 and 2) and the

second quiet line (ports 3 and 4). There is also resonance in the cavity between the

primary and secondary return conductors. Slightly removed from resonance at 3GHz,

vector surface current visualisation shows greatly reduced surface currents in the return

conductor cavity and on the second signal conductor.
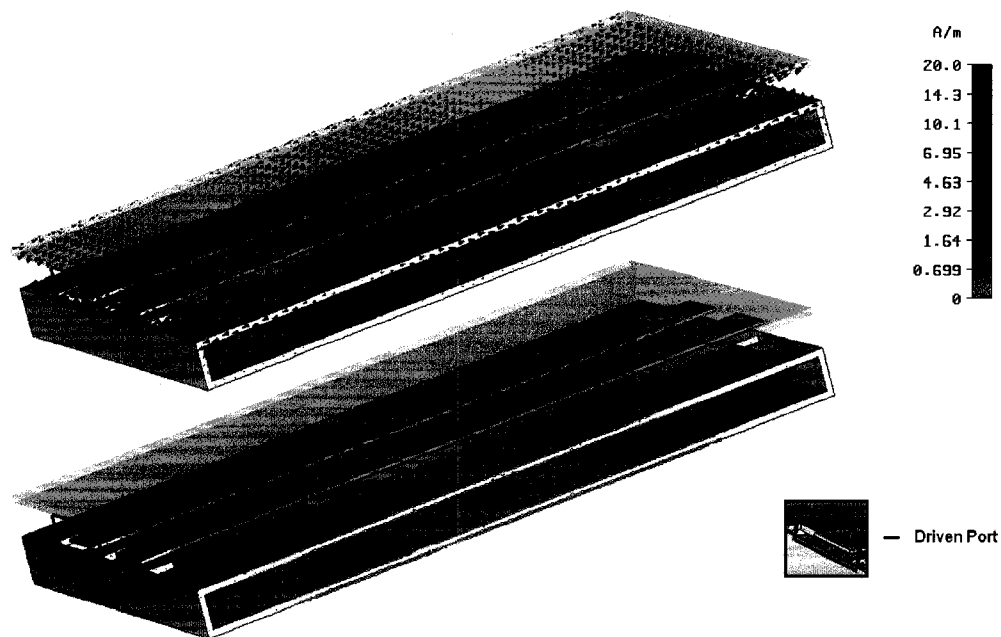
Figure 9: Surface current visualisation of the covered microstrip structure at (top) resonance (2.92GHz cavity standing wave) and (bottom) slightly outside of resonance (3GHz traveling wave).

Since electromagnetic resonance can occur due to imperfections in the return

conductor geometries that couple transmitted signal leakage into nearby parasitic cavities,

it was shown that a portion of signal energy of a quasi-TEM mode connector

transmission line can resonate in undesirable ways in the return conductors of said

connector transmission line. This undesirable resonant energy can couple to other

transmission lines that might share the return conductors and results in unwanted

crosstalk interference. A related example of return conductor resonance in a coaxial

SMA connector is included in Appendix A.

Unwanted crosstalk interference can be reduced by placing a lossy material slab

in the structure cavity. To show the effect of lossy material on damping this type of

resonant crosstalk, and to demonstrate the motivation behind this thesis, a slab of lossy

dielectric material modeled with conductivity of 45 S/m and using a constant

conductivity material dispersion loss model, was placed on one face of the primary return

conductor air cavity to suppress the resonant surface currents of this parasitic cavity

structure as shown in Figure 10.
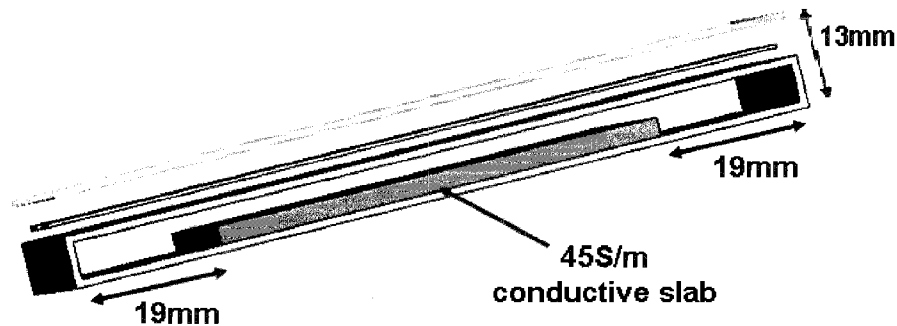
Figure 10: Longitudinal view of a lossy material placement in the microstrip transmission line with aperture cuts in the primary return conductor.

The lossy slab extends for the full transverse width of the PEC cavity, half of the

5mm height of the cavity, and is separated from the two end walls of the cavity by 19mm

of free space. The structure was again simulated, with the addition of the lossy slab in

the cavity. The S-parameters of the lossy slab full-wave simulation are shown in Figure

11.

Covered microstrip, with return conductor apertures & lossy slab
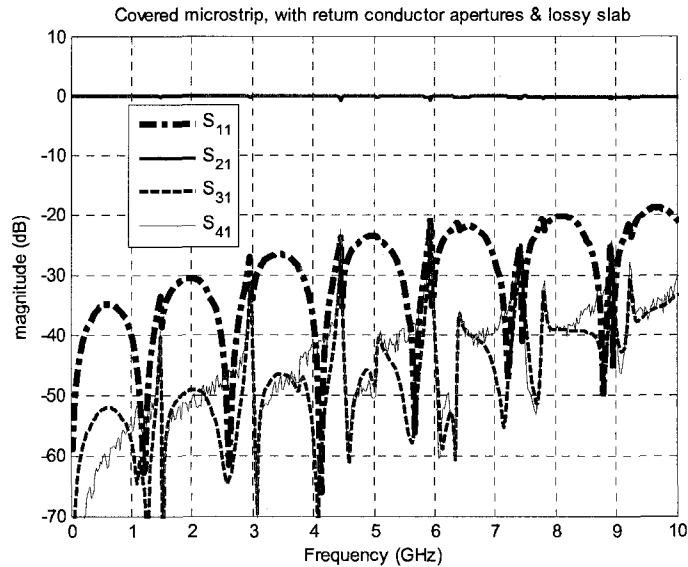
Figure 11: S-parameters of the covered microstrip transmission line with practical primary return conductor attachment and lossy material slab in the adjacent parasitic air cavity.

Analysis of the data in Figures 6 and 11 shows a reduction of resonant far-end and near-end crosstalk from as little as -6.8dB in magnitude at the 5.9GHz resonant frequency, to reduction as much as -14.93dB for the 8.875GHz resonant frequency when the lossy material slab is added to the primary return conductor air cavity. These data show that in theory lossy materials suppress resonance in return conductors with practical attachment to a solid PCB ground plane.

In summary, Chapter 2 showed crosstalk due to resonance in a simple 2-transmission line connector and how the crosstalk is reduced with lossy material. The thesis will study a similar structure with more signal conductors and several return conductor cavities in subsequent chapters. Additional signal conductors in an SMTL connector will provide a larger crosstalk impairment to channel throughput than the simple connector of this chapter.

CHAPTER III

EXPERIMENTAL FIXTURE

This chapter describes the experimental setup used to study the efficacy of lossy

materials in reducing crosstalk due to resonances in a connector return conductor

structure. Section 3.1 describes the connector platform. Section 3.2 has a brief

description of the properties of the lossy materials used in the connector experiments.

3.1 The SMTL Connector Experimental Platform

The experimental platform created for this thesis consists of a simple connector

system of several stacks of microstrip transmission lines between return conductor plates.

The SMTL experimental connector return conductor components were constructed of

robust 0.125" controlled-thickness brass sheet stock. The experimental SMTL connector

was designed to have similar resonant characteristics to contemporary high-speed

commercial connectors. In order to achieve this similarity, the connector plate return

conductors were designed to have air gaps where the connector return conductors make

contact with the PCB surface ground plane. Each return conductor plate has 0.05" by

0.53" gaps in the brass material where the return conductor makes contact with a launch

plate for the SMA signal feeds of the fixture. These gaps are situated directly below the

signal conductor. The gaps in the return conductors were used to excite resonance with

signal transmission leakage currents, and as a result create significant crosstalk between

all of the signal lines in the fixture. The SMTL connector was designed so that lossy

material slabs can be affixed to one face of each connector return conductor for the material experiments.

To emulate the surface ground planes of two PCBs for the experimental SMTL connector under study, large brass launch feed plates were used on either side of the SMTL connector. These two feed plates allow for the removal and attachment of the SMTL connector return conductors, and utilized threaded female 50Ω SMA connectors as via feeds to drive the signal conductors in the experimental connector. The signal conductors of the SMTL connector are constructed of 0.125" diameter copper tube, tapered to interface with the respective signal conductors of the SMA via feeds attached to the two PCB surface feed plates. Comprehensive details about the SMTL connector structure dimensions and construction are provided in Appendix D.

Since the connector uses air dielectric, the distance of 0.625" between the connector return conductor plate faces can support a standing wave in the transverse cross-section at 9.5GHz, which limits the bandwidth of the experimental connector to approximately 10GHz. The spacing between the SMTL connector return conductors will behave as an imperfect parallel plate resonator above 9.5GHz. This standing wave frequency is not of concern in a high density commercial SMTL connector, where the comparatively small electrical length of the gap between adjacent SMTL return conductor shields results in a standing wave frequency that is far above the operational frequencies of any contemporary SMTL connector channel.
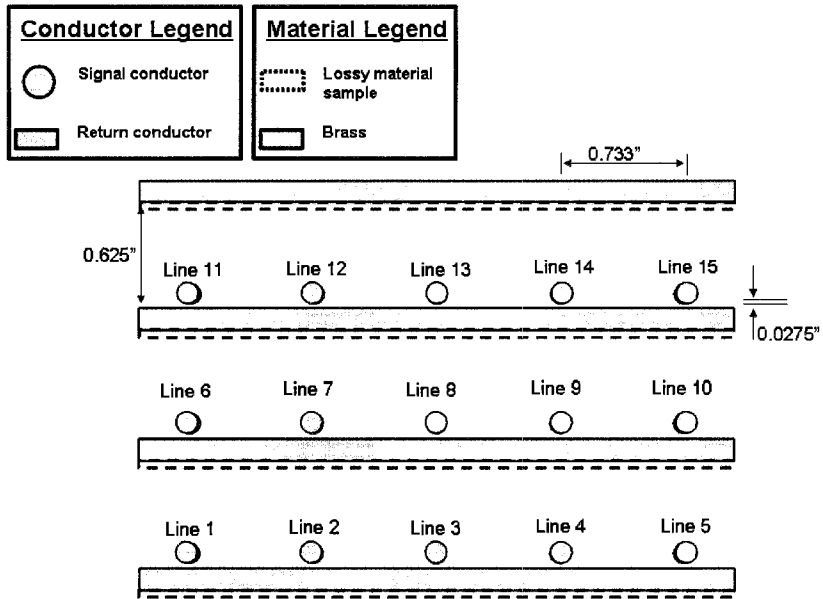
Figure 12: Cross-sectional diagram of the experimental connector.
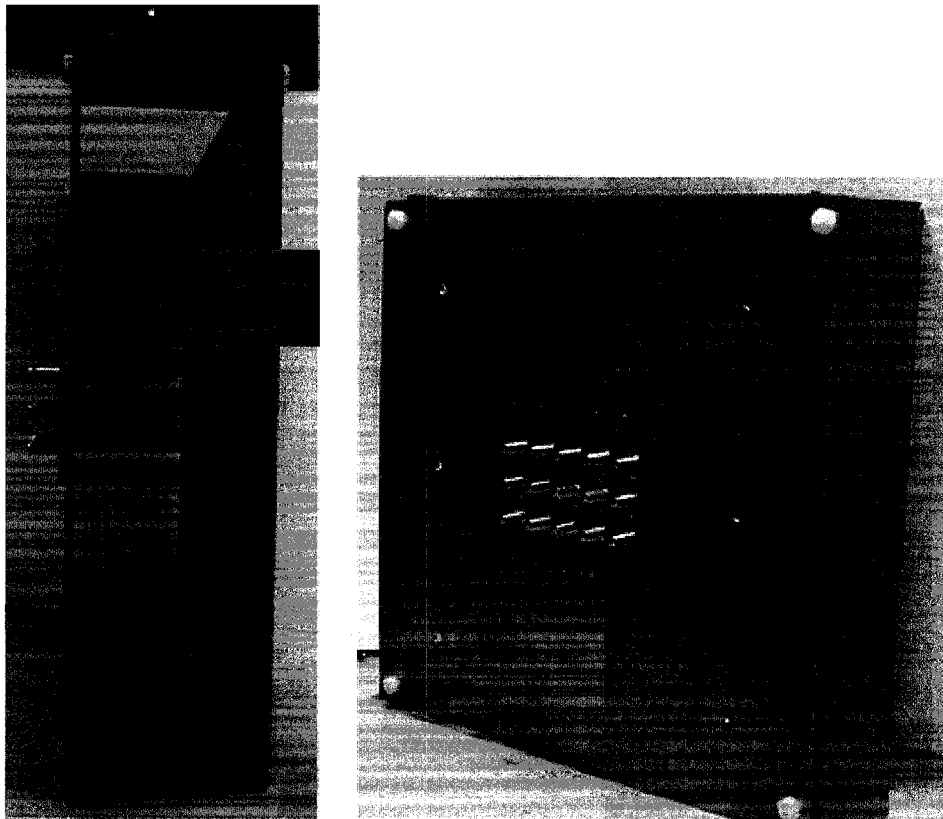
Figure 13: A photograph of the experimental connector setup (12" ruler scale) with side view (left) and front view (right.)

Signal conductors in the experimental connector are always more closely biased toward a primary return conductor (conductor A from Figure 14) than the adjacent secondary return conductor (conductor B from Figure 14). The nominal physical gap between the signal conductors and the primary return conductor plate is 0.0275" to achieve the desired connector cross-section impedance.
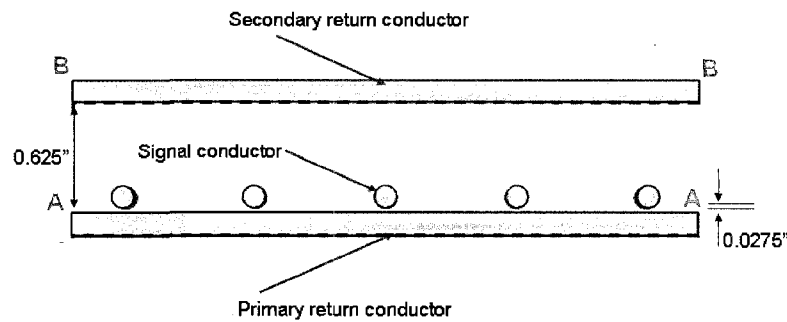
Figure 14: Cross-sectional diagram of a "wafer" in the experimental connector.

Crosstalk interference due to the connector resonant frequencies results in an increase in the connector channel BER. Since the effective propagation delay of a SMTL largely determines certain resonant frequencies, the experimental platform using air dielectric required greater physical length than a commercial connector that uses a plastic dielectric. For example, the signal conductors of a mated Amphenol NeXLev single-ended connector wafer can be up to 1.2 inches in physical length, as shown in Figure 15. Individual wafers are not typically used without the presence of adjacent wafers.
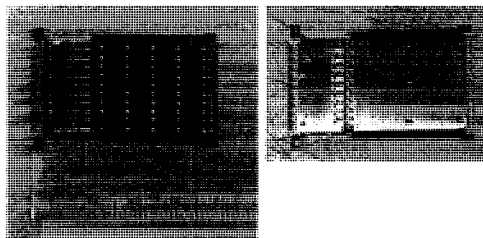
Figure 15: Top view (left) of 8 signal conductors in dielectric and bottom view (right) of shield return conductor from a single NeXLev wafer.

The dielectric of this connector has an approximate relative real permittivity

ε_r'=3.0. The wafer has a propagation delay of approximately 176ps, and the cavity

quarter-wavelength fundamental resonance frequency is approximately 3GHz when

adjacent to other wafers. Evidence of resonance around 3GHz for this connector is shown

in transmission (blue), near-end distant-line crosstalk (green), and far-end distant-line

crosstalk (red) in Figure 16.
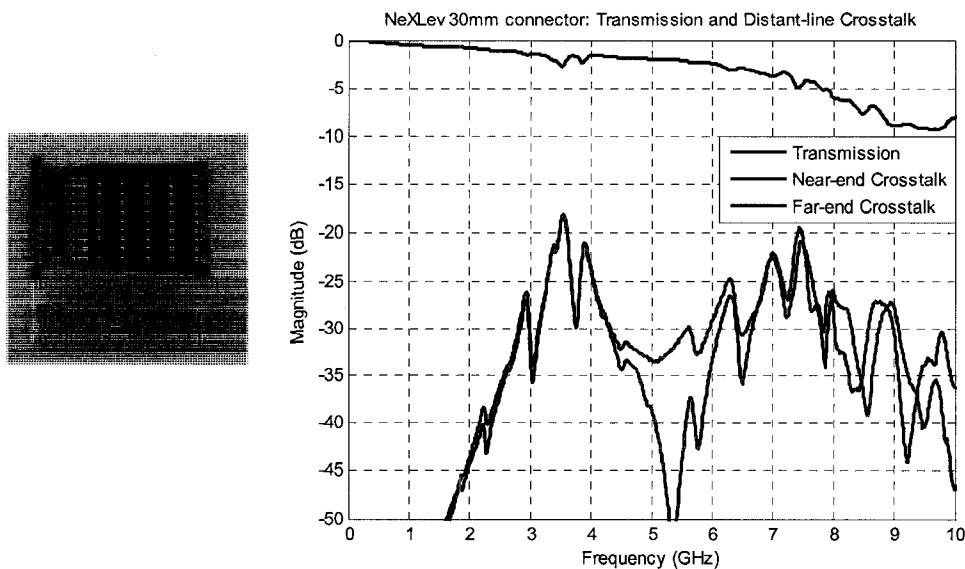
Figure 16: Diagram (left) and graph (right) shows evidence of resonance in transmission (blue), near-end (green) crosstalk, and far-end (red) crosstalk.

A transmission line with air dielectric in the SMTL connector structure for this

study was designed to have a physical length of approximately 3.0 inches, propagation

delay of 250ps, and cavity quarter-wavelength fundamental resonance frequency of

approximately 2GHz, similar to resonance frequencies in existing commercial

connectors.

A commercial connector system was not used as the experimental platform for

this study due to complex features such as a connector separable interface, punch holes in

the shield return conductors, and the difficulty of modifying connector plastic features with miniature machining technology. Additionally, consistency in controlling the thickness dimension of lossy materials in a miniature commercial connector system is difficult to achieve outside of an industrial manufacturing setting. The lossy material samples used in the experiments are generally much thicker than might be used in typical production manufactured connector wafers as well.

One feature of the experimental connector is that the size of the transmission line components was designed such that it is easy to remove and install lossy material samples without disturbing the other connector elements. Another useful feature of using thick, robust transmission line conductor components is that it allows for the use of simple air dielectric rather than plastics. Air dielectric is advantageous to this study since this eliminates dielectric loss in the SMTL connector. Hence the loss in the connector is due to transmission line component conductor loss, lossy material sample loss, and radiation loss. Yet another feature of this design is that one can easily simulate the simple structures in a full-wave electromagnetic simulator to obtain numerical results.

The secondary return conductor of the SMTL experimental platform has negligible influence on transmission line characteristic impedance due to its physical distance from the signal conductor electromagnetic field configuration in the connector cross-section. Outside of resonance, this adjacent secondary conductor face is not considered to be a significant surface current path. The SMTL experimental connector configured in this way is useful in isolating the influence of lossy material slabs on reducing crosstalk surface currents. Lossy material slabs of uniform thickness are attached to the face of the secondary return conductor, as illustrated by dashed lines in the

connector cross-section view of Figure 12. The approximate characteristic impedance of

a connector transmission line in the cross-section is 53Ω.

A measured time domain reflectometry (TDR) plot of the baseline connector is

shown in Figure 17. The time domain reflectometry instrument used for this

measurement was an Agilent 54754A TDR module with a 35ps rise time step waveform

generator. Measurements were performed in a nonsterile laboratory environment at room

temperature and static wrist straps were used. A TDR plot is the measurement of the

reflection transient step response to the input step pulse, represented in terms of effective

transmission line impedance, where the instrument reference impedance is 50 ohms. This

instrument is useful for identifying impedance discontinuities in transmission line

connections, but its utility in characterising transfer functions is limited by the relatively

high noise floor (>-50dB) of the instrument and only one reflection measurement port.
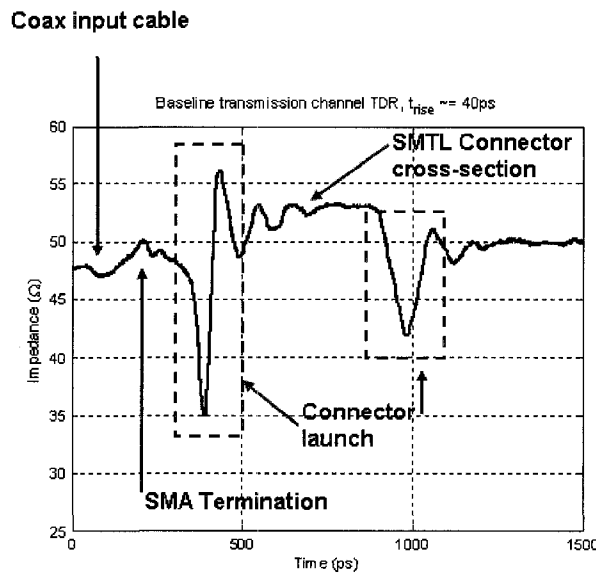
Figure 17: TDR plot of the impedance on line 8.

Ports numbers were assigned to the SMA feeds of the connector. The connector

has a total of thirty ports, fifteen ports at each PCB surface ground plane, with two ports

per transmission line in the fixture. Each transmission line two-port network is assigned a successive odd number for one port, and the other side is assigned the successive even number. Odd-numbered ports were assigned to only one side and even-numbered ports were assigned to the other side of the connector. Numbering begins in one corner of the five-by-three connector transmission line matrix, and port numbers are sequentially increased within a return conductor cavity before numbering proceeds to an adjacent cross-shield cavity. Every successive pair of odd- and even-numbered ports constitutes a successively numbered transmission line. For instance, ports 1 and 2 are attached to line 1, ports 15 and 16 are attached to line 8, and ports 29 and 30 are attached to line 15, as shown in Figures 12 and 18.
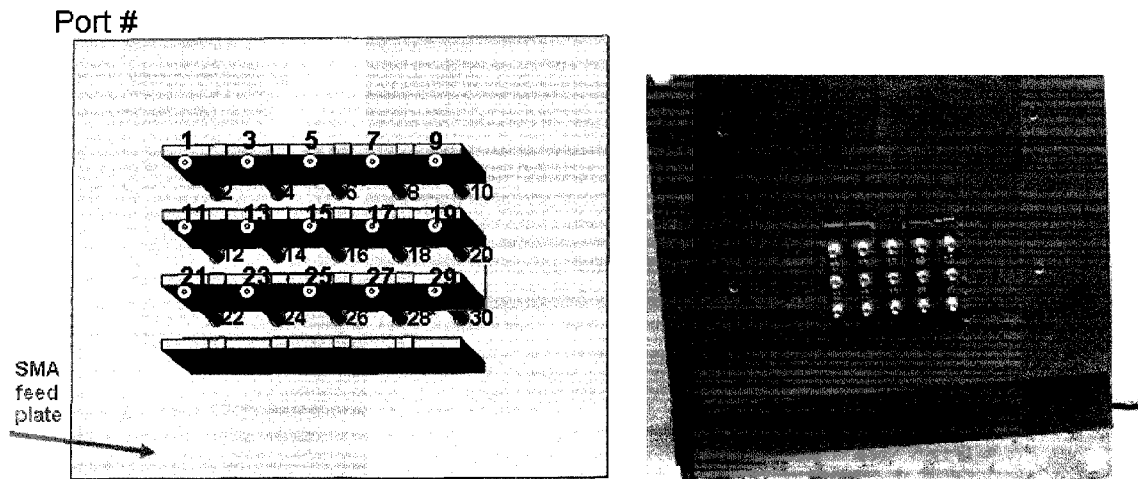
Figure 18: Pinout numbers (in red) of the SMTL connector structure (drawing on left, photograph on right). One SMA feed plate (left) is hidden for ease of visualising port numbering convention.

3.2 Lossy Material Descriptions

For use in the connector structure, 0.030"-thick lossy material slabs were prepared for use in the experiments. Lossy material slabs of uniform thickness were affixed to the face of the transmission line secondary return conductors within the connector. Two broad categories of lossy materials used in the study are conductive lossy materials and nonconductive lossy materials.

3.2.1. Conductive Materials

The quasi-conductor materials used in this study and some of their known properties are listed in Table 1.

Table 1: Properties of Conductive Materials

Material Name	Spec Sheet Bulk Conductivity	Measured Bulk Conductivity	Filler Material	
			Carbon	Nickel
1.5 S/m material	1.57 S/m	1.5 S/m	X	
1500 S/m material	2000 S/m	1500 S/m	X	
Material A	N/A (Custom)	45 S/m	X	
Material B	N/A (Custom)	31 S/m	X	X

Bulk quasi-conductor lossy materials used in the connector are all a thermoplastic base resin system impregnated with an unknown volume concentration of conductive particles. Material A, the 1.5 S/m material, and the 1500 S/m material are impregnated with fine conductive carbon particles. Material B is filled with a mixture of fine carbon and nickel particles. Graphite and nickel powder are inexpensive and available on demand from the market.

3.2.2. Nonconductive Materials

The nonconductive materials used in this study and some of their known

properties are listed in Table 2.

Table 2: Properties of Nonconductive Materials

Material Name	Volume Conductivity	Relative Impedance $\mid \eta_m / \eta_0 \mid$	$\tilde{\varepsilon}$ & $\tilde{\mu}$ values available?
CRS-124	<1E-8 S/m	0.4	Yes, in Appendix B
MCS	<5E-7 S/m	0.3	Yes, in Appendix B

The MCS and CRS-124 materials are both commercial microwave absorber

materials that are highly frequency dependent with high magnetic and dielectric loss

tangents. The materials are elastomer matrices filled with high performance ferrite

powder. High performance ferrite powders are typically propriety niche products and

therefore tend to be costly. The CRS-124 and MCS materials have a similar propagation

attenuation rate, but dissimilar a relative impedance to free space, CRS-124 being more

closely matched to free space. Datasheet values for nonconductive material complex

permeability, complex permittivity, intrinsic impedance relative to free space, and

attenuation rate for these two materials are provided in Appendix B. A laboratory

measurement of insertion loss was performed on these materials in a coaxial test fixture

sample holder to verify the provided manufacturer datasheet values. Measurement

procedure and data are provided in Appendix E. Datasheet values for the ferrite materials

were found to be consistent with measurement.

In summary, Chapter 3 provided an overview of the experimental platform used

for both numerical simulation and measurement. This chapter also discussed relevant

electromagnetic parameters of the lossy material samples used in the experiments.

CHAPTER IV

EXPERIMENTAL DATA & ANALYSIS

In this chapter measurement and the computer simulation data are examined in the time domain and frequency domain. In section 4.1 a full-wave simulation of the central signal conductor in the connector with and withouth lossy material is presented along with theoretical models for the material losses. Section 4.2 describes the crosstalk S-parameters on the central signal conductor due to the neighbouring signal conductors in the connector. In section 4.3 S-parameter magnitude data of the simulated and measured connectors are compared. Simulation and measurement of connector S-parameters are examined and discussed. Section 4.4 presents the channel eye patterns of the connector central signal conductor with crosstalk interference. The simulated and measured connector eye patterns for the baseline and lossy material connectors are also discussed. Section 4.5 presents the BER and channel quality factor (Q) of the measured baseline and lossy material connector channels. Section 4.6 discusses principles of the insertion loss-crosstalk ratio (ICR) in the frequency domain, as well as a slope fitting measure of the ICR. Section 4.7 provides a relationship between ICR fit slope and connector channel BER, a relationship between ICR fit slope and connector channel Q, and a relationship between the ICR fit slope and the connector output eye pattern vertical opening.

4.1 Full-wave Simulation of the Connector

CST Microwave Studio, a commercial FIM full-wave field solver environment were used to simulate the experimental connector. Insertion loss and crosstalk magnitude was obtained theoretically using the full-wave (3D) simulation of the multi-port experimental SMTL connector with bare conductor plates (baseline configuration) and connector lossy material configurations, where only a port connected to the central signal conductor (line 8) is excited. Quasi-conductor lossy materials were simulated in the connector using a constant conductivity model with $\varepsilon_r'=4$, a typical value for the lossy material base polymer system. For simulation of Material B, which is a mildly ferromagnetic quasi-conductor material, the mean value for this material can be assumed to be $\mu_r'=1.5$, as the magnetic metal component of this material is very small compared to the rest of the material contents. The two nonconductive ferrite-dielectric absorber materials were simulated in the connector using measured values given by the manufacturer for the complex permeability and permittivity. The S-parameters for connector insertion loss and crosstalk magnitude were obtained on the connector with and without the lossy materials affixed to the connector plate return conductors.

4.2 Measurement of the Connector

In the measurement of the connector, only 4-port measurements were available to probe two transmission lines in the SMTL connector fixture for insertion loss and crosstalk S-parameter transfer functions, while the remaining 26 ports were terminated with precision 50Ω broadband SMA loads. The 4-port S-parameter measurements were acquired with an Agilent E8364B VNA using broadband SOLT calibration to remove the

effects of the measurement cables. S-parameter measurements were recorded in the frequency range of 20MHz to 25GHz. The sample interval for the frequency range was measured in 10MHz increments. Measurements were performed in a nonsterile laboratory environment at room temperature. Static wrist straps were used. To reduce the total number of necessary measurements on the connector experiments, crosstalk port symmetry was assumed about a symmetry plane in the connector. Appendix C shows that reducing the number of crosstalk measurements using the assumption of symmetry with respect to line 8 is equivalent to measurement of all the symmetrical crosstalk terms onto line 8. S-parameter measurements were performed for the baseline connector and the cases where the connector return conductors are coated with lossy material.

4.3   Connector Crosstalk Frequency Domain Magnitude S-Parameters

4.3.1   Baseline Connector Individual Crosstalk Contributors

When one of the connector ports is excited at one of the system's resonant frequencies, all the other connector ports are also illuminated. For the baseline connector this results in the near-end and the far-end crosstalk at the central signal conductor port having the same magnitude. Crosstalk interference contributors from neighbouring lines onto a receiving transmission line channel of the connector are dependent on the direction of signal propagation of the neighbouring lines. For a connector, the crosstalk on a receiving channel due to a neighbouring transmitting channel comes from the near end, while crosstalk on a receiving channel due to a neighbouring receiving channel comes from the far end. Since transmitters and receivers can be placed in an arbitrary pattern within an SMTL connector appropriate for an application, line 8 of the experimental

connector is treated as the receiving channel of interest surrounded only by transmitters.

Therefore only near-end sources of crosstalk interference on line 8 originate from other

connector transmission lines for this connector channel. Neighbouring transmission lines

in the baseline connector are not used as far-end crosstalk sources since far-end and near-

end sources of crosstalk are similar in magnitude. Far-end crosstalk terms will not be

relevant to the particular connector channel study, but will be shown to be similar in

magnitude to near-end crosstalk interference sources.

Figure 19 shows the similarity in resonant magnitude for a particular transmission

line (line 1) used as a source of both far-end and near-end crosstalk on line 8 in the

simulated baseline connector.
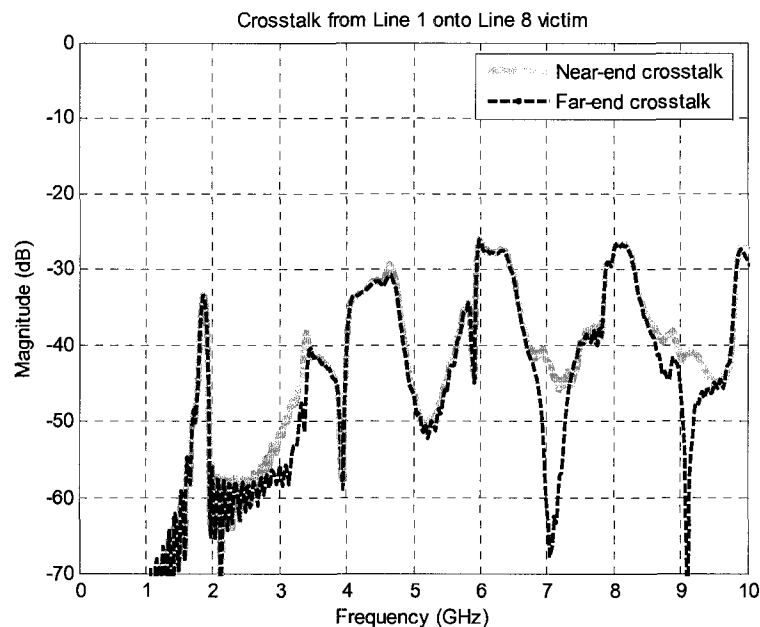
Figure 19: A comparison of the magnitude response of far-end and near-end
crosstalk from line 1 to line 8 of the baseline connector.

Crosstalk in the experimental connector is harmonically resonant, with resonant

peaks approximately every 2GHz. This harmonic resonance is consistent with the

quarter-wavelength resonance frequency associated with the connector length of 3 inches,

or twice the connector's electrical length in air. The gaps formed by the attachment of

the connector return conductors to the launch ground planes permit signal transmission

leakage currents to resonate in the structure.

The simulated and measured magnitude response for several of the largest

magnitude near-end crosstalk interference sources on line 8 of the experimental SMTL

connector are shown in Figures 20 and 21 respectively.
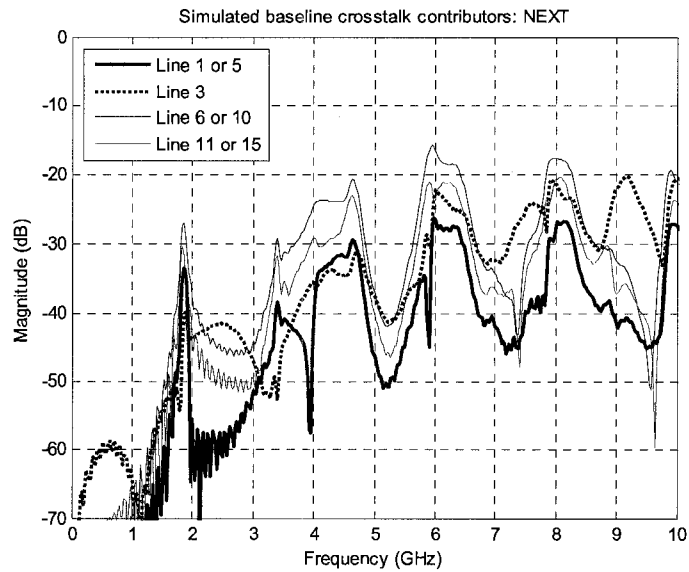
Figure 20: Several near-end crosstalk magnitude spectra in the simulated baseline connector.
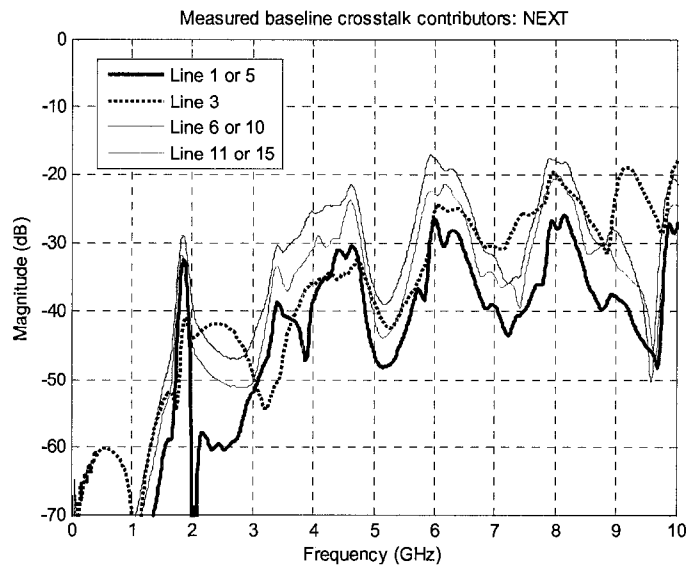
Figure 21: Several near-end crosstalk magnitude spectra in the measured baseline connector.

The simulated and measured magnitude response for several of the largest magnitude far-end crosstalk interference sources on line 8 of the experimental SMTL connector are shown in Figures 22 and 23 respectively.
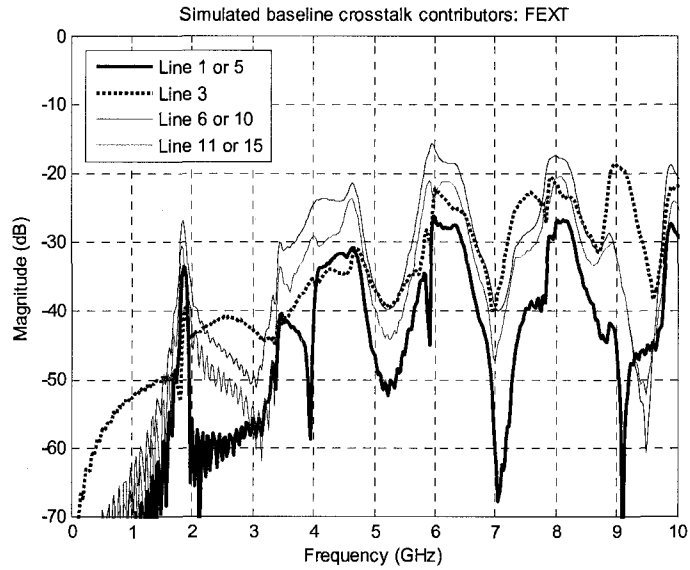
Figure 22: Several far-end crosstalk magnitude spectra in the simulated baseline connector.
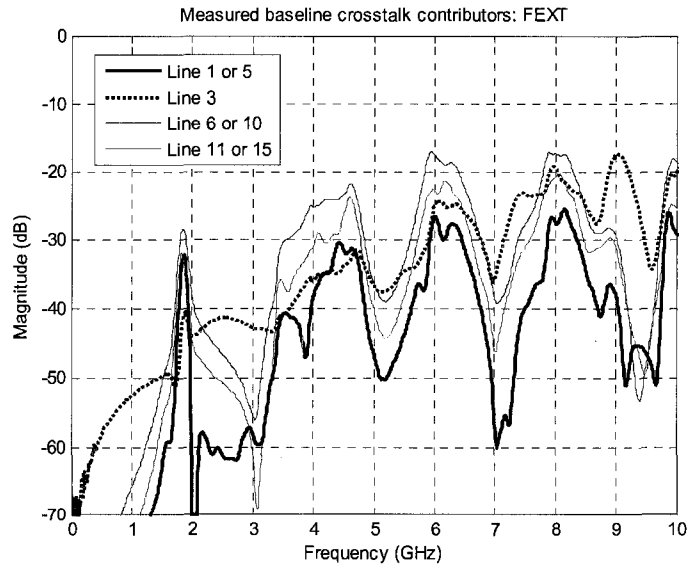
Figure 23: Several far-end crosstalk magnitude spectra in the measured baseline connector.

The simulated connector individual crosstalk source spectra have very similar peak frequencies, null frequencies, and have similar curvature characteristics when compared to measurements of the connector. This similarity indicates that the simulation closely reproduces the physical electromagnetic propagation characteristics and shows that the simulation methodology is valid. Additionally, a comparison of Figure 20 to Figure 22 for simulation or a comparison of Figure 21 to Figure 23 for measurement shows that peak crosstalk amplitude for these sources of near-end and far-end crosstalk interference are practically identical in magnitude for crosstalk greater than -40dB.

Because there are 14 other transmission lines in the connector in addition to line 8, the cumulative effect of crosstalk interference superposition from these 14 transmission line sources will result in amplitude distortion of the output signal at operating frequencies where connector resonant crosstalk is excited by the input waveform. Tables 3 and 4 compare baseline simulated and measured connectors by using superposition of crosstalk magnitude in the connector on line 8 for the resonant frequencies of 2GHz and 4GHz, for near-end and far-end crosstalk respectively.

Table 3: Simulated and Measured Superposition NEXT Magnitude on Line 8.

Resonant Frequency (GHz)	Simulated* Superposition NEXT on Line 8 (dB)	Measured** Superposition NEXT on Line 8 (dB)
2	-24.11	-25
4	-10.79	-11.59

Table 4: Simulated and Measured Superposition FEXT Magnitude on Line 8.

Resonant Frequency (GHz)	Simulated* Superposition FEXT on Line 8 (dB)	Measured** Superposition FEXT on Line 8 (dB)
2	-23.45	-23.96
4	-10.56	-11.06

*S-parameter crosstalk values obtained from full-wave simulation.
**S-parameter crosstalk values obtained from VNA measurement.

Since the resonances in the connector do not result in crosstalk peaks exactly at harmonics of 2GHz, the superposition crosstalk is generally larger in magnitude for frequencies around these harmonics, with superposition crosstalk magnitude increasing with higher harmonics of the resonance.

4.3.2 Connector Insertion Loss and PSNEXT

The total frequency domain magnitude crosstalk interference on the line 8 receiver, surrounded by only near-end crosstalk sources in the connector, is referred to as the power sum near-end crosstalk (PSNEXT). The PSNEXT on line 8 is computed with Equation 4-1.

$$PSNEXT \ (f) = \sqrt{\sum_{n=1}^{7} \left[abs \ \left(S(f)_{16,2n}\right)^2\right] + \sum_{n=9}^{15} \left[abs \ \left(S(f)_{16,2n}\right)^2\right]} \tag{4-1}$$

Since data are conveyed through the connector channel as a baseband square wave pulse train rather than a pure sinusoid waveform, total crosstalk is not represented as the superposition of crosstalk magnitudes at each frequency. Instead, PSNEXT is used to determine the magnitude crosstalk spectrum for the connector channel. Shown below is the magnitude insertion loss and PSNEXT for all simulated and measured connectors in the baseline and lossy material configurations. Each connector material configuration of the connector is individually compared between simulation and measurement.
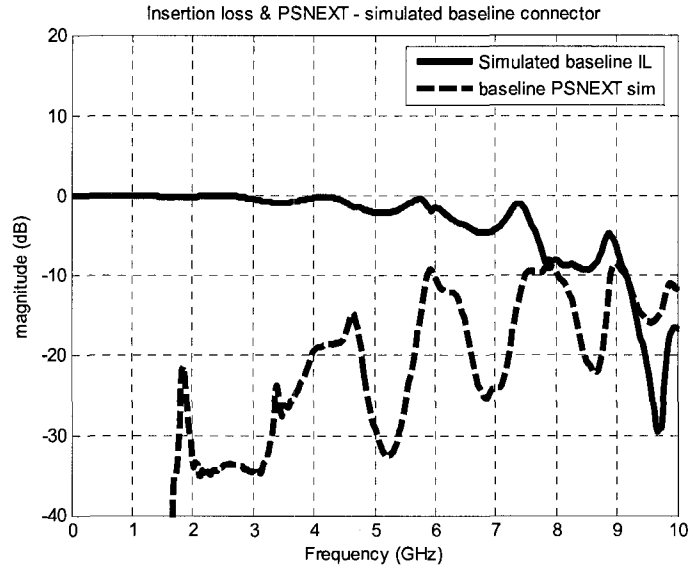
Figure 24: Insertion loss magnitude and PSNEXT plot of the simulated baseline connector.
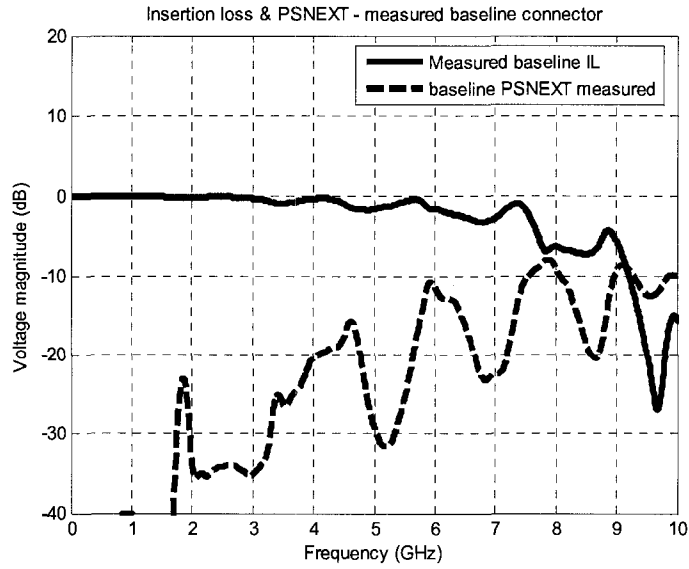
Figure 25: Insertion loss magnitude and PSNEXT plot of the measured baseline connector.

41
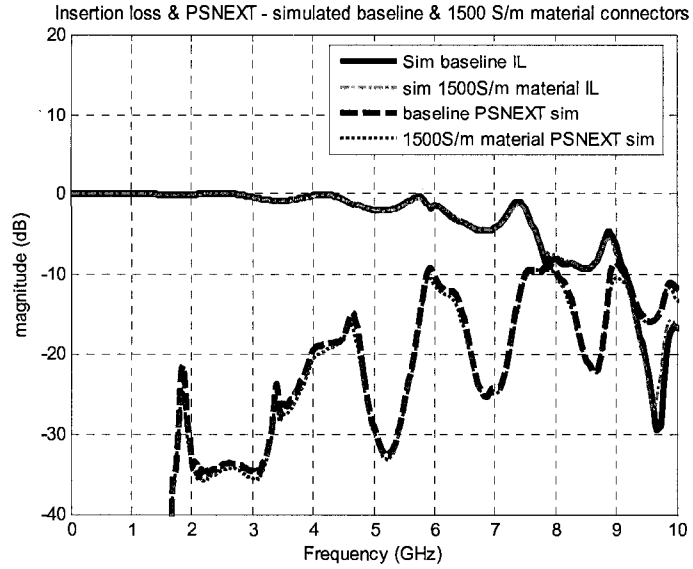
Figure 26: **Insertion loss magnitude and PSNEXT plot of the simulated 1500 S/m lossy sample connector compared with the baseline connector.**
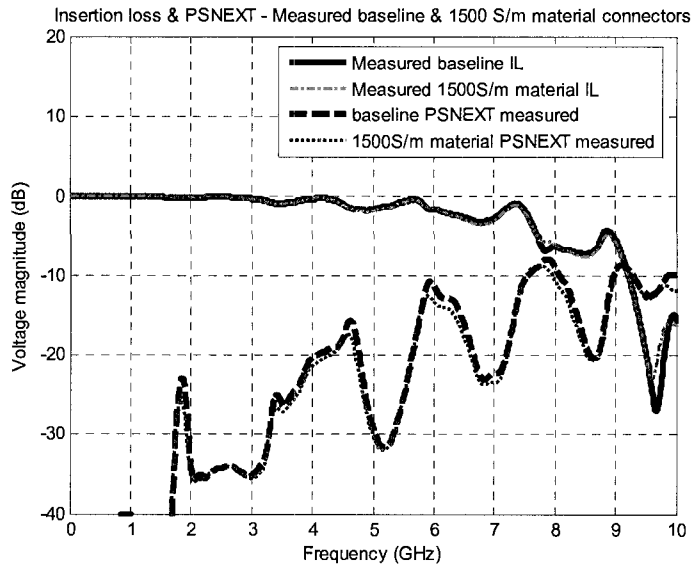
Figure 27: **Insertion loss magnitude and PSNEXT plot of the measured 1500 S/m lossy sample connector compared with the baseline connector.**
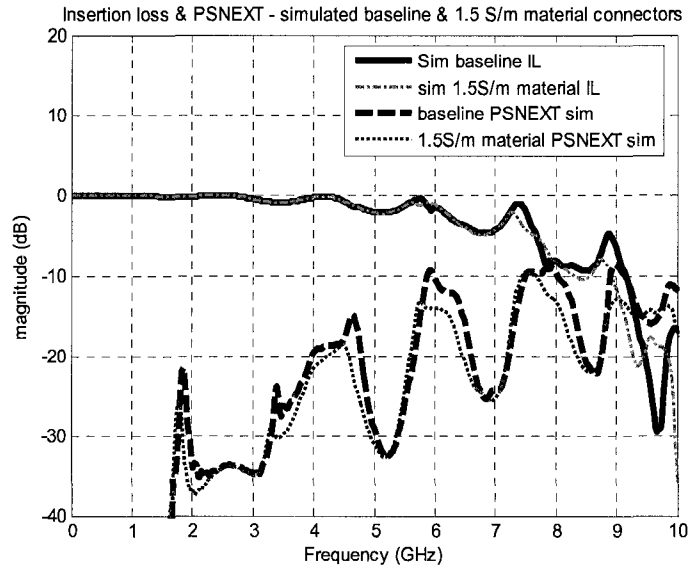
Figure 28: Insertion loss magnitude and PSNEXT plot of the simulated 1.5 S/m lossy sample connector compared with the baseline connector.
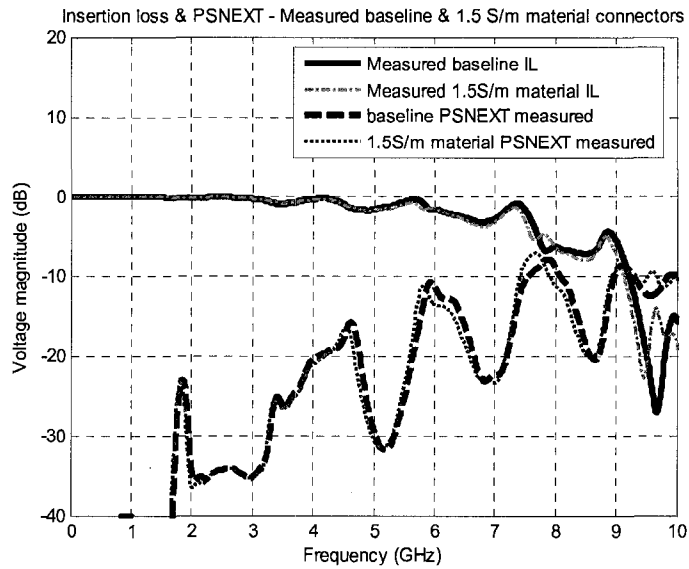
Figure 29: Insertion loss magnitude and PSNEXT plot of the measured 1.5 S/m lossy sample connector compared with the baseline connector.
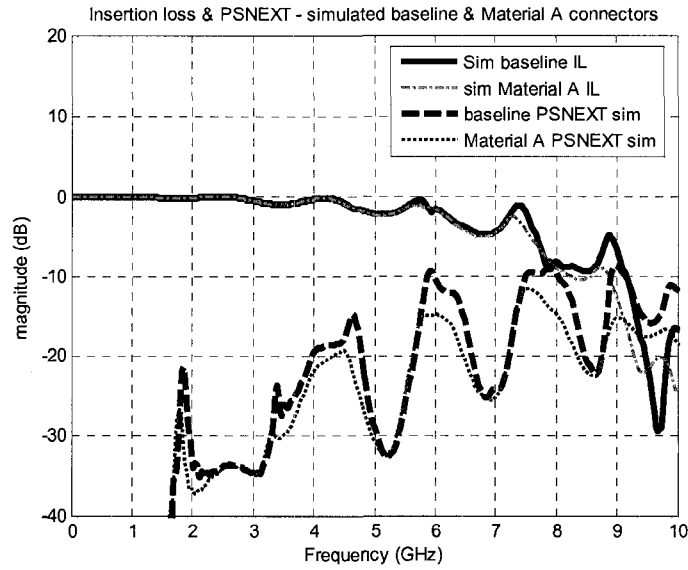
Figure 30: Insertion loss magnitude and PSNEXT plot of the simulated Material A lossy sample connector compared with the baseline connector.
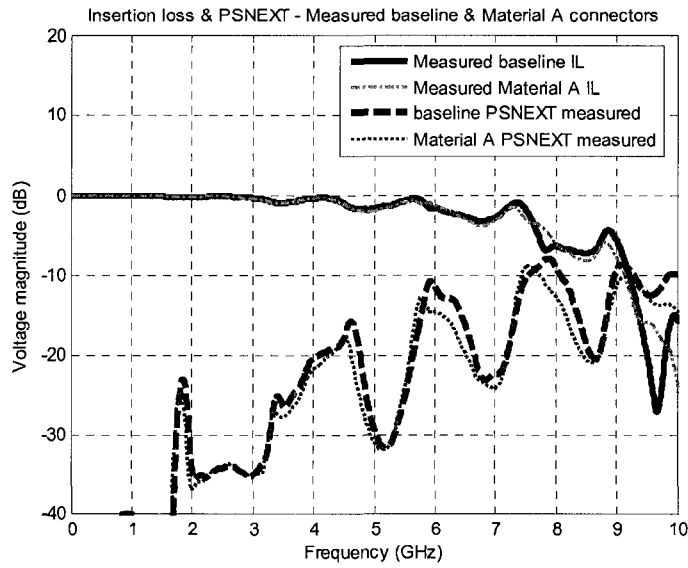
Figure 31: Insertion loss magnitude and PSNEXT plot of the measured Material A lossy sample connector compared with the baseline connector.
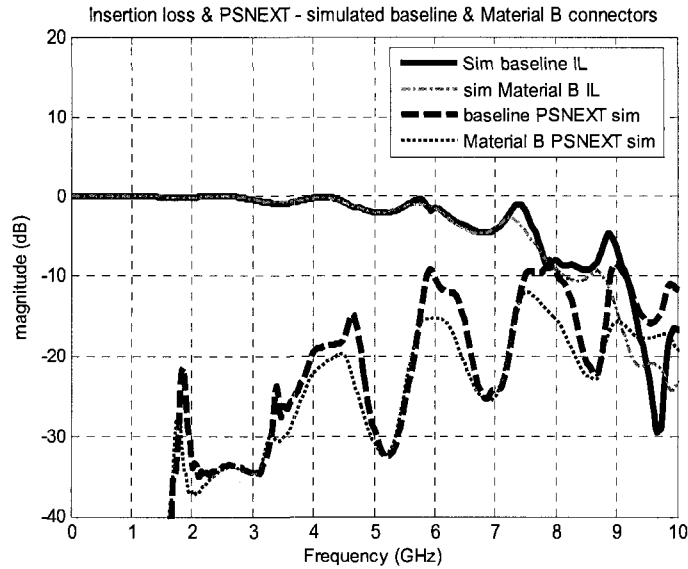
Figure 32: Insertion loss magnitude and PSNEXT plot of the simulated Material B lossy sample connector compared with the baseline connector.
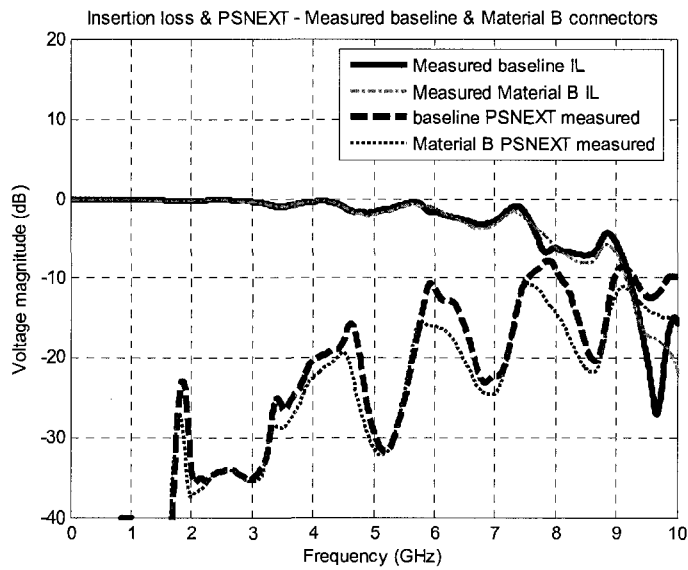
Figure 33: Insertion loss magnitude and PSNEXT plot of the measured Material B lossy sample connector compared with the baseline connector.
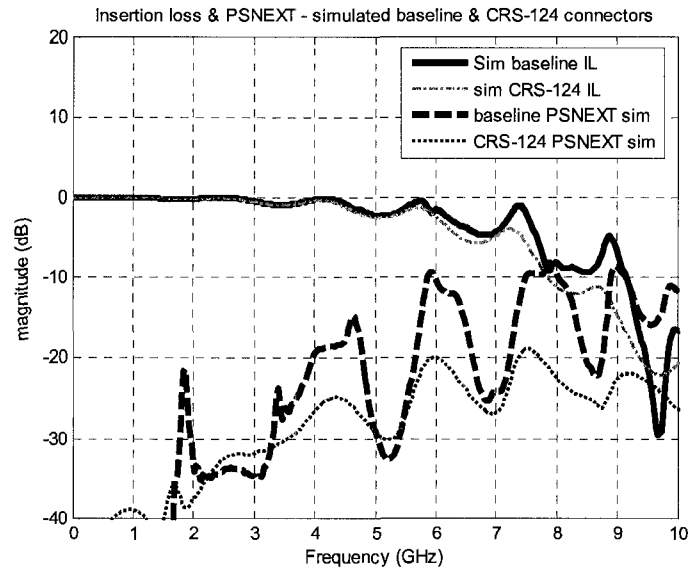
Figure 34: Insertion loss magnitude and PSNEXT plot of the simulated CRS-124 lossy sample connector compared with the baseline connector.
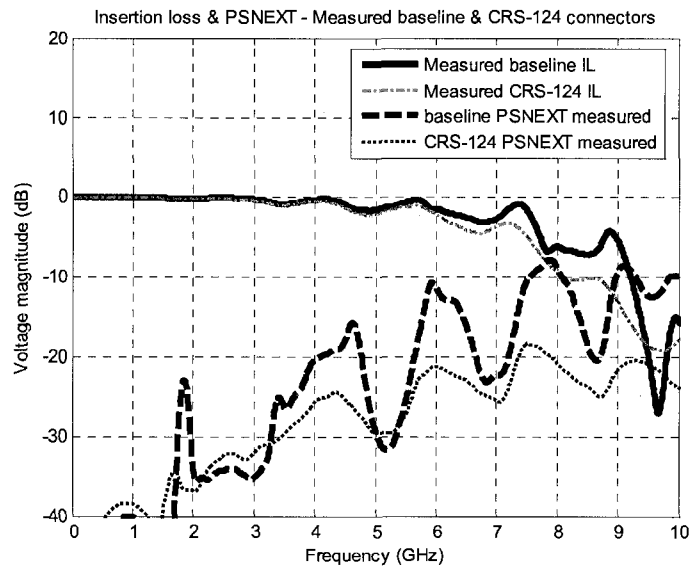
Figure 35: Insertion loss magnitude and PSNEXT plot of the measured CRS-124 lossy sample connector compared with the baseline connector.
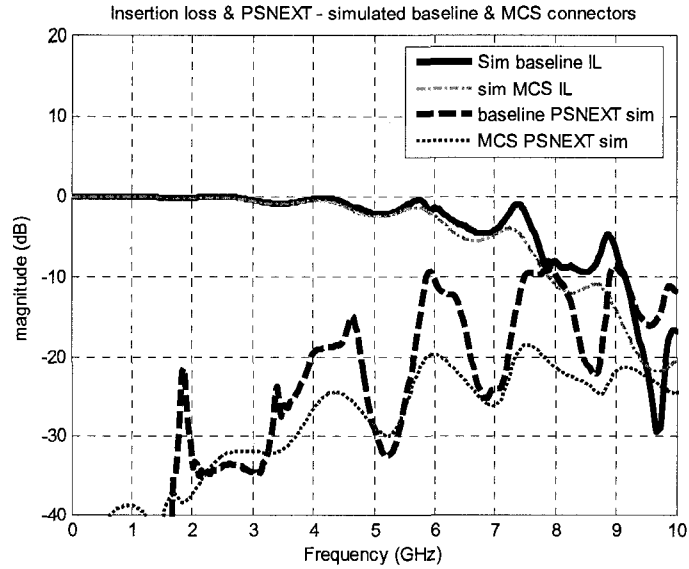
Figure 36: Insertion loss magnitude and PSNEXT plot of the simulated MCS lossy sample connector compared with the baseline connector.
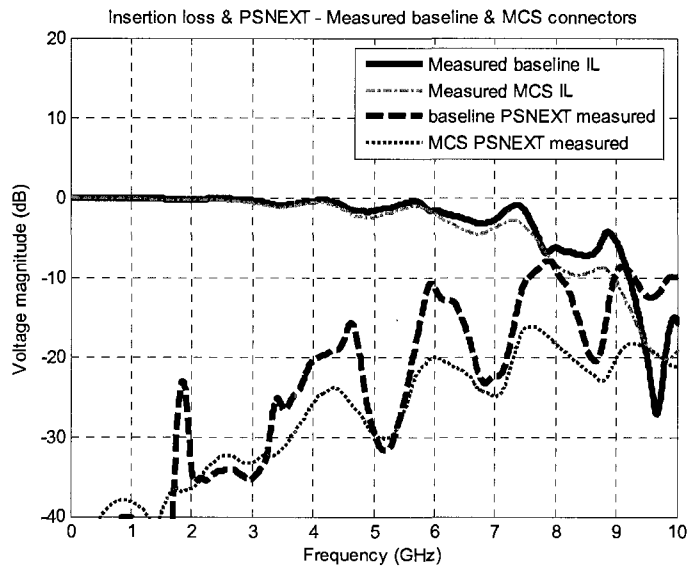
Figure 37: Insertion loss magnitude and PSNEXT plot of the measured MCS lossy sample connector compared with the baseline connector.

Figures 24 and 25 show insertion loss and PSNEXT magnitude spectra for the baseline simulated and measured connectors respectively. Simulation of the baseline connector accurately reproduces peaks, nulls, and general curvature in PSNEXT magnitude and insertion loss in comparison to the measured connector within 2dB. Nulls in insertion loss from the simulated baseline connector are smaller in magnitude than the measured baseline connector, which can be explained by the excess simulation transmission line impedance mismatch in the modeling of the connector launch. The particulars of the connector launch mismatch will be explained in more detail later in section 4.5.2. The excess mismatch naturally results in stronger standing wave cancellation characteristics associated with the connector electrical length. Similarly, peaks at PSNEXT resonance frequencies in the simulated baseline connector are slightly larger in magnitude than is seen in measurement. In general, if a slightly higher impedance mismatch exists in some baseline resonant connector, then more energy is trapped ringing between the connector mismatches, and therefore a larger quantity of that resonant energy will naturally couple onto other transmission lines within the resonant connector.

Figures 26 and 27 show insertion loss and PSNEXT magnitude spectra for the simulated and measured connectors respectively, which compare the baseline connector and the connector with 1500 S/m lossy slabs. Comparison of the simulated and measured connector insertion loss and PSNEXT magnitude spectra of the 1500 S/m lossy material experiment shows agreement within 3dB. The change in resonant behaviour between the baseline and material experiments when comparing simulation and measurement is

similar, although the simulation underestimates the measured reduction in PSNEXT magnitude or enhanced crosstalk skin effect loss for this connector experiment.

Figures 28 and 29 show insertion loss and PSNEXT magnitude spectra for the simulated and measured connectors respectively, comparing the baseline connector and connector with 1.5 S/m lossy slabs. When comparing the simulated and measured connector insertion loss and PSNEXT magnitude spectra of the 1.5 S/m lossy material experiments, the results are noticeably different. The connector insertion loss is practically identical for both the simulated and measured connector with 1.5 S/m lossy slabs. By comparing simulation and measurement, the resonant frequencies for the first three harmonics of crosstalk between the baseline and 1.5 S/m lossy material connectors are lowered by a similar amount. However, the material loss model used in simulation greatly overestimates the actual reduction in PSNEXT magnitude that is seen in the measured connector experiment by approximately 5dB. The effect of the 1.5 S/m lossy slabs, in terms of reducing the resonant crosstalk magnitude in measurement, is actually less than 1dB different when compared to the baseline measurements.

Figures 30 and 31 show insertion loss and PSNEXT magnitude spectra for the simulated and measured connectors respectively, comparing the baseline connector and connector with Material A lossy slabs. Comparison of the simulated and measured insertion loss and PSNEXT magnitude spectra for the Material A experiments shows a difference between simulated and measured crosstalk. The change in PSNEXT resonant magnitude between the baseline and lossy material simulation, in comparison with measurement, is similar in that the connector resonant frequencies are shifted lower in frequency. However, the material A simulation loss model generally overestimates the

measured reduction in PSNEXT magnitude. The insertion loss to power sum near-end crosstalk margin for the simulated connector with Material A is larger than the measured connector margin. The full-wave simulation is therefore somewhat inaccurate in reproducing the connector measurement results because reduction in PSNEXT magnitude is overestimated by about 4dB. However, channel insertion loss is practically identical for both the simulated and measured connectors with Material A lossy samples.

Figures 32 and 33 show insertion loss and PSNEXT magnitude spectra for the simulated and measured connectors respectively, which compare the baseline connector and connector with Material B lossy slabs. Material B has a percentage of conductive nickel particles that makes it mildly ferromagnetic. The material has unknown quantified magnetic properties, but was assumed to have a relative real permeability of 1.5 and no significant imaginary permeability components. Comparison of the simulated and measured insertion loss and PSNEXT magnitude spectra of the Material B connectors with the baseline connector shows a difference between simulation and measurement. The change in resonant behaviour between the baseline and material experiments when comparing simulation and measurement is similar for this material in that the connector resonant frequencies are shifted lower in frequency in both simulation and measurement, as was the case with the Material A experiment. The Material B loss model used in simulation generally overestimates the actual reduction in PSNEXT magnitude that is seen in the measured connector experiment. The insertion loss to PSNEXT margin for the simulated connector with Material B is larger than the measured connector margin. The simulated connector is therefore somewhat inaccurate in reproducing the connector measurement results because reduction in PSNEXT magnitude is overestimated by about

3dB at resonant frequencies. However, channel insertion loss is practically identical for both the simulated and measured connectors with Material B lossy samples.

Figures 34 and 35 show insertion loss and power sum near-end crosstalk magnitude spectra for the simulated and measured connectors respectively, comparing the baseline connector and connector with CRS-124 lossy slabs. When comparing the simulated and measured connector insertion loss and PSNEXT magnitude spectra of the CRS-124 experiments, the results are very similar where the resonant crosstalk is reduced in frequency and the magnitude of PSNEXT is reduced. The CRS-124 loss model used in simulation generally reproduces the reduction in PSNEXT magnitude that is seen in the measured connector experiment within 2dB. The insertion loss to PSNEXT margin for the simulated connector with CRS-124 is similar to the measured connector margin and agrees within 2dB of measurement. The channel insertion loss is practically identical for the simulated and measured connectors with CRS-124 lossy material samples. The CRS-124 material also causes the insertion loss to begin a gradual roll-off at a lower frequency than is seen in the baseline connector, at approximately 6GHz.

Figures 36 and 37 show insertion loss and power sum near-end crosstalk magnitude spectra for the simulated and measured connectors respectively, comparing the baseline connector and connector with MCS lossy slabs. A comparison of simulated and measured connector insertion loss and PSNEXT magnitude spectra of the MCS experiments, the results are practically identical to the results obtained from the CRS-124 connector measurement and simulation.

To summarise the magnitude spectra of the measured and simulated connectors, the insertion loss characteristics of all of the connectors in the baseline and material

experiment configurations, present an almost identical transmission channel with the exception of enhanced insertion loss rolloff above 6GHz for the CRS-124 and MCS. For the reduction of PSNEXT in comparison of simulation to measurement, it was shown that with the loss models in simulation for lossy material, PSNEXT reduction in the 1500 S/m material simulated connector is underestimated. The reduction of PSNEXT is overestimated for the simulated connectors with 1.5 S/m material, Material A and Material B lossy material slabs. Simulation of the baseline connector and lossy material experiments using the CRS-124 and MCS materials agree well with measurement. Measured connectors with lossy material samples are listed in ascending order of effectiveness in reducing PSNEXT as follows: 1) σ =1.5 S/m material, 2) σ =1500 S/m material, 3) Material A (σ =45 S/m), 4) Material B (σ =31 S/m; unknown magnetic properties), and 5) CRS-124 and MCS.

4.4 Eye Patterns from Simulated & Measured Data: 10.6Gbps

An eye pattern provides the voltage level crossings for a periodic sampling interval when data symbols are transmitted through a system. For this study the data symbols are bits of a polar NRZ data stream. Crosstalk interference sources in a connector transmission line will be due to arbitrary wave shapes, amplitudes, and data rates. However for this study a data rate of 10.6Gbps from a random polar NRZ input waveform is be used for the transmission channel as well as for neighbouring crosstalk interference sources in the connector. To provide for optimal recovery of data, a received bit pattern through a transmission line channel will be sampled at a periodic interval where the eye pattern has a maximum height. Decision feedback equalisation hardware

algorithms can be used to "widen" eye patterns and therefore improve the BER performance of the channel. They will not be discussed here as they are outside the scope of this thesis.

The eye patterns for the raw measured and simulated connector experiments will be examined for two purposes. The first purpose is for comparative analysis of the accuracy of the simulated connector and the measured connector experiment performances. Specifically, the utility of conventional dielectric loss models to model the loss mechanisms within quasi-conductor and ferrite-dielectric lossy materials will be examined. The second purpose is to use statistical data from the measured connector eye diagrams to conduct communication channel analysis on the connector experiments and determine performance metrics of the connector systems.

4.4.1   Channel Eye Patterns as Transfer Function Output

S-parameter transfer functions of the measured and simulated connector experiments were used to create a time domain response for an input 10.6Gbps polar NRZ pulse train with 5000 bit intervals and 1 volt swing centered around 0 volts. The input 10.6Gbps pulse train is excited at port 15 (Figure 18), is transmitted through connector line 8 (Figure 12), and the output waveform is recorded at port 16 (Figure 18). The 10.6Gbps pulse train waveform is also transmitted through all the crosstalk contributor s-parameter transfer functions onto line 8, and the crosstalk output waveforms are recorded. The crosstalk sources have a cumulative superposition effect on the output eye pattern.

As an illustration of transfer functions in the connector, Figure 38 and Figure 39 respectively show an example insertion loss and an example of crosstalk magnitude as a function of frequency. These transfer functions for the connector were obtained from the connector S-parameters.

Channel insertion loss
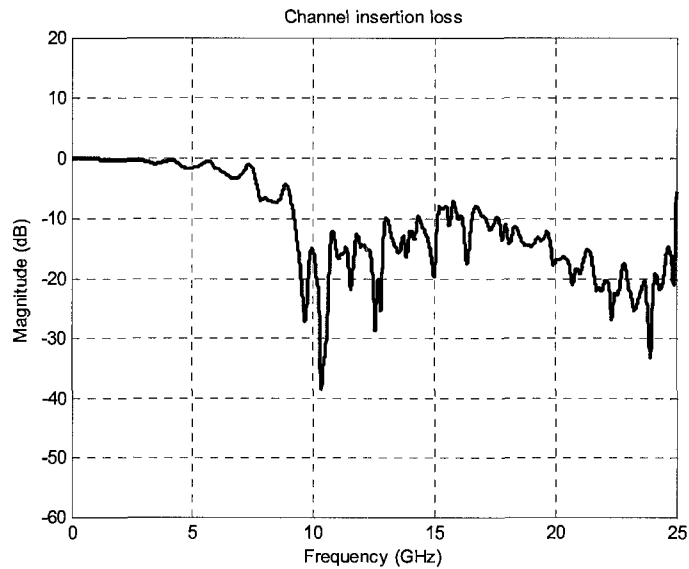
Figure 38: Example of connector insertion loss transfer function magnitude, from input port 15 to output port 16.
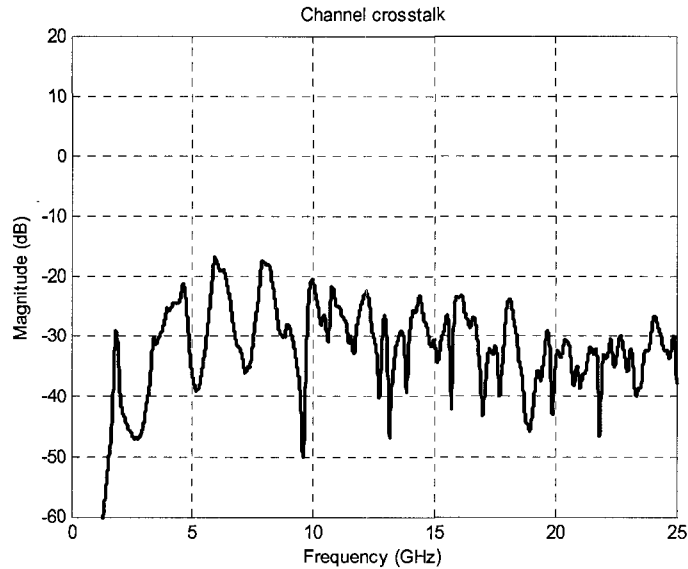
Figure 39: Example of connector crosstalk transfer function magnitude, from input port 2 to output port 16.

As the crosstalk and insertion loss spectra of the connectors were obtained from the s-parameter data, and since the magnitude does not decay to zero at high frequencies, the transfer functions are naturally brick wall-filtered by the measurement range of 0-25GHz. Due to the brick wall filter of the s-parameter spectra, the output time domain signals have undesirable $\sin(x)/x$ ringing. In order to reduce this ringing in the time domain output signal, a raised-cosine filter was used on all of the connector transfer functions. Raised-cosine filtering was applied to the frequency range of 21GHz to 25GHz of the connector S-parameters, and was used to avoid attenuation of the first and second spectral harmonics of the 10.6Gbps input signal. Examples of the insertion loss and crosstalk transfer functions with raised-cosine filtering are shown in Figure 40 and Figure 41 respectively.
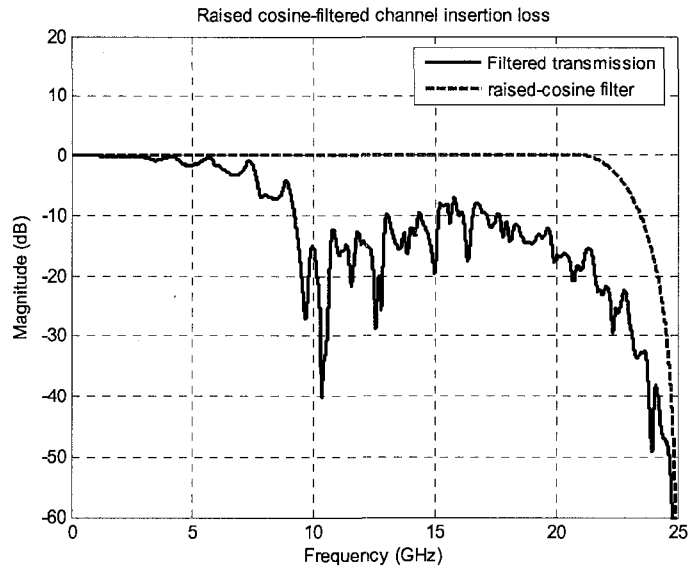
Figure 40: Magnitude plots of example insertion loss and raised-cosine filter transfer functions.
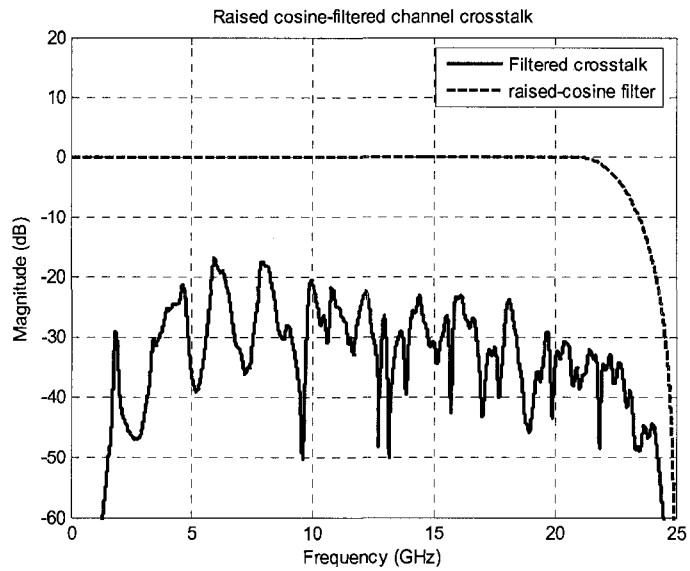
Figure 41: Magnitude plots of example crosstalk and raised-cosine filter transfer functions

The magnitude of the 10.6Gbps input polar NRZ waveform spectrum, connector

transfer function, and output waveform spectrum for the same insertion loss and crosstalk

examples are shown in Figure 42 and Figure 43.
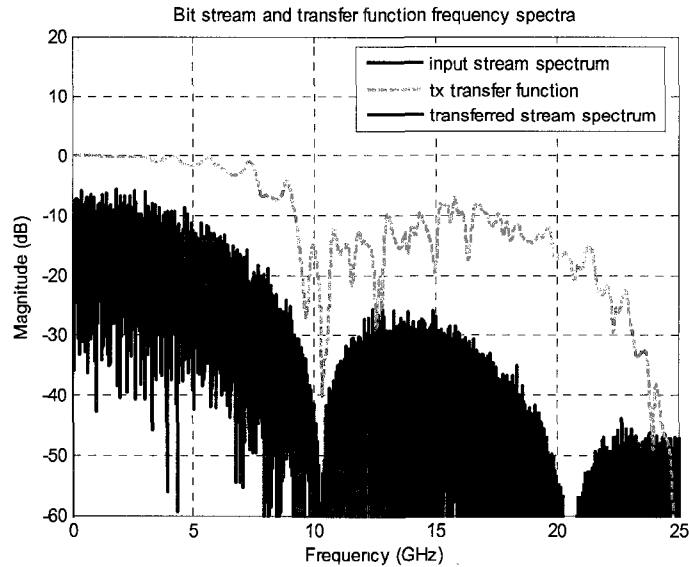
Figure 42: Magnitude plots of example input polar NRZ waveform, filtered insertion loss transfer function, and output 10.6Gbps polar NRZ waveform.
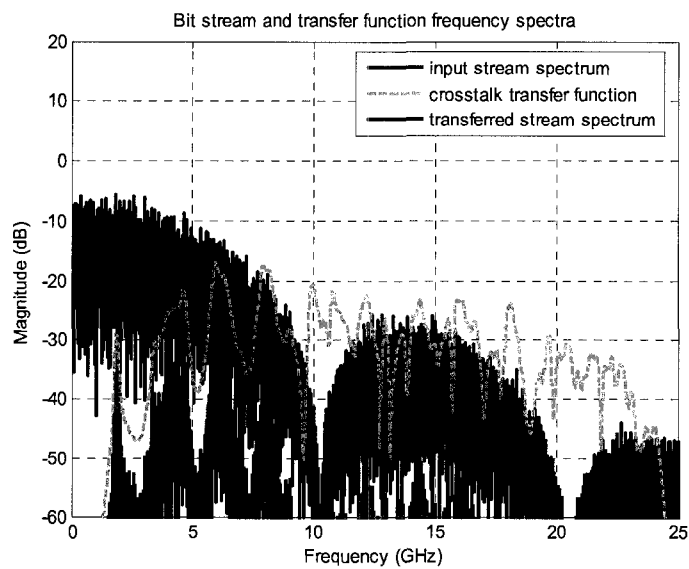
Figure 43: Magnitude plots of example input polar NRZ waveform, filtered crosstalk transfer function, and output 10.6Gbps polar NRZ waveform.

The time domain response of the input and output bit streams for the same

example transmission and crosstalk transfer functions using the inverse discrete Fourier

transform are shown in Figure 44 and Figure 45.
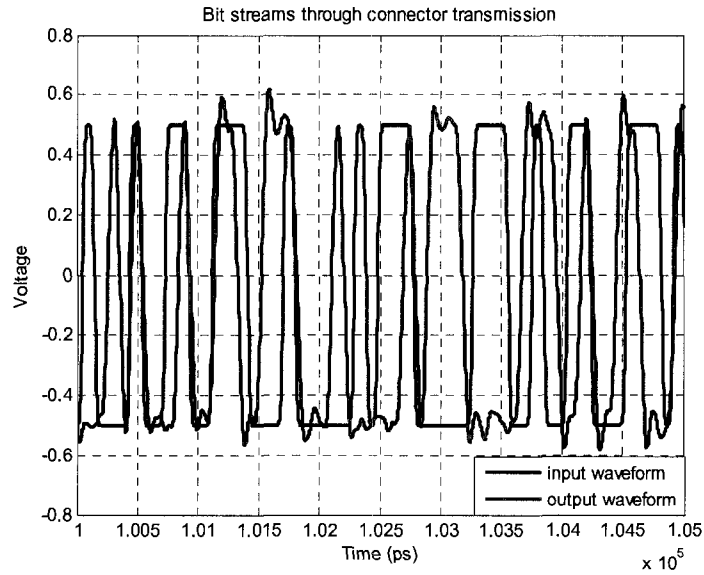
Figure 44: Inverse discrete Fourier transform waveform of the 10.6Gbps polar NRZ binary waveform input and output for the example insertion loss transfer function.
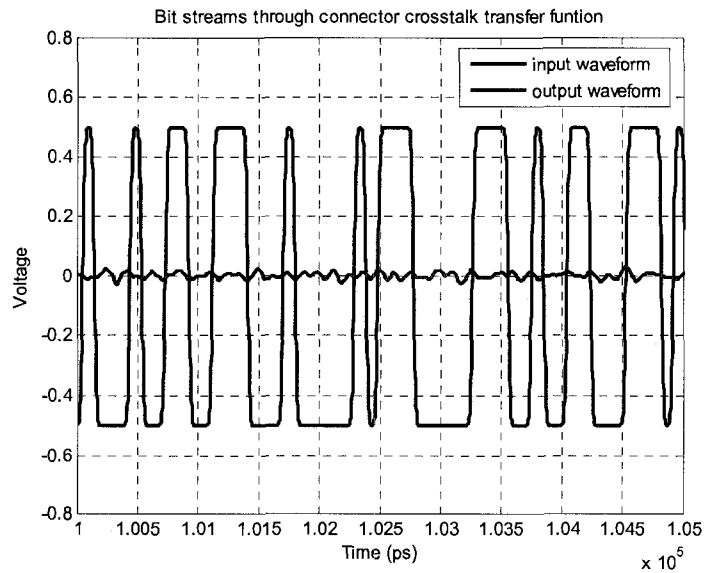
Figure 45: Inverse discrete Fourier transform waveform of the 10.6Gbps polar NRZ binary waveform input and output for the example crosstalk transfer function.

The output time domain response of the input bit stream through the connector

transmission channel (Figure 44) was used to create an eye pattern. An example

transmitted bit stream and eye pattern constructed from it are shown in Figures 46 and 47

respectively.
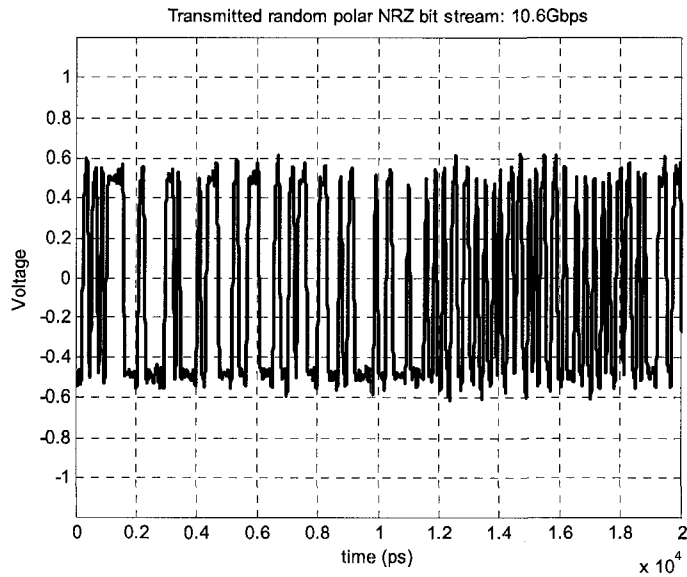
Figure 46: Output 10.6Gbps polar NRZ waveform from the example insertion loss transfer function (transmit).
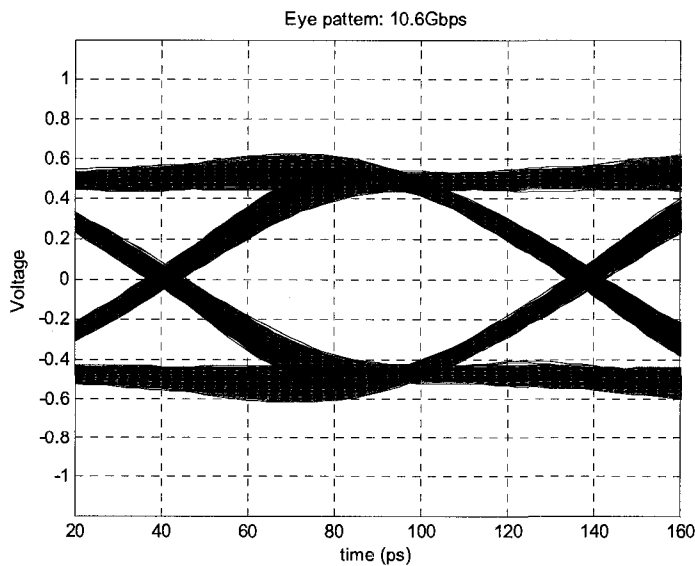
Figure 47: Eye pattern created from the transmitted 10.6Gbps polar NRZ pulse train.

The determination of peak crosstalk amplitude in the time domain within the

connector is of concern since it represents a limitation on the overall channel throughput.

Peak crosstalk within the connector at this data rate was determined by applying the

principle of superposition for each individual source of crosstalk interference onto the

transmission channel, at its peak observed crosstalk amplitude. The peak crosstalk

amplitude was composed by aligning in time the peak observed amplitude of each

individual crosstalk interference source and adding the crosstalk waveforms. The process

of individual crosstalk interference sources being composed into a peak superposition

waveform is shown in Figures 48 and 49.
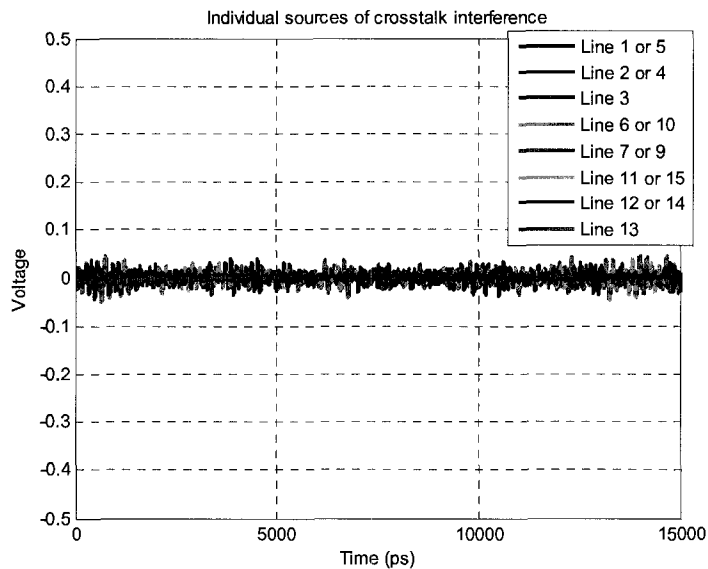
Figure 48: Plots of crosstalk voltage output of individual connector crosstalk sources in the connector with the 10.6Gbps polar NRZ input bit stream.
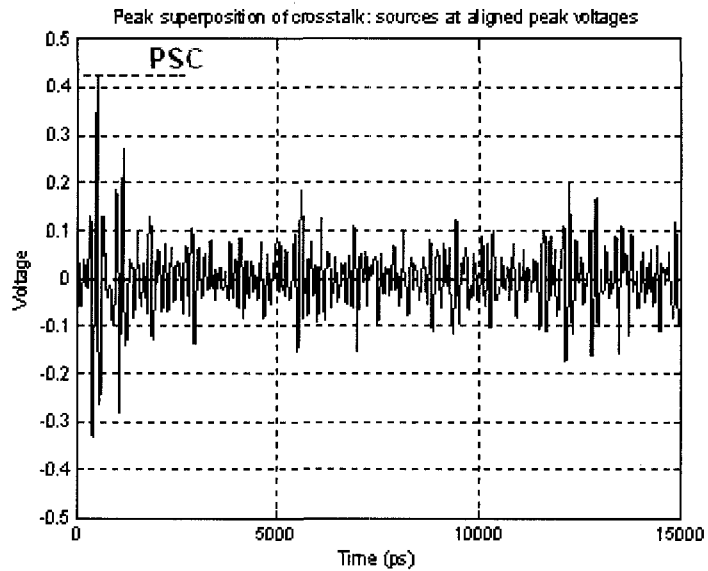
Figure 49: Plot of peak superposition crosstalk on line 8 for example connector, composed from individual crosstalk sources. Marker indicates PSC.

Superposition of peak observed crosstalk amplitude and the transmitted eye

pattern for all of the connector experiments was used to indicate all of the throughput

impairments on the connector channel. Observed peak superposition crosstalk (PSC) on

the transmitted eye pattern for all measured and simulated connector material

experiments is shown in Figures 50 through 63.

4.4.2 Connector Channel Eye Patterns
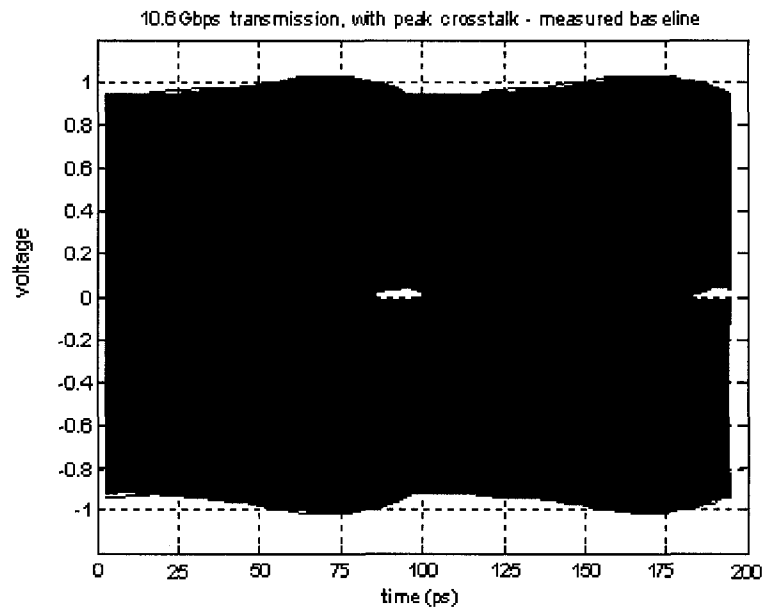
Figure 50: Channel output eye pattern with PSC for the measured baseline connector.
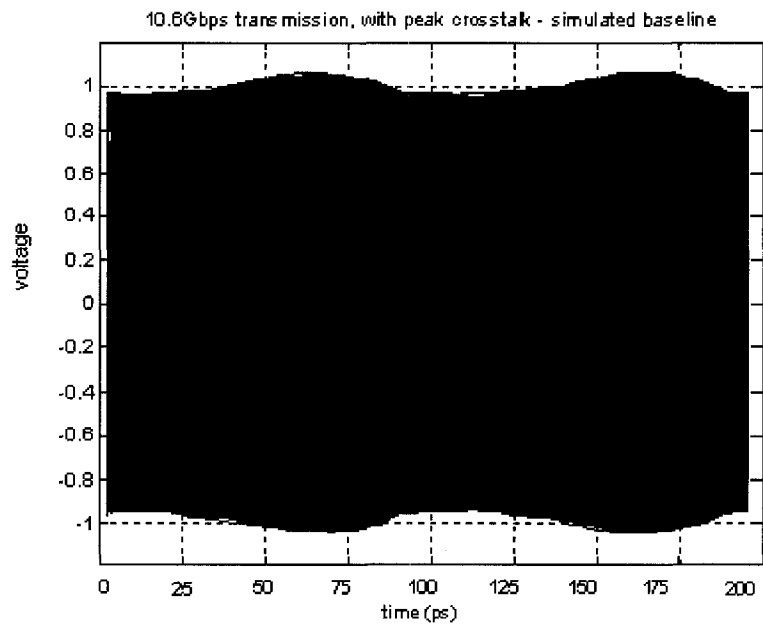
Figure 51: Channel output eye pattern with PSC for the simulated baseline connector.
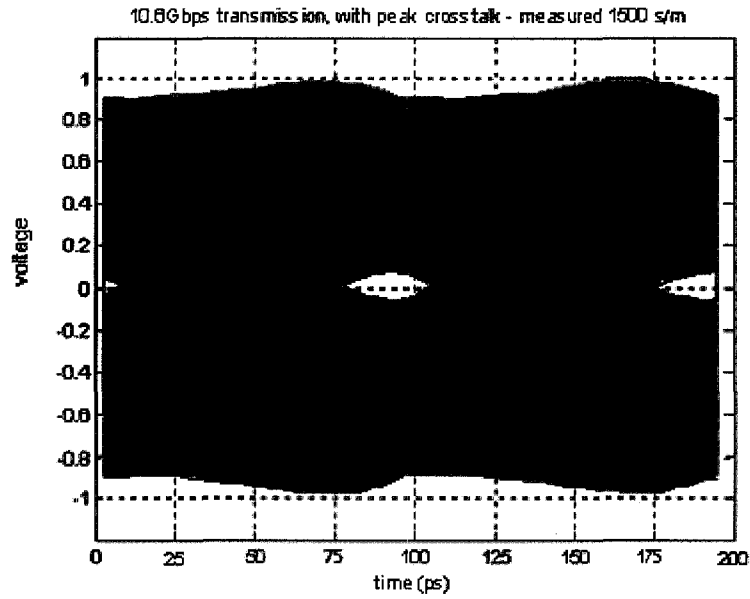
Figure 52: Channel output eye pattern with PSC for the measured 1500 S/m lossy material connector.
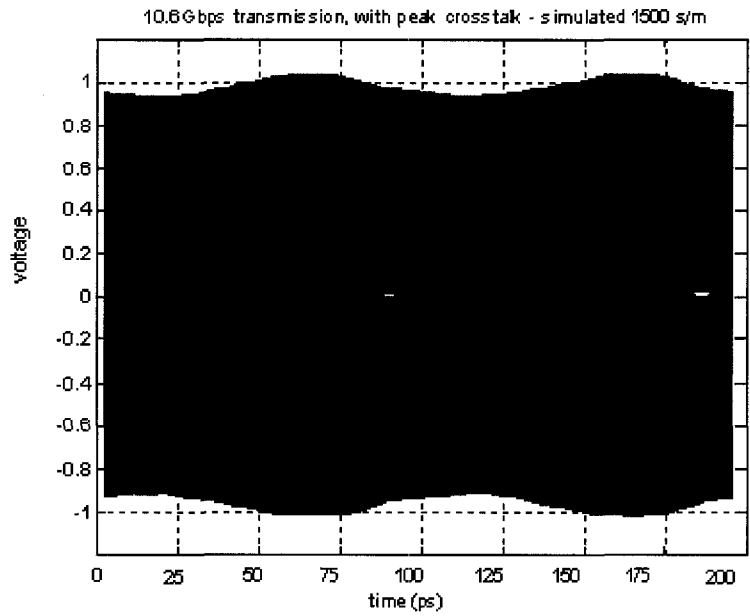
Figure 53: Channel output eye pattern with PSC for the simulated 1500 S/m lossy material connector.
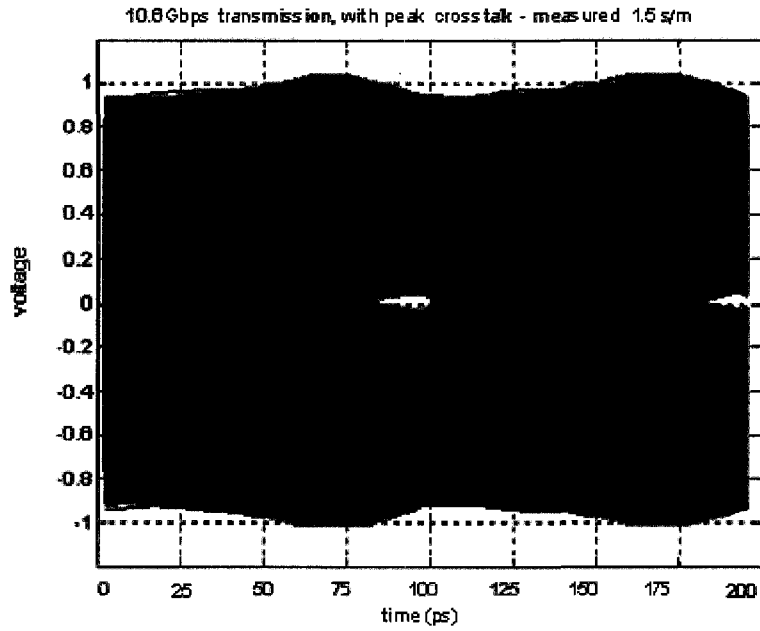
Figure 54: Channel output eye pattern with PSC for the measured 1.5 S/m lossy material connector.
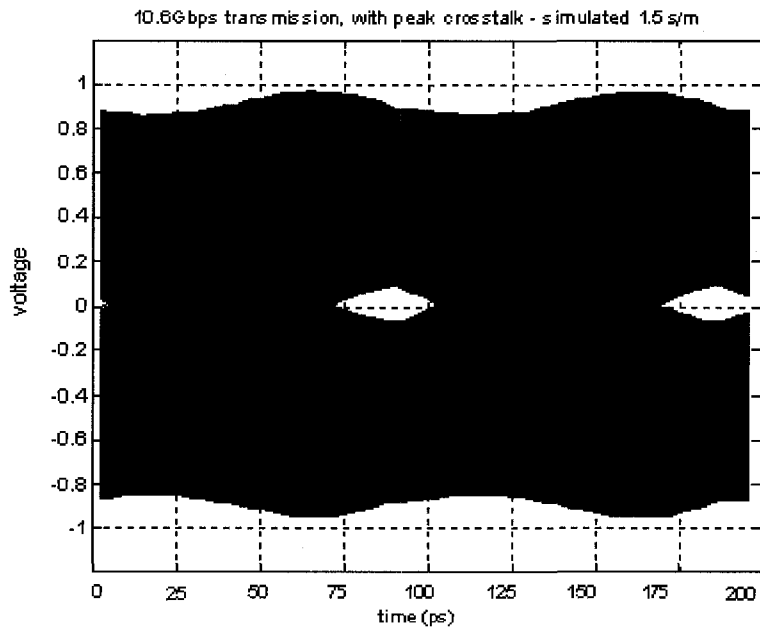
Figure 55: Channel output eye pattern with PSC for the simulated 1.5 S/m lossy material connector.
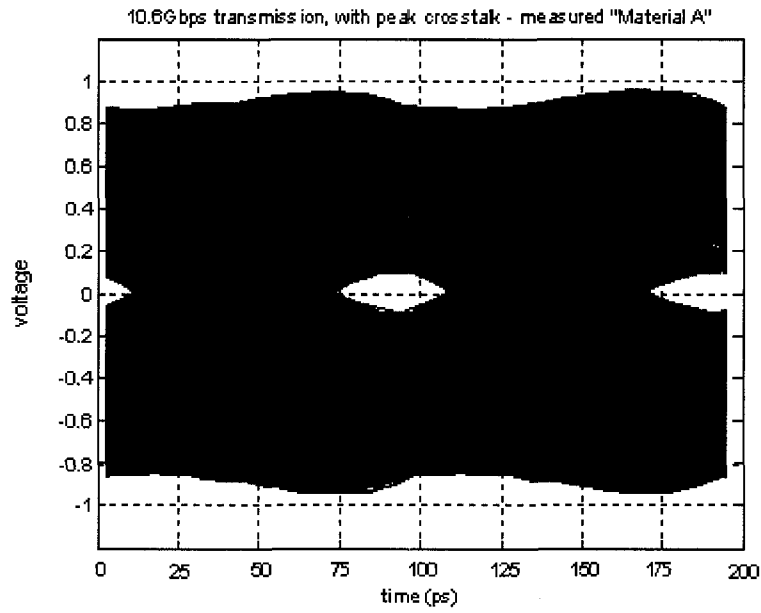
Figure 56: **Channel output eye pattern with PSC for the measured lossy Material A connector.**
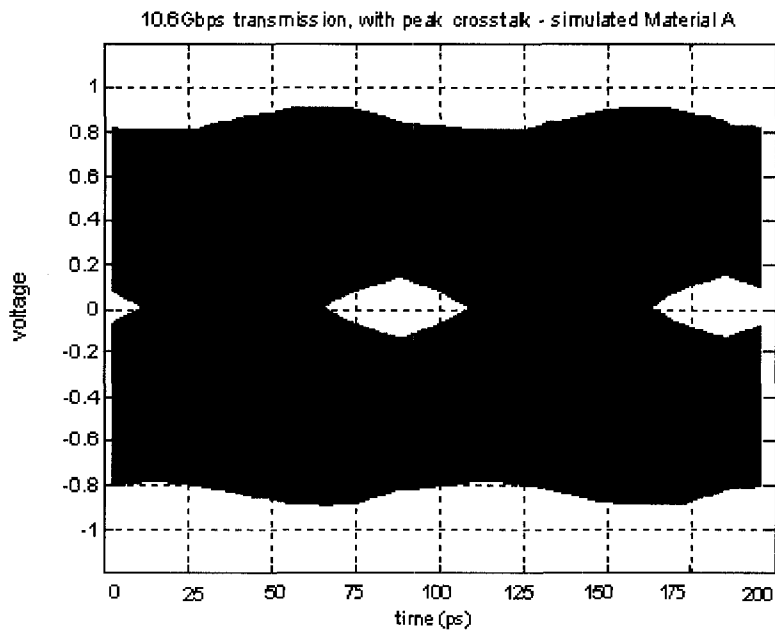
Figure 57: **Channel output eye pattern with PSC for the simulated lossy Material A connector.**
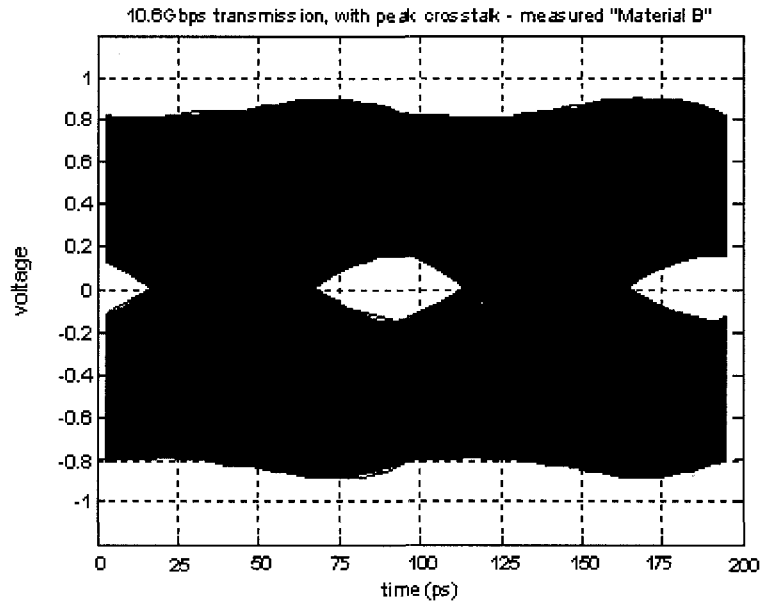
Figure 58: **Channel output eye pattern with PSC for the measured lossy Material B connector.**
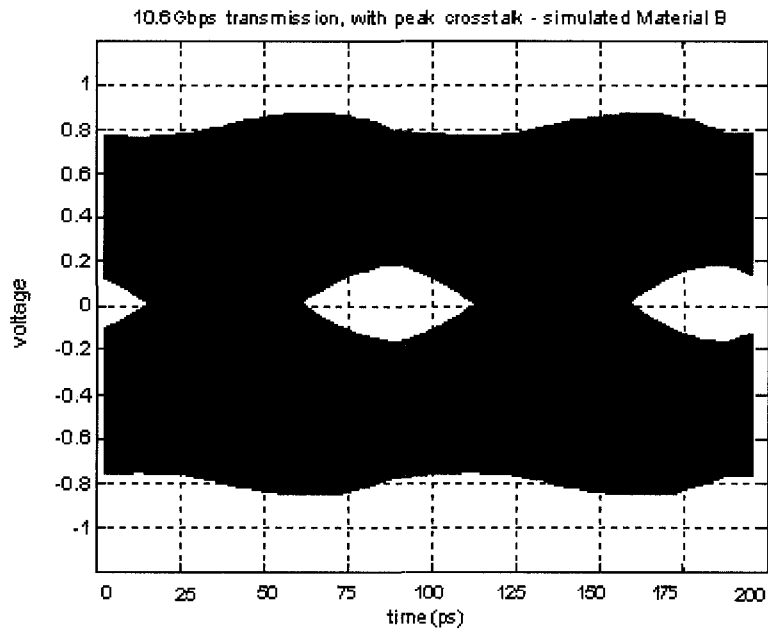
Figure 59: **Channel output eye pattern with PSC for the simulated lossy Material B connector.**

10.6Gbps transmission, with peak crosstalk - measured CRS-124
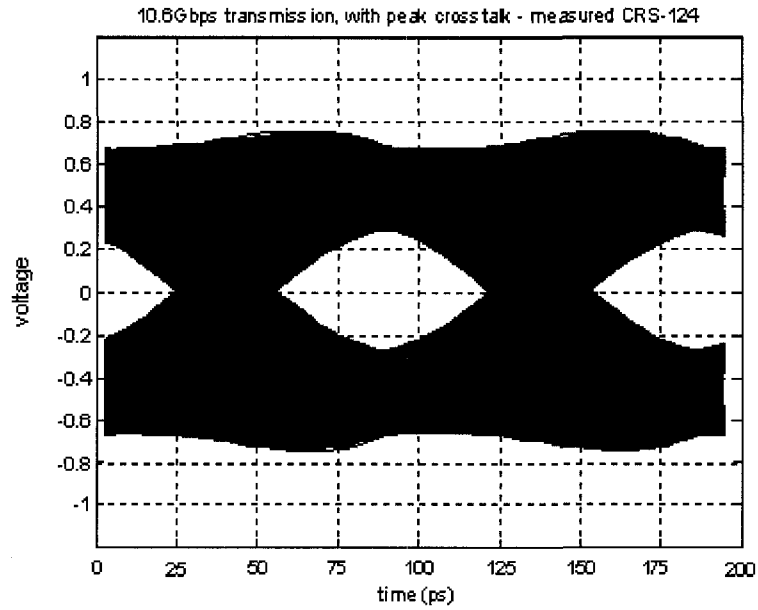
Figure 60: Channel output eye pattern with PSC for the measured CRS-124 lossy material connector.

10.6Gbps transmission, with peak crosstalk - simulated CRS-124
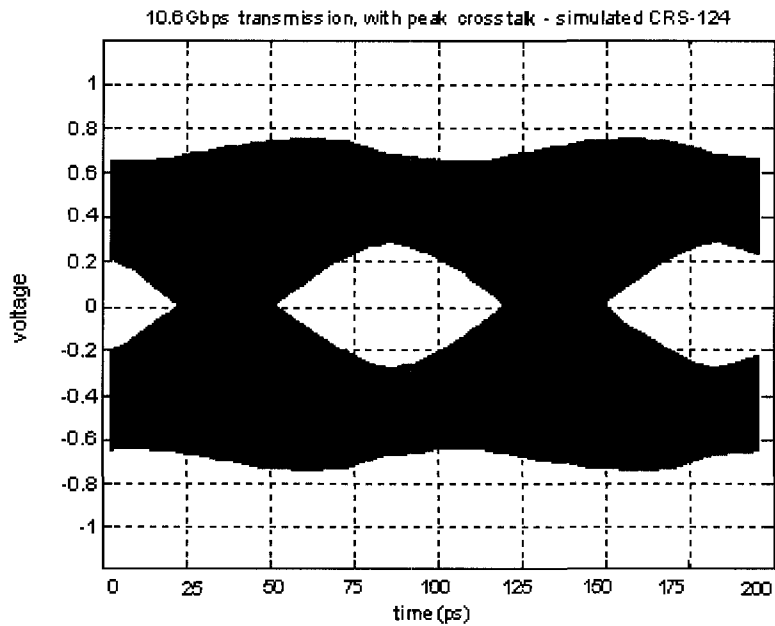
Figure 61: Channel output eye pattern with PSC for the simulated CRS-124 lossy material connector.
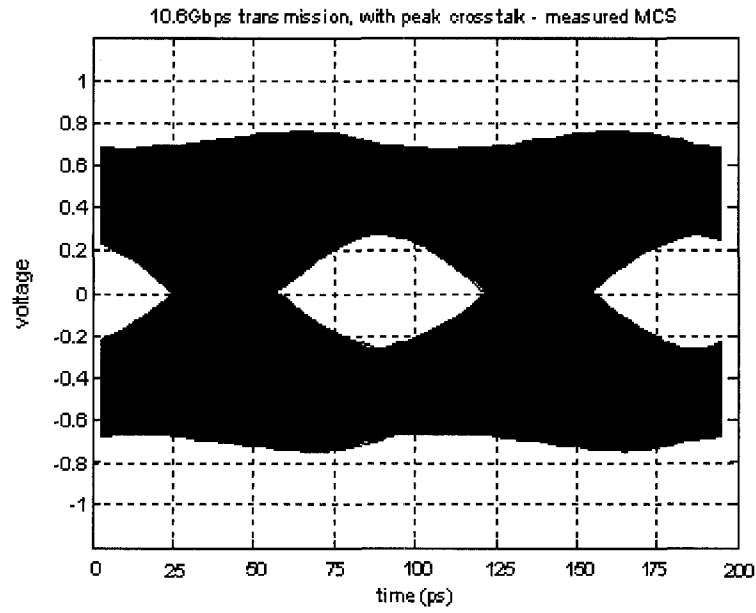
Figure 62: Channel output eye pattern with PSC for the measured MCS lossy material connector.
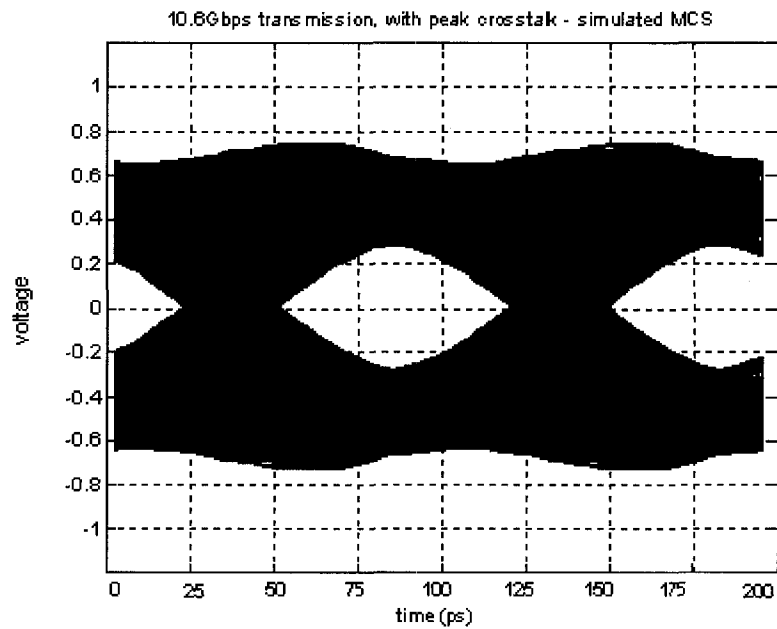
Figure 63: Channel output eye pattern with PSC for the simulated MCS lossy material connector.

The PSC amplitude at 10.6Gbps for the simulated baseline connector was 0.422

volts, compared with 0.402 volts for the measured connector, a 2.47% difference in

amplitude. The difference between the opening of the eye pattern in the simulated and

measured baseline connectors is shown in Figures 50 and 51. For the simulated baseline

connector, the maximum vertical eye pattern opening is 0.57% of the input maximum eye

pattern height. The measured baseline connector was found to have a maximum vertical

eye pattern opening of 5.67% of the input maximum eye pattern height. The discrepancy

in baseline eye pattern opening can be explained by the difference in both the connector

transient impedance in the time domain and return loss in the frequency domain. Figure

64 compares a TDR at the input side of line 8 the baseline connector channel in

simulation and measurement.
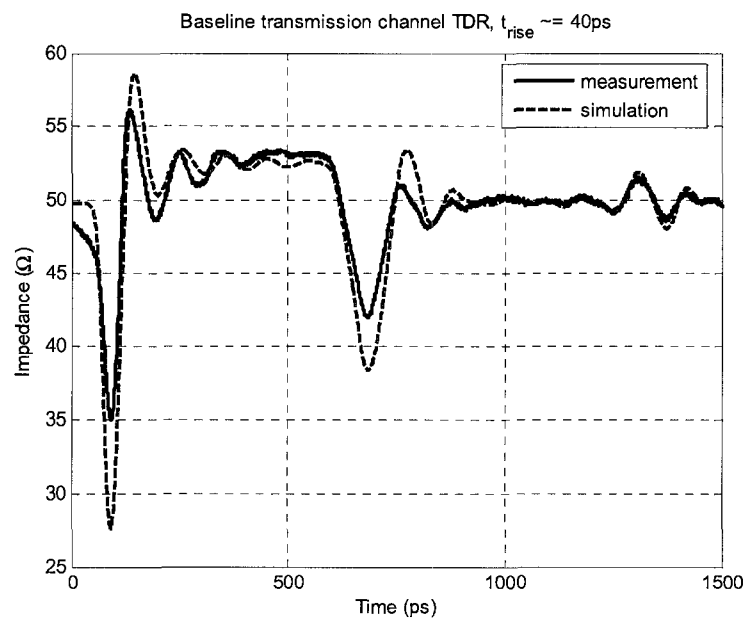
Figure 64: TDR plots of line 8 impedance for the measured and simulated baseline connector.

Both the simulated and measured TDRs were excited with an input step stimulus of similar rise time characteristics, about 40ps 20-80% amplitude rise time. The TDR plots indicate that there is greater reflection and therefore greater impedance mismatch on line 8 in the simulated connector when compared with the measured baseline connector. Mismatch in the connector is observed at the region where the input signal propagates from the SMA input of the connector onto the connector transmission line itself, *i.e.* at the connector launch. The primary reason for the discrepancy in mismatch is how the actual measurement connector launch differs in measured dimension from the nominal design drawings. The simulated connector first observes an impedance hit that is lower than the measured connector impedance. This is because the simulated connector launch was based on manufacturer drawings of an input SMA connector. The simulated connector launch, which is based on nominal drawinigs, indicates a smaller coaxial outer diameter for the input SMA than the true physical dimensions that were measured from the actual manufactured part. Because the simulated coaxial launch outer conductor diameter is smaller in diameter than the measured connector, one would expect the capacitance of this simulated line section to be larger than was measured. Therefore because this section of line in simulation has increased capacitance, the line section impedance is smaller than the measured impedance, *i.e.*

$Z_{sim} = \sqrt{L/C_{sim}} < \sqrt{L/C_{meas}} = Z_{meas}$. The immediately proceeding impedance hit for the connector launch is a high impedance section of transmission line where there is an air gap between the PCB surface ground plane and the connector plate return conductor and therefore an increase in the connector inductance. The discrepancy between simulation and measurement of te high impedance section of the connector launch is a limitation in

simulation mesh density and resultant numerical approximation error. The resonant

characteristics of both the measured and simulated connectors are observed to be

consistent and have similar ringing characteristics.

Figure 65 is the frequency domain steady-state impulse response representation of

the same structure shown with the transient step response in the time domain from Figure

64.
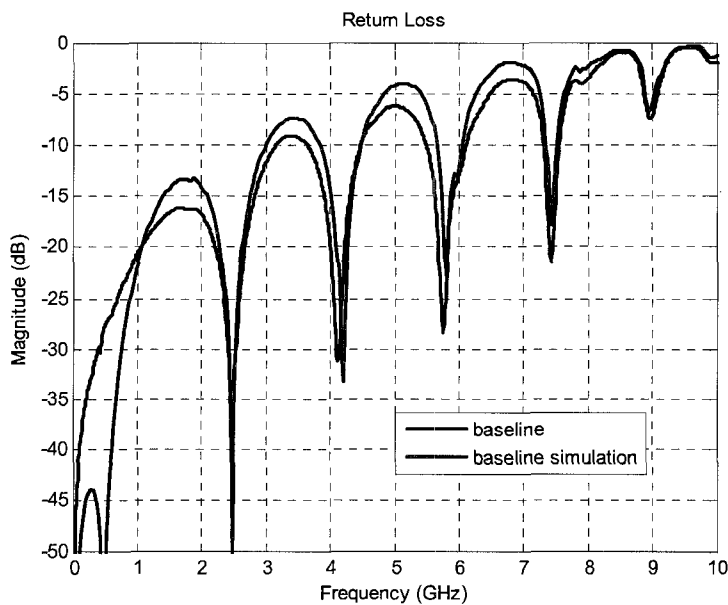
Figure 65: Return loss of line 8 for the measured and simulated baseline connector.

Because there is greater mismatch in the simulated connector, one would expect

the return loss to be larger in magnitude. Because of this, the simulated transmission line

insertion loss is comparatively degraded compared with measurement. A result of

insertion loss degradation is greater attenuation of the input waveform, and subsequent

greater eye pattern closure. If the connector could be given greater mesh density at the

launch air gap and simulated with the corrected coaxial launch dimensions, the simulated

and measured connectors would have greater similarity of S-parameters, transient step

response, and maximum vertical eye pattern height. Because the decibel margin between insertion loss and PSNEXT magnitude for the simulated baseline connector is smaller than the measured connector, a larger channel BER can be expected due to greater simulated eye pattern closure as seen by a comparison of Figure 50 and Figure 51. Excess eye pattern closure for the simulated baseline connector in comparison with the measured eye pattern closure is due to incorrect physical dimensions in full-wave simulation.

Table 5 provides a listing of the simulated and measured connector system eye pattern vertical eye pattern opening values as a percentage of the input eye pattern vertical opening.

Table 5: Comparison of Maximum Vertical Opening of Connector Eye Patterns (with PSC) as a Percentage of Input.

Material	Eye Pattern Height % of input (Simulated)	Eye Pattern Height % of input (Measured)
Baseline	0.57	5.67
1.5 S/m	16.1	5.89
1500 S/m	2.16	14.21
Material A	27.36	19.5
Material B	35.9	30.3
CRS-124	56.95	55.7
MCS	56.36	53.51

If the channel eye patterns of the baseline connector simulation and measurement were identical, then the effectiveness of lossy material modeling in the connector simulations could be determined from the perspective of the overall system, but they are not identical. The mismatch-attributed discrepancy between the simulated and measured baseline connector makes a relative comparison of the overall channel eye pattern difficult since the eye pattern vertical openings are significantly dissimilar. From Table

5, only for the CRS-124 and MCS materials do simulated and experimental eye pattern vertical openings agree. The reason for the discrepancy can be ascribed primarily to incorrect material loss models used in simulation, and to a lesser extent the incorrect modeling of the connector launch. A relative comparison of PSC reduction in the lossy material connector simulations with the baseline connector is useful in determining the effectiveness of the material loss model used.

Since crosstalk is the dominant source of eye pattern closure in the baseline connector, the PSC in a connector at 10.6Gbps may therefore be used as a relative measure of the effectiveness of modeling material loss in connector simulations. The quantity used for relative comparison of the PSC can be expressed as a percentage difference between the PSC values of the simulated lossy material connector and the simulated baseline connector. The percentage change of the simulated PSC can be compared with a measurement percent change counterpart, as shown in Table 6.

Table 6: Connector PSC Percent Change Between Baseline and Lossy Material for Simulated and Measured Connectors.

Material	Connector PSC % Change (Simulated)	Connector PSC % Change (Measurement)	% PSC change Overestimation Difference (Meas-Sim)
1.5 S/m	-11.85	-0.085	11.765
1500 S/m	-2.38	-5.33	-2.95
Material A	-20.45	-9.37	11.08
Material B	-27.14	-18.97	8.17
CRS-124	-51.78	-47.02	4.76
MCS	-51	-45.63	5.37

A PSC percent change in overestimation difference value of 0 would show perfect agreement between simulation and measurement. Values greater than zero indicate overestimation of PSC while values less than zero indicate underestimation of PSC in the

simulation of the lossy material connectors. With the exception of the 1500 S/m material

connector, the reduction in PSC due to the lossy material slabs in simulation is greater

than what is seen in measurement. Simulation of the 1500 S/m material connector

underestimates the measured reduction in PSC by -2.95%. Despite this underestimation

by simulation, the results agree well with measurement. In the lossy material connectors

where reduction in PSC is overestimated by simulation, the results are inaccurate in

varying degrees. For simulation of the connectors with CRS-124 and MCS

nonconductive material slabs, the reduction in PSC is overestimated in simulation by

4.76% and 5.37% respectively, which also agree well with measurement. For the case of

Material B in simulation, material loss is overestimated by 8.17%. Simulation of

Material B agrees somewhat well with measurement, but the value of μ_r' used once

again does not have any basis in measured material parameters. The simulated 1.5 S/m

and Material A connectors were shown to have an excess of overestimated PSC reduction

by 11.765% and 11.08% respectively. The 1.5 S/m material connector is particularly

striking in its inaccuracy since the measured connector showed virtually no reduction in

PSC due to the lossy material slab.

In summary, by using eye patterns it was determined that the channel

performance of the measured baseline connector could be reproduced in the simulator

environment with appropriate modifications in the problem setup. In terms of measured

PSC, the loss effects of the two ferrite-dielectric absorber materials CRS-124 and MCS

and the 1500 S/m quasi-conductor material agree with the measured values, whereas the

remaining simulated materials did not agree with their respective connector

measurements due to the limitations of the material loss model. Since the PSC

determined from simulation data underestimates measurement in the 1500 S/m material experiment, the eye pattern of this simulated connector configuration is much smaller than the channel eye pattern from measurement data. A different electromagnetic propagation loss model for the full wave simulator is necessary for the 1.5 S/m material, 1500 S/m material, Material A, and Material B, as these cannot be accurately modeled as a lossy dielectric with constant σ. Due to this reason, channel performance modeling for the simulated connector configurations was not calculated. From experimental data in Table 5, the connectors with the CRS-124 and MCS materials have the greatest vertical eye pattern opening at about 54.5% of the input and are therefore the most effective materials at reducing crosstalk in the connector. Only the connector configuration with 1.5 S/m material had virtually no effect on reducing PSC and therefore no effect on the channel eye pattern in comparison with the baseline connector. The dominant effect in opening the connector channel eye pattern is the reduction of PSC. The insertion loss of the connector material configurations provide similar transmission channels for the 10.6Gbps signal despite the enhanced rolloff in insertion loss of the CRS-124 and MCS connectors above 6GHz (Figures 35 & 37). This is due to the fact that approximately 75% of spectral energy of the input 10.6Gbps polar NRZ waveform is below 5GHz. Therefore the reduction of PSC in the connector due to lossy materials is primarily responsible for increased vertical eye pattern opening at this data rate.

4.5 Connector BER and the Q-Factor Method

4.5.1 Principles of BER, Q, and Statistical Fitting

The BER of a communication channel can be determined using a variety of approaches, some theoretical and the others being measurement-based methods. The channel BER may be directly computed if the binary state distributions are assumed Gaussian and the corresponding Gaussian characteristics can be determined. Another technique commonly used in fiber optics for characterizing channel throughput is the channel Q-factor method. The Q factor relates approximately the properties of the time domain statistical distribution of voltage crossings at a particular sampling instance of an eye pattern to the raw channel BER, a measure of the received signal. In practice, PCB connectors are designed to have a determinable channel BER of less than 10^{-12}. Figure 66 shows an eye pattern and the assumed Gaussian voltage probability distribution crossings for binary states "1" and "0" at a sampling instance where the vertical opening of the eye pattern of the transmission channel is at a maximum.

$$Q = \frac{\mu_1 - \mu_0}{\sigma_1 + \sigma_0}\bigg|_{\varphi = \pi}$$
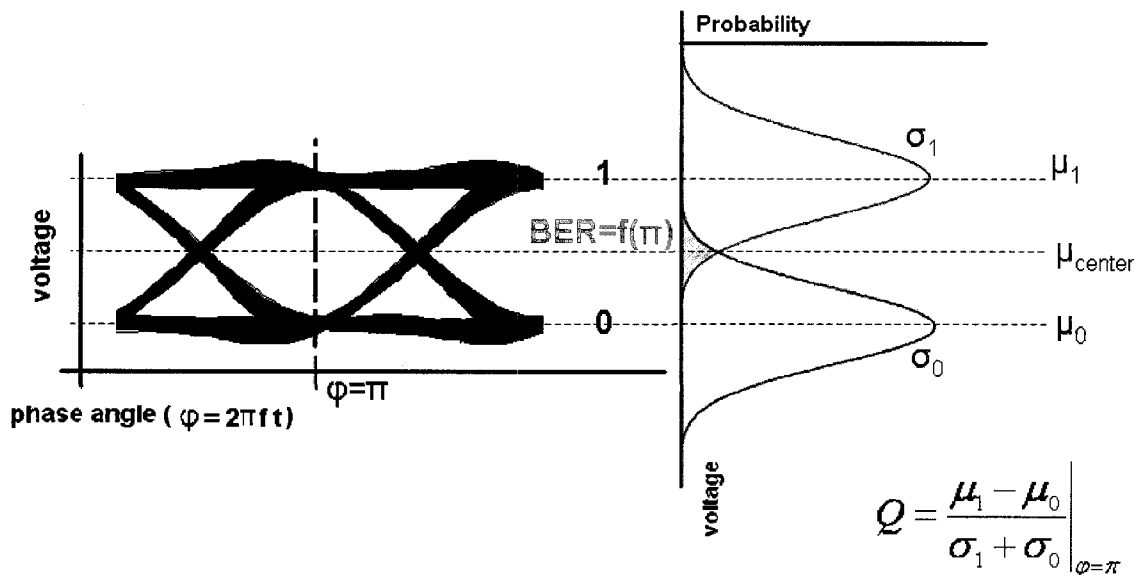
Figure 66: **Transmit only eye pattern and binary state probability density functions.**

76

The probability of a bit decision error for polar NRZ square wave transmission over a channel with white thermal Gaussian noise is given by Equation 4-2 (Couch (2001)),

$$P_{error, polarNRZ} = \frac{1}{2} erfc\left(\frac{A}{\sigma\sqrt{2}}\right)$$
(4-2)

where A is half of the swing amplitude of the antipodal polar NRZ wave shape and σ is the variance of the two binary state probability density functions. In this simple case, the variance of the two binary states is assumed to be identical.

Equation 4-2 can also be decomposed into two equally probable components, resulting in Equation 4-3.

$$BER = \frac{1}{4} erfc\left(\frac{\mu_{center} - \mu_0}{\sqrt{2}\sigma_0}\right) + \frac{1}{4} erfc\left(\frac{\mu_1 - \mu_{center}}{\sqrt{2}\sigma_1}\right)$$
(4-3)

Equation 4-3 expresses the cumulative probability of a decision error for both the binary "1" and "0" states of the transmission channel, where σ_0 and σ_1 are the Gaussian variances of their respective binary states, μ_0 and μ_1 are the respective determined mean voltage levels for each of the binary states, and μ_{center} describes a decision threshold voltage level that is usually the average of μ_0 and μ_1. Equation 4-3 computes the area underneath the intersecting tails of the two binary state probability distribution functions

and assumes *a priori* that the two transmitted binary states in a random bit stream are equally probable. The variances for the two binary distributions in most systems in practice may not always be assumed equal, particularly since the rising and falling edges of a practical square wave pattern generator implementation usually have different shape characteristics, with frequency content that may respond differently to the channel transfer function.

Q is a value used to describe the transmission channel, is shown in Equation 4-4.

$$Q = \frac{\mu_1 - \mu_0}{\sigma_1 + \sigma_0}$$

(4-4)

The channel BER can be approximated in terms of Q [Ramaswami[28]] and is shown in Equation 4-5.

$$BER \approx \frac{\exp(-Q^2 / 2)}{Q\sqrt{2\pi}}$$

(4-5)

To include the effects of crosstalk on the BER of the transmission channel of interest, the above equations for BER and Q can be modified to incorporate the effects of PSC from other transmission lines in the connector at the same data rate. The eye patterns of the various connector measurements from the previous section would then represent the same channel BER described by the modified BER equations.
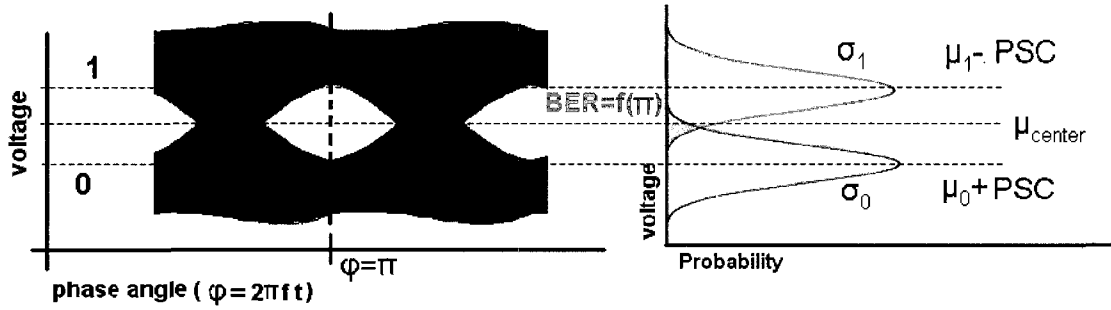
$$Q_{XTALK_{MAX}} = \frac{\mu_1 - \mu_0 - 2 \cdot PSC}{\sigma_1 + \sigma_0}\bigg|_{\varphi=\pi}$$

Figure 67: Binary state probability density functions and channel eye pattern with PSC.

Equation 4-6 is created by modifying Equation 4-3 to include the effect of PSC interference onto the channel of interest.

$$BER_{XTALK_{MAX}} = \frac{1}{4} erfc\left(\frac{\mu_{center} - \mu_0 + PSC}{\sqrt{2}\sigma_0}\right) + \frac{1}{4} erfc\left(\frac{\mu_1 - \mu_{center} - PSC}{\sqrt{2}\sigma_1}\right) \qquad (4\text{-}6)$$

In this modified equation where superposition crosstalk interferes with the transmitted channel, the mean levels μ_0 and μ_1 are simply both shifted inward toward μ_{center} by the magnitude of PSC. The BER of the transmission channel alone is therefore increased by the presence of the maximum observed crosstalk. Equation 4-4 for calculation of Q may similarly be altered as Equation 4-7 to be used with its respective BER approximation formula in Equation 4-5.

$$Q_{XTALK} = \frac{\mu_1 - \mu_0 + 2 \cdot PSC}{\sigma_1 + \sigma_0} \qquad (4\text{-}7)$$

79

The statistical distributions of the binary states were extracted from the measured connector eye patterns shown in section 4.4.2. For the optimal BER of the connector transmission channels with crosstalk, a sample position on the eye pattern horizontal axis was chosen where the vertical opening of the eye pattern is at a maximum for the bit interval. The statistical distribution for the binary states of all the connector material configurations were acquired and individually fit to a Gaussian probability density function with a variance that results in maximum correlation with the statistical data. An algorithm utilizing a range of variances and a covariance technique for determining correlation with the statistical data was used to determine best-fit Gaussian probability density functions. Figure 68 shows an example statistical distribution for a binary state and its best-fit Gaussian probability distribution function.

transmission: no crosstalk ; positive "1" distribution

Voltage level at bit decision time
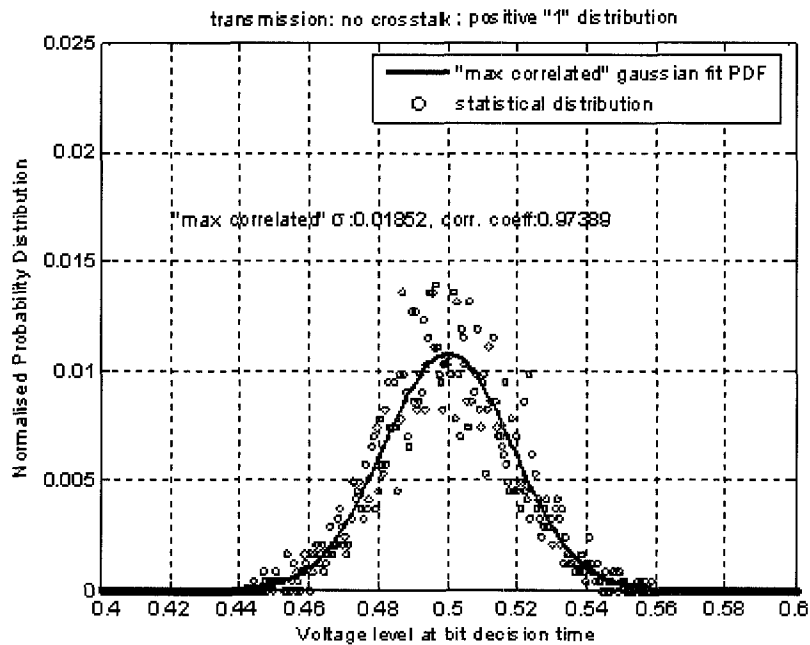
Figure 68: A Gaussian probability density function is maximally correlated with the binary state statistical distribution extracted from an eye pattern at the maximum vertical opening.

With the determination of a Gaussian fit for each binary state distribution,

Equation 4-6 was used to determine the BER of the connector experiment transmission

channels with maximum crosstalk interference.

4.5.2 BER and Q of Measured Connectors

Figure 70 is a plot of the best-fit Gaussian probability density functions for both

binary states in each connector experiment. The plot shows the influence of PSC on the

connector channels.

Positive & negative distributions, adjusted for maximum crosstalk interference
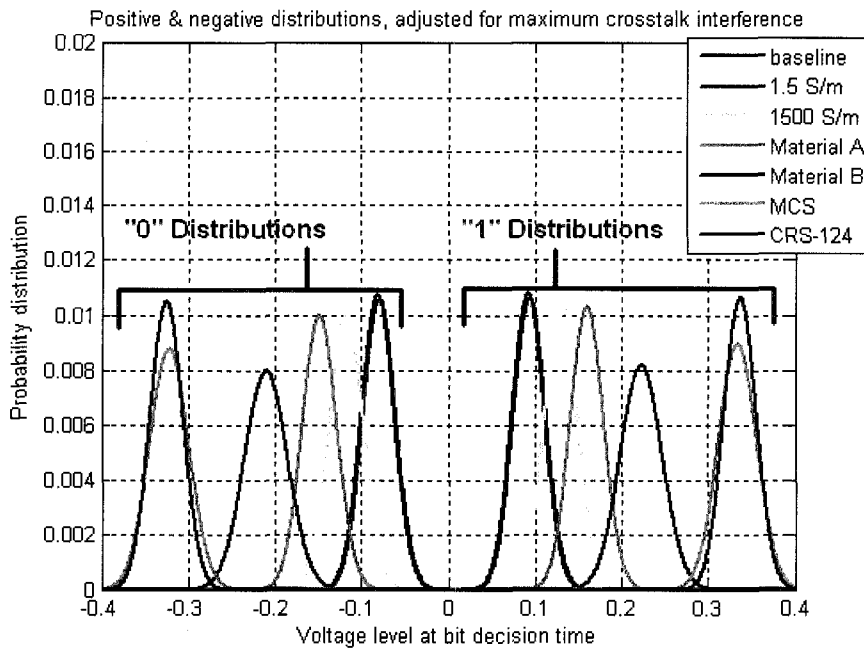
Figure 69: Binary state probability density functions with PSC for the measured connectors.

For the measured connector binary state statistical distributions, the computed

best-fit Gaussian variances and mean voltages are provided in Table 7 along with the

measured connector PSC. The connector configurations are listed in order of descending PSC.

Table 7: Statistical and Channel Quantities for Calculation of BER and Q.

Material	σ_0	σ_1	μ_0 (volts)	μ_1 (volts)	PSC (volts, 1v swing input)
Baseline	0.01883	0.01852	-0.481	0.494	0.402
1.5 S/m	0.01879	0.01859	-0.482	0.495	0.401
1500 S/m	0.01986	0.01889	-0.479	0.492	0.362
Material A	0.01998	0.01933	-0.481	0.493	0.333
Material B	0.025	0.02431	-0.484	0.497	0.274
MCS	0.0227	0.02217	-0.472	0.484	0.15
CRS-124	0.01899	0.01874	-0.47	0.482	0.145

It should be noted that the best-fit Gaussian variance values of the binary state statistical distributions are not identical, and is not known if a greater number of processed bit intervals would increase the similarity of σ_0 and σ_1 for each connector configuration. Also, based on the magnitudes of μ_0 and μ_1, there is apparently a small positive DC offset in the processed data which may be corrected by more processed bit intervals. The BER and Q of the measured connectors are provided in Table 8 using Equations 4-6 and 4-7.

Table 8: BER and Q for Connector Lossy Material Configurations

Material	BER	Q
Baseline	1.83E-06	4.55
1.5 S/m	8.37E-07	4.64
1500 S/m	2.56E-11	6.39
Material A	9.10E-16	7.79
Material B	2.03E-19	8.77
MCS	6.75E-50	14.62
CRS-124	2.72E-70	17.55

The BER of less than 10^{-12} is currently accepted by industry as the threshold value for PCB and silicon devices to operate at, and it is preferable that a passive link can be determined to have a BER that is at least this small. In the baseline connector configuration with bare brass return conductors, the connector channel BER of $1.83 \cdot 10^{-6}$ is not sufficiently enough free of bit errors to be used as a reliable component in a PCB application. For the connector with 1.5 S/m lossy material slabs, the BER of $8.37 \cdot 10^{-7}$ is barely improved over the baseline connector because PSC was reduced by only a miniscule amount. The 1.5 S/m connector also is not sufficiently free of errors. At the BER of $2.56 \cdot 10^{-11}$, the PSC of the 1500 S/m connector is reduced enough that the channel barely fails the 10^{-12} BER requirement. To a varying degree of effectiveness, the introduction of Material A, Material B, MCS, and CRS-124 lossy material slabs reduce the connector PSC sufficiently enough to pass and exceed the BER requirement of 10^{-12} for use as a passive link in backplane hardware.

Although Material A and Material B have bulk conductivities on the same order, improvement in BER and reduction in PSC may either be due to enhanced magnetic loss provided by Material B, or relate to the effective broadband penetration depth of crosstalk surface currents into the material slab. Because the magnetic properties of Material B are not known, it cannot be determined how deeply the crosstalk surface currents penetrate into the material slab.

Since the aim of the study was to find out which of the materials are suitable to minimize the crosstalk interference to improve connector throughput, only approximately 5000 bit intervals were used to obtain the eye pattern. Hence the BER obtained is approximate. A better approximation of the BER can be obtained with a greater number

of bit intervals. The computer memory management of the MATLAB software package used for this study limited the number of bit intervals to only approximately 5000 using a fine 5ps sample resolution. Although the determined "0" and "1" binary state variances for each connector configuration are very similar, they are not identical to each other and therefore the BER approximation is also limited. Additionally, the BER approximation is inherently limited in the assumption of a Gaussian distribution, as Figure 68 shows that the best-fit Gaussian probability density function is significantly different from the statistical distribution in terms of outliers. Additional bit intervals may result in a better Gaussian approximation.

4.6 ICR and Characteristics

The insertion loss-crosstalk ratio (ICR), like Q in the time domain, is a measure of the received signal through a channel in the frequency domain. The ICR is equal to the difference between insertion loss and PSNEXT magnitude.

In this chapter, an ICR linear fitting method similar to that described by IEEE (2006) is used to determine the characteristics of the connector ICR spectra from the measurements.

The channel PSNEXT in decibels is shown by Equation 4-8, where $S_{NEXT,m}(f)$ are the scattering matrix elements for connector near-end crosstalk.

$$PSNEXT(f) = -20\log 10 \sqrt{\sum_m abs(S_{NEXT,m}(f))^2} \qquad (4\text{-}8)$$

The raw channel magnitude ICR is shown in Equation 4-9, where IL(f) is the insertion loss magnitude of the channel.

$$ICR(f) = -IL(f) + PSNEXT(f) \qquad (4\text{-}9)$$

The connector channel ICR magnitude in decibels is obtained by fitting first-order polynomial over the frequency range f_a to f_b.

The average frequency value over the measured log frequency band is calculated by Equation 4-10, where N is the number of sampled points evenly spaced on a linear frequency scale.

$$x_{avg} = \frac{1}{N} \sum_n \log_{10}(f_n) \qquad (4\text{-}10)$$

The average raw channel ICR is computed by Equation 4-11.

$$ICR_{avg} = \frac{1}{N} \sum_n ICR(f_n) \qquad (4\text{-}11)$$

The slope of ICR, m_{ICR}, is shown in Equation 4-12.

$$m_{ICR} = \frac{\sum_n (\log_{10}(f_n) - x_{avg})(ICR(f_n) - ICR_{avg})}{\sum_n (\log_{10}(f_n) - x_{avg})^2} \qquad (4\text{-}12)$$

And the y-intercept value b_{ICR} is computed with Equation 4-13.

$$b_{ICR} = ICR_{avg} - m_{ICR} x_{avg}$$

<div align="right">(4-13)</div>

Hence a linear approximation of the ICR is plotted with Equation 4-14.

$$ICR_{fit}(f) = m_{ICR} \log_{10}(f) + b_{ICR}$$

<div align="right">(4-14)</div>

The frequency range of interest, $f_a = 1GHz$ and $f_b = 5GHz$, was chosen through trial and error when the ICR y-intercept value b_{ICR} for all the connector experiments was observed to be similar, while concurrently a trend of decreasing m_{ICR} was observed to follow the pattern of decreasing computed BER and Q determined in section 4.7.
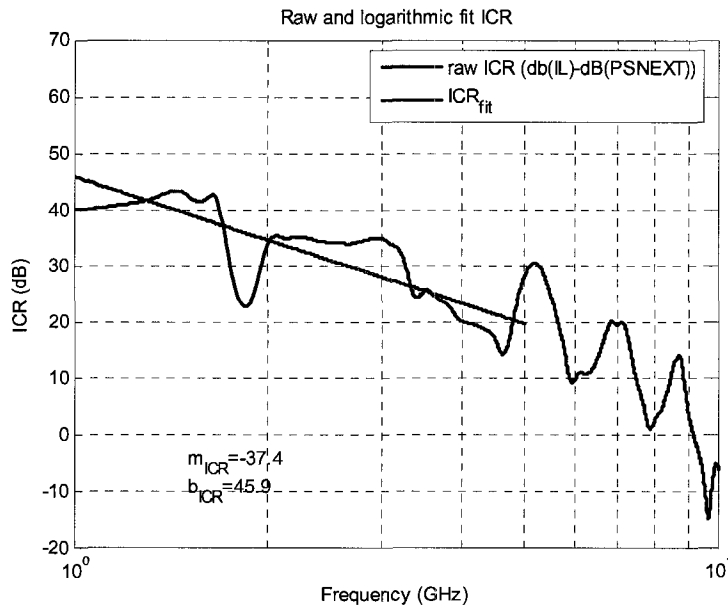
Figure 70: Baseline connector measurement: Raw and logarithmic fit of ICR.
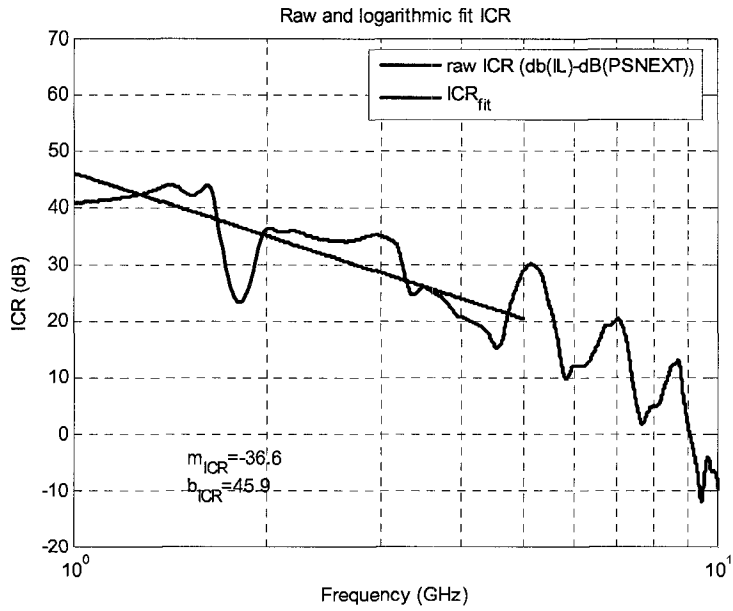
Figure 71: 1.5S/m material connector measurement: Raw and logarithmic fit of ICR.
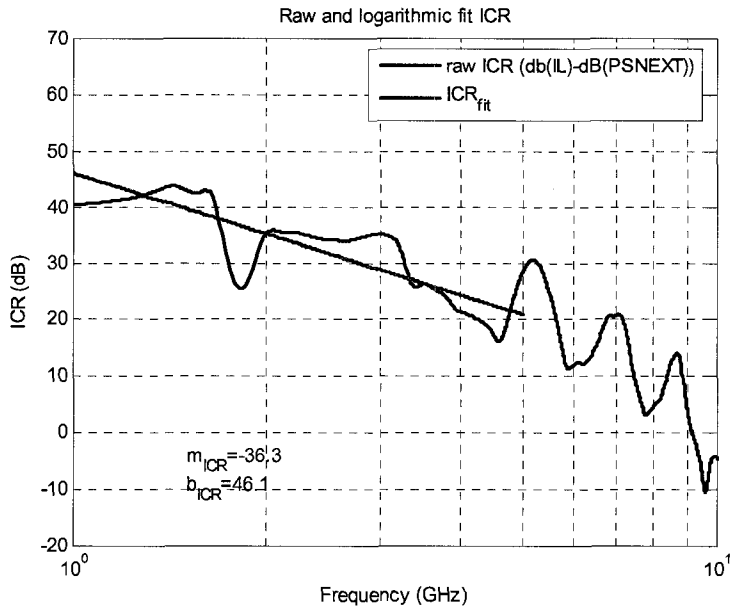
Figure 72: 1500S/m material connector measurement: Raw and logarithmic fit of ICR.
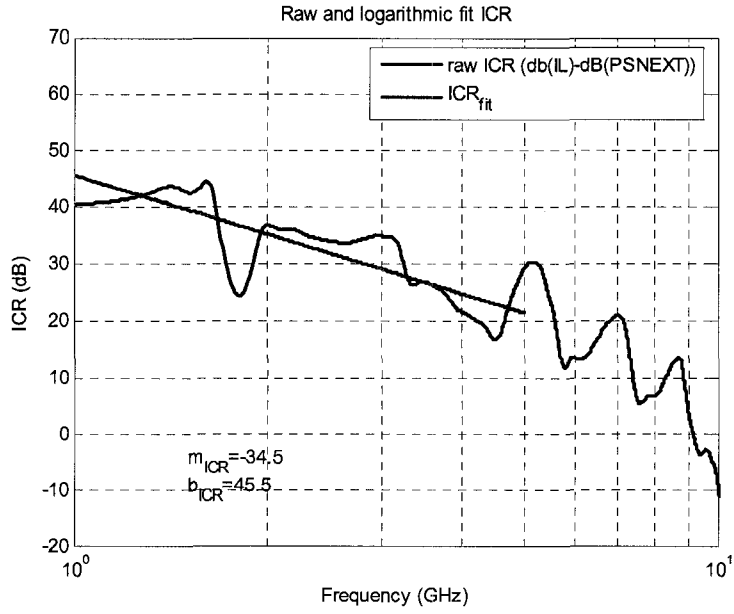
Figure 73: Material A connector measurement: Raw and logarithmic fit of ICR.
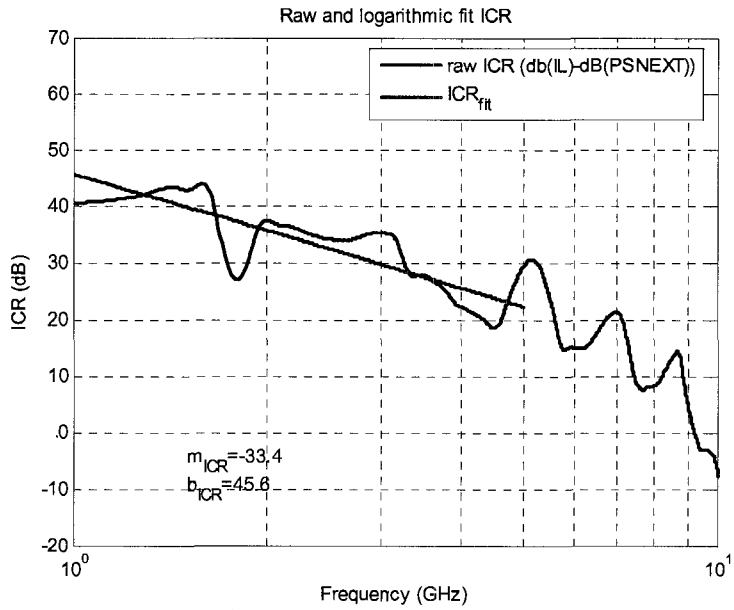
Figure 74: Material B connector measurement: Raw and logarithmic fit of ICR.
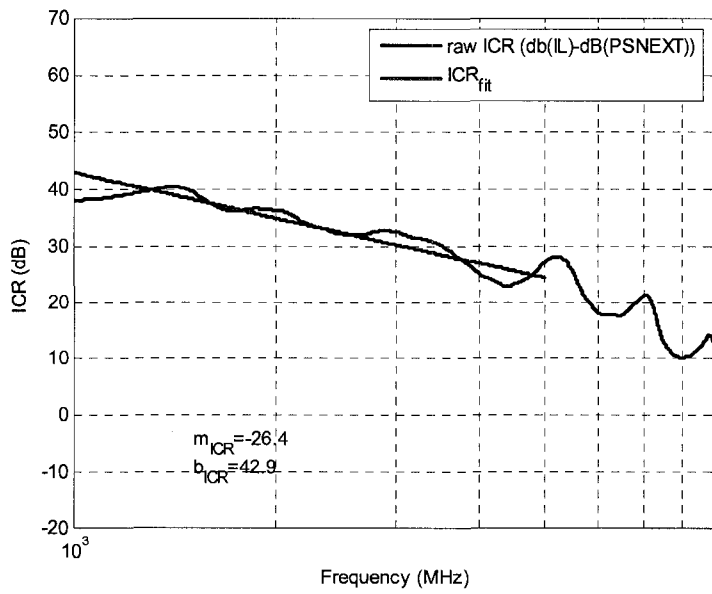
Figure 75: MCS material connector measurement: Raw and logarithmic fit of ICR.
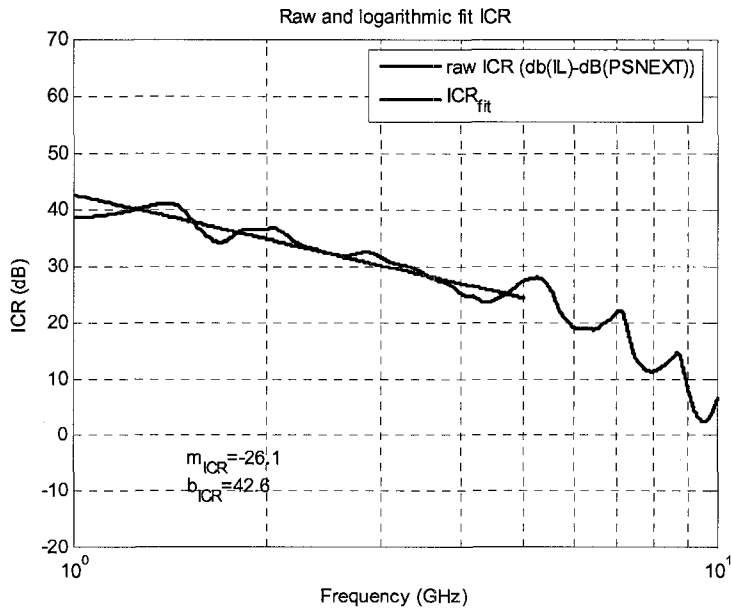
Figure 76: CRS-124 material connector measurement: Raw and logarithmic fit of ICR.

For all of the connector experiments, b_{ICR} at $f_a = 1GHz$ varies from 46.1dB to 42.6dB, where the values in this range are similar in magnitude. It is worth noting that 75% of the signal energy in an input 10.6Gbps polar NRZ bit stream is confined to the 0-5GHz frequency range, and 63% of the input signal energy is concentrated within the 1-5GHz band.

Table 9 compares the m_{ICR}, computed channel BER, and PSC for each connector material configuration. The slope values for m_{ICR} were taken from Figures 72 through 78.

Table 9: Trend of Decreasing m_{ICR} Slope, Connector BER, and PSC.

Connector Material Experiment	m $_{ICR}$	BER	PSC (1 volt input swing)
Baseline	-37.4	1.83E-06	0.402
1.5 S/m	-36.6	8.37E-07	0.401
1500 S/m	-36.3	2.56E-11	0.362
Material A	-34.5	9.11E-16	0.333
Material B	-33.4	2.03E-19	0.274
MCS	-26.4	6.75E-50	0.15
CRS-124	-26.1	2.72E-70	0.145

The slope steepness of m_{ICR} is shown to decrease with decreasing connector channel BER, along with decreasing PSC.

4.7 Relationship Between ICR and Other Channel Performance Metrics

Within these connector experiments and this choice of frequency range for ICR fitting, the ICR slope m_{ICR} has a relationship to connector BER in that they decrease together. The m_{ICR} for any arbitrary lossy material sample in this experimental

connector can have an associated BER, Q, or eye pattern height if a trend line or function

is fit to the material sample experiments in this thesis. A function can be assumed with

ICR slope m_{ICR} as the input and a variety of scalars as the output metric on the condition

that b_{ICR} remains similar, or below some threshold value. The log of the connector

channel BER can be approximated by a linear relationship with m_{ICR} as shown in Figure

77 for the different connector configurations at 10.6Gbps.
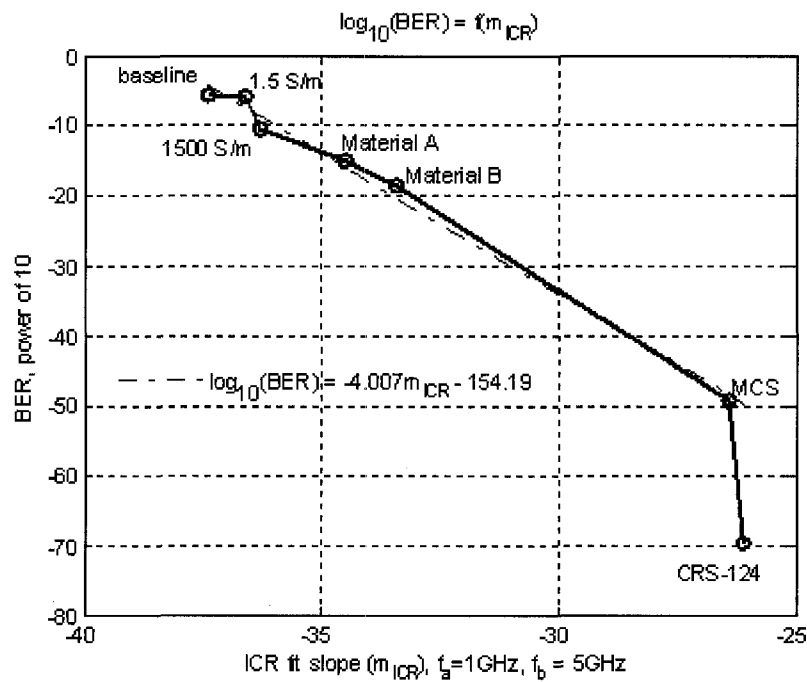
Figure 77: Graph showing a relationship between m_{ICR} and calculated BER at 10.6Gbps.

$$\log_{10}(BER) = -4.007 m_{ICR} - 154.19 \tag{4-15}$$

Equation 4-15 provides a piecewise linear approximation of the log of

experimental connector channel BER as a function of m_{ICR}. The CRS-124 material

experiment does not conform to the linear approximation of Equation 4-15.
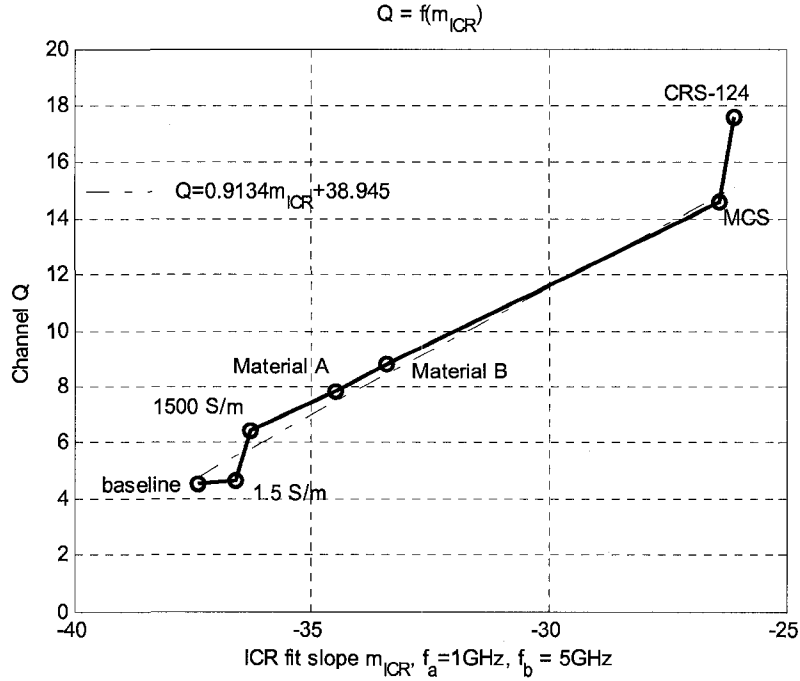
Figure 78: Graph showing a relationship between m_{ICR} and channel Q at 10.6Gbps.

The connector channel Q as a function of m_{ICR} is shown in Figure 78. Q is a measure of the received signal through the connector channel, and is another way to approximately represent the connector channel BER. The polynomial in Equation 4-16 provides a piecewise linear relationship between Q and m_{ICR} of the experimental connector channel material experiments.

$$Q = 0.9134 m_{ICR} + 38.945 \qquad (4\text{-}16)$$

As was the case with Equation 4-15, the Q as a function of m_{ICR} for the CRS-124 material experiment does not conform to Equation 4-16.
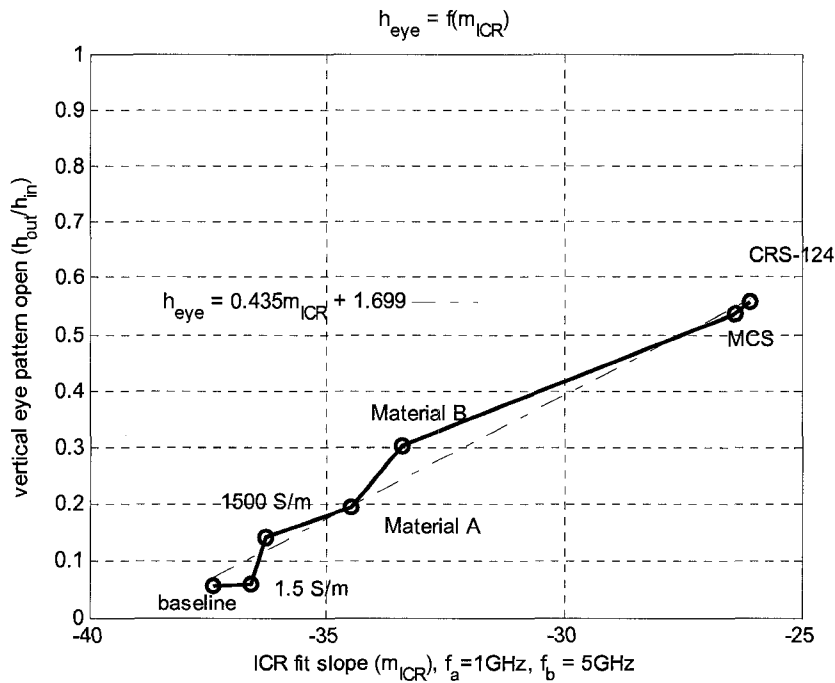
Figure 79: Graph showing a relationship between m_{ICR} and maximum height of channel output eye pattern at 10.6Gbps.

The connector channel output vertical eye pattern height as a function of m_{ICR} is shown in Figure 79. The output vertical eye pattern opening, or eye height, was found approximately to be a linear function of m_{ICR}. This linear relationship is provided in Equation 4-17.

$$h_{eye} = 0.435 m_{ICR} + 1.699 \tag{4-17}$$

In summary, chapter 4 presented simulation and measurement data. The effect of lossy materials on channel performance was also discussed.

CHAPTER V

CONCLUSIONS & FUTURE WORK

5.1 Conclusions

In section 5.1.1 the accuracy of connector simulation in relation to measured

insertion loss and reduction of crosstalk in terms of S-parameters is discussed. In section

5.1.2 the effectiveness of the lossy materials on reducing crosstalk in measurement of the

connector, and the resultant improvement of system performance is discussed.

5.1.1   Simulated and Measured Connectors

As was shown in Section 4.3.2, the connector S-parameters were used to

determine similarity of the simulations to measurement. The S-parameters obtained

from simulation of connector insertion loss for all of the connector material

configurations agree closely with the measured values. The effect on total crosstalk due

to the lossy materials was evaluated by plotting the PSNEXT of the connectors from s-

parameter crosstalk magnitudes in the frequency range of 0 to 10GHz. In the case of the

baseline connector and the connector with ferrite-dielectric materials CRS-124 and MCS,

the S-parameters obtained from simulation agreed with measurement within 1dB to 2dB.

The CRS-124 and MCS material losses are accurately modeled since the complex

permeability and permittivity values of these materials were available. Simulation of the

remaining connectors with the quasi-conductor 1500 S/m material, 1.5 S/m material,

Material A (45 S/m), and Material B (31 S/m; magnetic) agree with measurement of

PSNEXT only within 2dB to 5dB. Therefore the constant conductivity loss model does not accurately model crosstalk reduction in the quasi-conductor materials

The disagreement of 2dB to 5dB with connector PSNEXT between simulation and measurement for the connectors with quasi-conductor lossy materials translates over as a dramatic effect on PSC in the time domain at the data rate of 10.6Gbps. PSC in the connector was also determined to be the primary source of eye pattern closure. A comparison of percentage change between simulated and measured connectors from Table 6 showed an underestimation of loss in simulation for the 1500 S/m material, and overestimation of loss in simulation for the 1.5 S/m material, Material A, and Material B. The underestimation of PSC reduction from simulation for the 1500 S/m material yields an eye pattern closure that is greater than what is measured, resulting in artificially large channel BER in comparison to eye patterns from measurement data. Similarly the overestimated PSC reduction from simulation of connectors with Material A, Material B, and the 1.5 S/m material yields artificially large eye pattern openings that underestimate BER calculated from measurement data. This error in crosstalk estimation can be ascribed to the inaccuracy of the constant conductivity dielectric loss model used for the quasi-conductor materials.

As shown in Table 6, simulation of the connectors with CRS-124 and MCS materials overestimated PSC reduction by approximately 5% in comparison with measurement. However since the CRS-124 and MCS materials in simulation and measurement have very little crosstalk, the eye pattern closure due to crosstalk in these connector material configurations is less than all the other material configurations. The

overall channel output eye pattern for the simulated and measured eye patterns from the CRS-124 and MCS material connector configurations are all practically identical.

5.1.2 Measured Connector System Performance Metrics

At the data rate of 10.6Gbps the BER and Q for the measured connectors was calculated. The baseline connector was found to have the highest BER of the different connector configurations since it had only an air dielectric. The lossy materials can be ranked in ascending order of effectiveness in reducing the connector BER as follows: 1.5 S/m material, 1500 S/m material, Material A, Material B, MCS, and CRS-124. Table 8 lists the BER values from the connector measurement data when 5000 bit intervals were transmitted through the channel. The computed BER of the connectors with MCS and CRS-124 material are essentially the same since both BER values are exceptionally low. Of the lossy materials measured in the connectors, only the 1.5 S/m material and 1500 S/m material did not reduce the connector PSC sufficiently enough to make the BER less than 10^{-12} for use as a passive channel in backplane hardware.

Although the MCS and CRS-124 materials were the most effective in reducing crosstalk interference in the connector channel, the high-performance ferrite particles used in these materials are quite expensive and proprietary. It was shown that crosstalk can be reduced in the connector channel significantly enough to make the BER less than 10^{-12} with inexpensive carbon and nickel particle-filled insulators that are bulk quasi-conductors, *viz.* Material A & Material B.

The connector frequency domain data was used to determine a linear approximation of the channel ICR for all of the connector lossy material configurations in

the frequency range of 1GHz to 5GHz. The frequency-dependent ICR linear

approximation was characterized by its slope coefficient m_{ICR}. For the 10.6Gbps data

rate, linear equations were developed to relate m_{ICR} to channel BER, m_{ICR} to channel Q,

and m_{ICR} to channel output eye pattern height. It is shown that as the steepness of m_{ICR}

decreases, the BER decreases, the channel Q increases, and the channel output eye

pattern height increases.

5.2 Future Work

5.2.1 Connector Fixture for Study Beyond 10GHz

Since signaling rates in backplane applications are continually increasing with

20Gbps on the horizon, there is a need to understand connectors with lossy material at

higher data rates. To facilitate further study at higher data rates, a simplified connector

similar to the one used in this study may be created by modifying the current design. The

design of the connector fixture components limits the bandwidth of the study to less than

10GHz. The relatively large air gap of 0.625" between the SMTL connector return

conductors can support a transverse standing wave at 9.5GHz, thereby inherently limiting

the connector topology to 10Gbps and less. The impedance match of the connector

launches also present a channel bottleneck for data rates greater than 10Gbps, as shown

in the TDR plot of Figure 17. One way the launch could be improved would be to

gradually taper the signal conductors from the diameter of the SMA launch connector to

the larger SMTL connector signal conductor diameter.

5.2.2 Additional Nonferromagnetic Quasi-conductor Materials

Investigation of a larger sample set of quasi-conductor materials with bulk conductivity between 1.5 S/m and 1500 S/m is needed since Material A (45 S/m bulk conductivity) had the largest effect on reducing PSC and therefore reducing channel BER of the three materials impregnated with only carbon particles.

5.2.3 Usage of More Aggressive Lossy Materials for Smaller BER

By using materials that are capable of reducing crosstalk much more than was accomplished with the CRS-124 material, the relationship between m_{ICR} and BER or m_{ICR} and Q should be investigated at even lower BER values and higher channel Q values.

5.2.4 Channel Analysis Using More Bit Intervals

The present study performed channel analyses based on statistical values obtained from only approximately 5000 transmitted bit intervals. The computational software used for this study, MATLAB, is limited in its memory management capability to manipulate bit record lengths much longer than 5000 at the time waveform sample resolution of 5ps. Statistical data acquired from longer data records will help to determine if more bit intervals used will result in greater similarity of voltage state variances σ_0 and σ_1 (Table 5) and therefore more accurate determination of channel BER.

5.2.5 Agreement Between Calculated and Measured BER

While the BER of the connector experiments in this thesis was calculated using statistical values obtained from eye pattern data, the accuracy of this methodology should ideally be compared with measurement. High-end test equipment such as BERTScope is available on the market currently to measure the BER of backplane channels. BERTScope determines the BER of a channel by transmitting large numbers of bits through the channel at some data rate and checks the output waveform for corrupted bits. Since BERTScope does not have multiple data output ports available for generating asynchronous crosstalk interference, a methodology needs to be developed for measurement of channel BER with full asynchronous crosstalk interference from other signal conductors in the connector.

APPENDICES

APPENDIX A

COAXIAL RETURN CONDUCTOR RESONANCE

It can be demonstrated that parasitic resonance which degrades transmission

performance can exist in TEM transmission lines if the return conductor of the line is

longitudinally discontinuous such that a parasitic cavity is coupled to the transmission

line through an aperture. One specific example of this would be a mated coaxial SMA

connector with a parasitic annular cavity formed by improper tightening of the

connector's threaded mating nut. A properly mated SMA connector is shown in Figure

80.
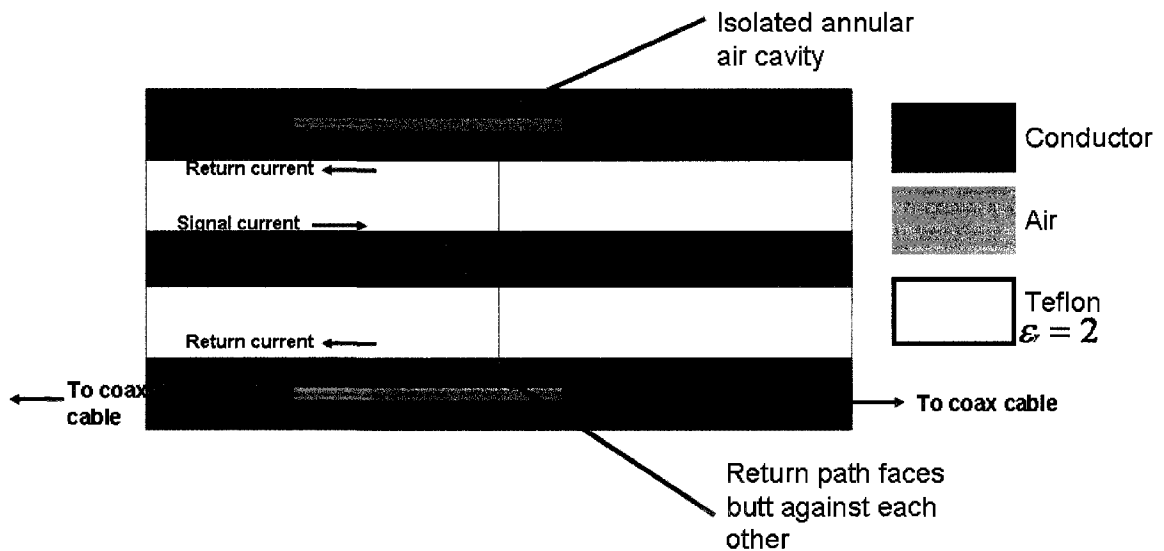
Figure 80: Schematic of a fully mated SMA connector.

Measurement of this connector shows maximum insertion loss of 0.56dB and

maximum return loss (reflection) of -16.7dB from DC to 20GHz when properly mated as

shown in Figure 81. When fully mated, an air cavity is isolated from the transmission

line since the faces of the return path conductors butt together.

Figure 81: Measured transmission (left) and reflection (right) magnitude transfer functions of a fully mated SMA connector.

If the threaded return conductor of the fully mated SMA is then slightly loosened while

the signal conductor remains mated, this loosening action subsequently exposes through a

gap the isolated air cavity to the space in the transmission line. The gap is formed since

the designed return conductor faces no longer butt against each other when the connector

is loosened as shown in Figure 82.
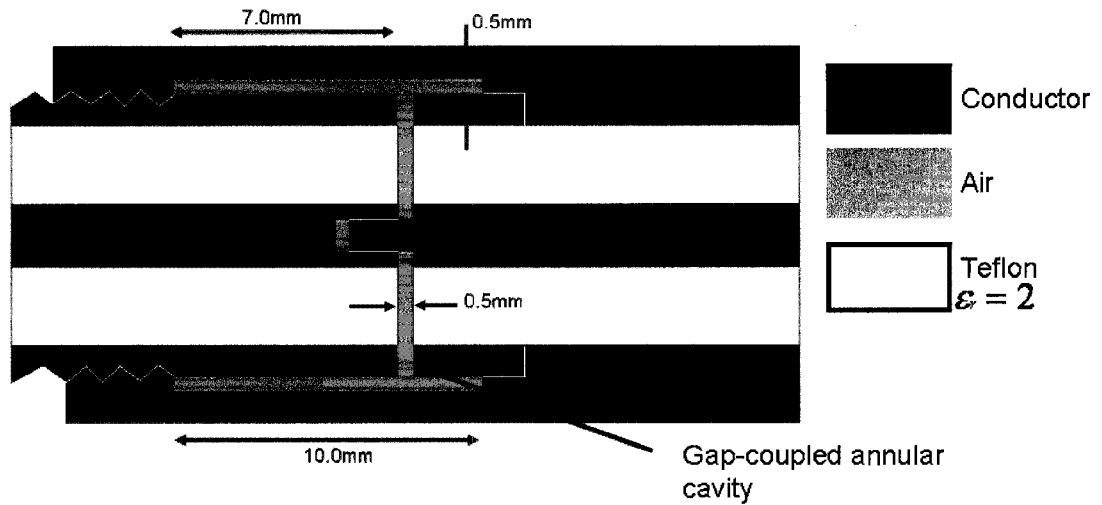
Figure 82: Schematic of an improperly mated SMA connector.

As a result of the gap-coupled annular cavity in the coax return conductor, transmission

and refection characteristics of the slightly demated connector exhibit resonant

characteristics as shown in Figure 83.

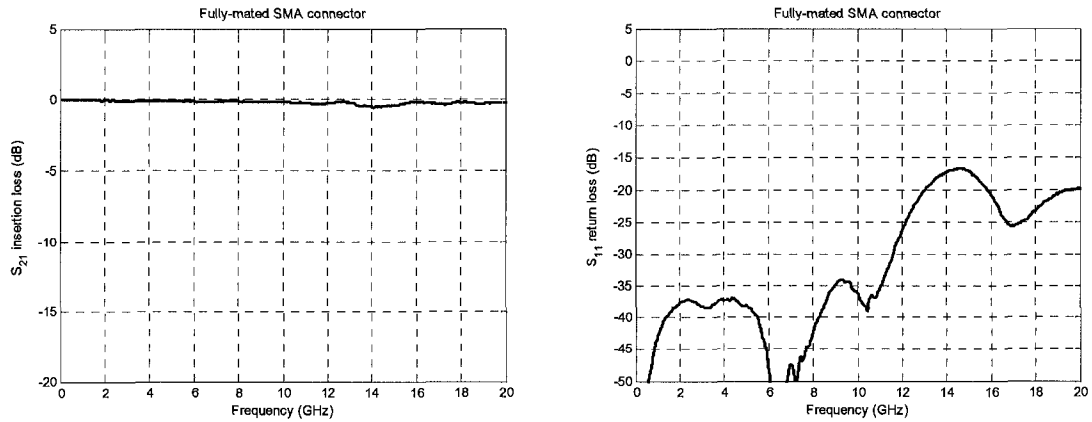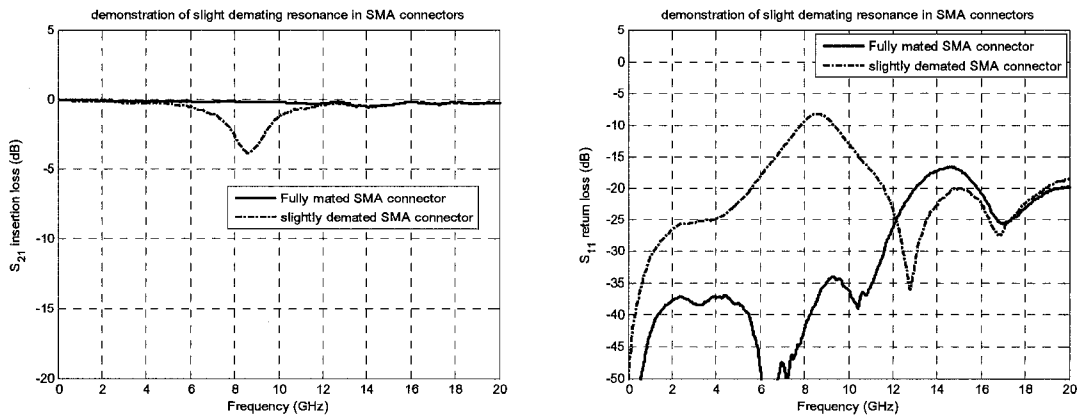**Figure 83: Measured transmission (left) and reflection (right) magnitude transfer functions of a fully mated SMA connector compared with an improperly mated SMA connector.**

CHARACTERISTICS OF MCS AND CRS-124 MATERIALS
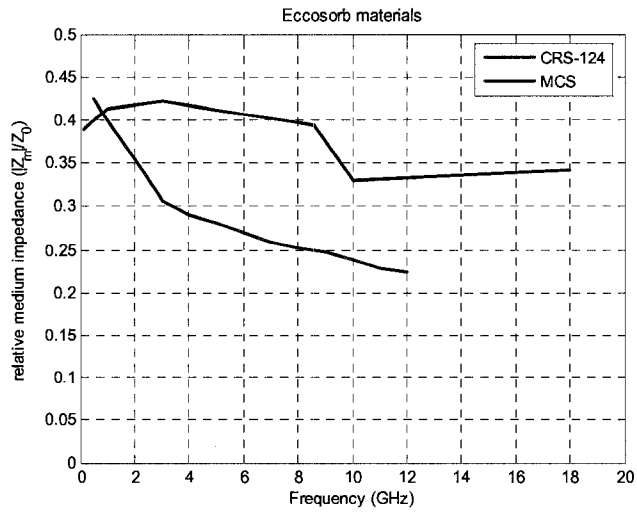
Figure 84: Magnitude of intrinsic impedance relative to free space for CRS-124 and MCS materials.
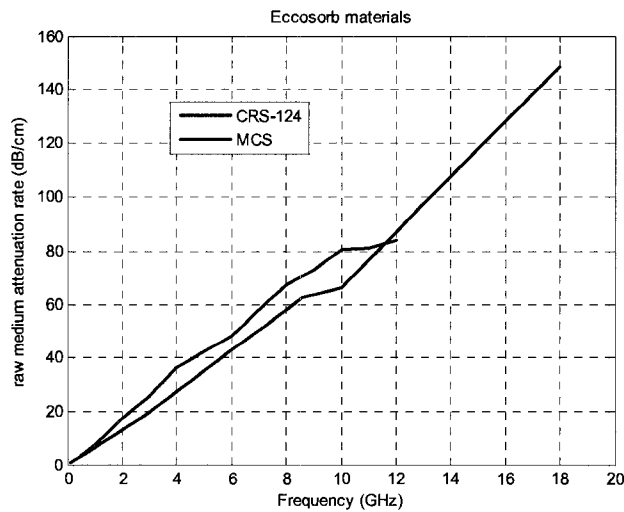
Figure 85: Attenuation rate of CRS-124 and MCS materials.
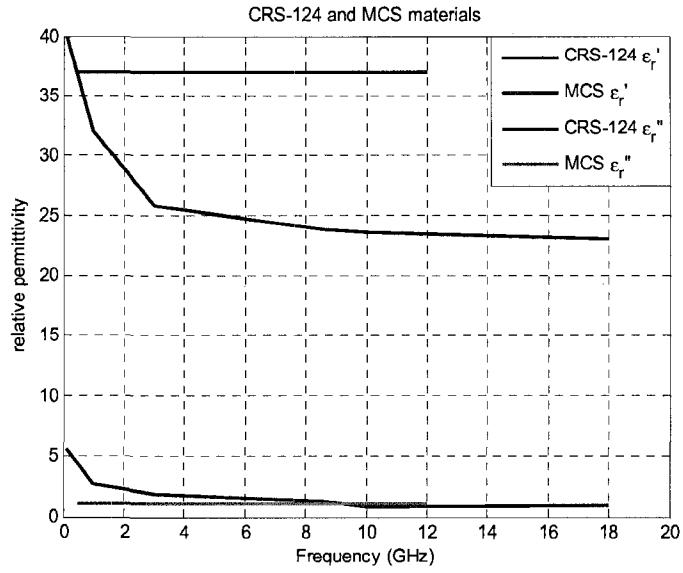
Figure 86: Complex permittivity values for the CRS-124 and MCS materials.
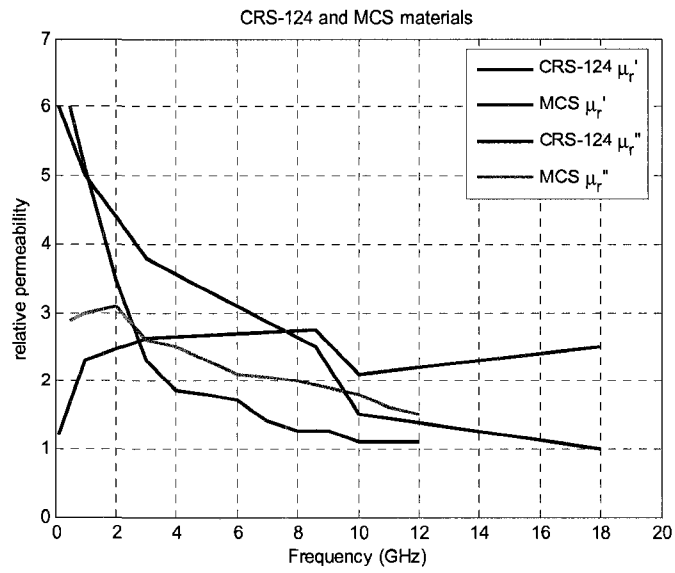
Figure 87: Complex permeability values for the CRS-124 and MCS materials.

105

APPENDIX C

VNA MEASUREMENT AND ASSUMPTION OF SYMMETRY

Since the experimental connector platform has a plane of geometrical symmetry,

most crosstalk data was acquired from enough ports to assume crosstalk symmetry about

the connector line of symmetry, where line 8 is the "victim" transmission channel of

interest for this connector. Complex frequency domain measurements were conducted

with an Agilent E8364B VNA. Assuming symmetry reduces the total number of

necessary measurements and removes unnecessary redundant measurement.
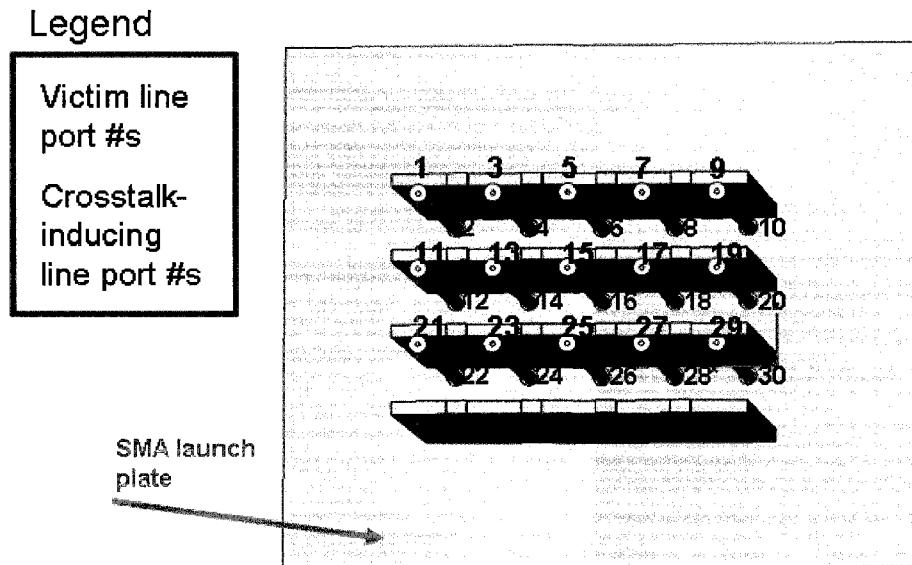
Figure 88: Diagram showing port numbers assigned to the transmission channel signal conductor line 8 and other signal conductors that induce crosstalk.
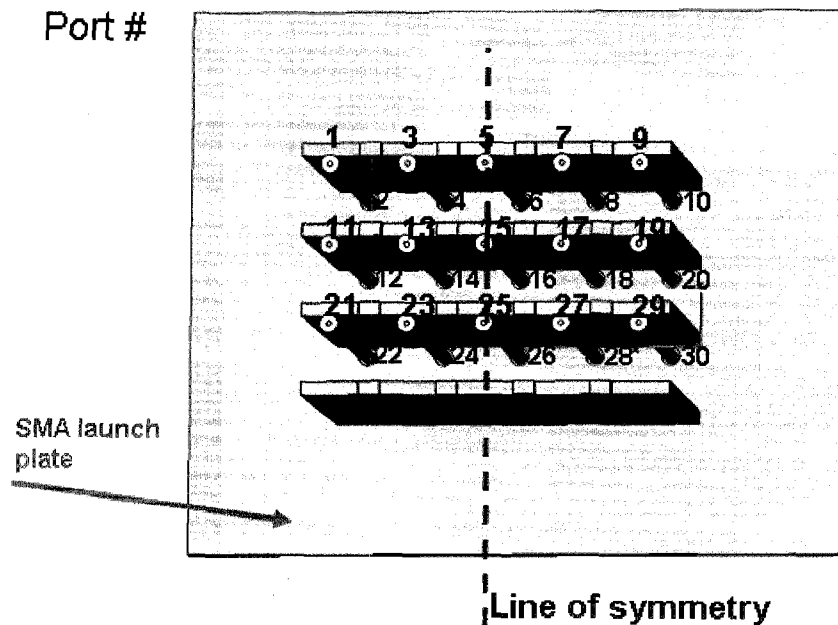
Figure 89: Diagram showing how many conductors are geometrically symmetric about line 8.

To examine the use of symmetry assumptions for measurements in the fixture and to expedite the measurement process, all S-parameters associated with an excitation port were measured in the baseline connector. Port 15, which is attached to line 8, was swept in frequency, and the response for all of the connector ports was recorded. S-parameters acquired from full-wave computer simulation of the connector were determined to be symmetric S-parameters due to sufficient mesh elements in the electromagnetic simulation, and the mesh structure is known to be geometrically symmetric in the simulator. S-parameters are based on an input power quantity of unity, and describe the response between measurement ports. A frequency-dependent audit of power delivered to all measurement ports based on S-parameter voltage quantities and constant system characteristic impedance from excited port 15 was determined from Equation C-1.

$$P.Audit = \sum_{n=1}^{30} \left| S(f)_{n,15} \right|^2 \tag{C-1}$$

If symmetry is assumed, then the audit of power is calculated with Equation C-2 where the crosstalk S-parameters are a function of frequency as numbered in Figure 87.

$$P.Audit = 2\left(\sum_{n=1}^{4} \left| S_{n,15} \right|^2 + \sum_{n=11}^{14} \left| S_{n,15} \right|^2 + \sum_{n=21}^{24} \left| S_{n,15} \right|^2 \right) + \sum_{n=5}^{6} \left| S_{n,15} \right|^2 + \sum_{n=15}^{16} \left| S_{n,15} \right|^2 + \sum_{n=25}^{26} \left| S_{n,15} \right|^2 \tag{C-2}$$

Comparison of the case where symmetry is and is not assumed in the baseline connector measurements shows little difference between the two methods of calculating the power audit, as shown in Figure 90. Therefore symmetry was used for measurement of all lossy material connector experiments to reduce the total number of measurements necessary to obtain all symmetric crosstalk terms since this determines that the two measurement methods are equivalent. It is worth noting that the power audit exceeds unity between 8GHz and 9GHz, which is not physical for a passive network. Possible explanations for this include error in the vector network analyser receivers, inaccurate mathematical characterisation of broadband SOLT calibration standards by the manufacturer in that frequency range, or standing wave constructive interference. Where the power audit falls below unity, it is assumed that the cumulative effects of conductor loss, Teflon dielectric loss in the launch SMAs, radiation loss, or destructive interference are the sources of loss in the power audit.
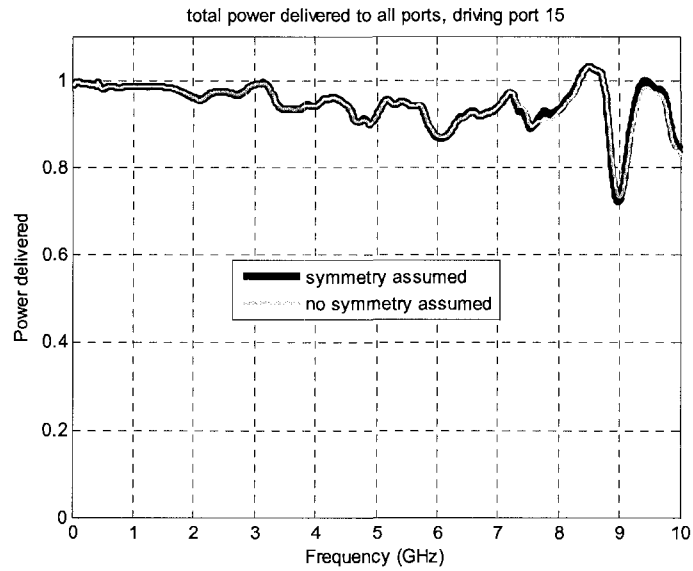
total power delivered to all ports, driving port 15

Figure 90: Power audit of the baseline connector shows the equivalence of assuming crosstalk symmetry with no assumption of symmetry.

APPENDIX D

CONSTRUCTION DETAILS OF SMTL CONNECTOR

There are several basic components involved with the construction of the SMTL connector structure used in this study. These consist of the following: a) the surface ground planes (feed plates) used to interface between measurement equipment and the connector structure, b) the connector return conductors with apertures for attachment to the surface ground planes, c) signal conductors used to deliver electromagnetic energy from one end of the connector structure to the other, d) SMA threaded female-female connectors used as vias to deliver signal energy from measurement equipment to the feed plates, and e) fastener hardware to join the components together into a connector assembly. Mechanical tolerances were designed to be held within ±0.001" of nominal shown in drawings.

In order to facilitate the transmission of electromagnetic energy into the SMTL connector structure for measurements, two identical 12" by 12", 1/8"-thick brass feed plates were machined to accept threaded female-female SMA adapters. The feed plates were machined to provide tight-tolerance holes used for the purpose of retaining and guiding 2-56 threaded pass-through fastener bolts for the purpose of attaching the connector return conductors to the feed plate surfaces. Identical attachment geometries of 2-56 threaded bolt guides and ¼"-36 threaded female-female SMA adaptors were geometrically repeated for 5 positions on the 12"x12" brass plates. Several additional ¼"-36 UNS 2B threaded holes were tapped through the feed plates for antenna measurements, but these holes were left unused. Finally, at the corners of the large brass launch plates, precision through-holes were machined to facilitate the attachment of four 3" length Delrin plastic standoffs with ¼"-20 fastener hardware, used to maintain additional mechanical rigidity of the connector structure. A mechanical drawing of the feed plates is shown in Figure 91.
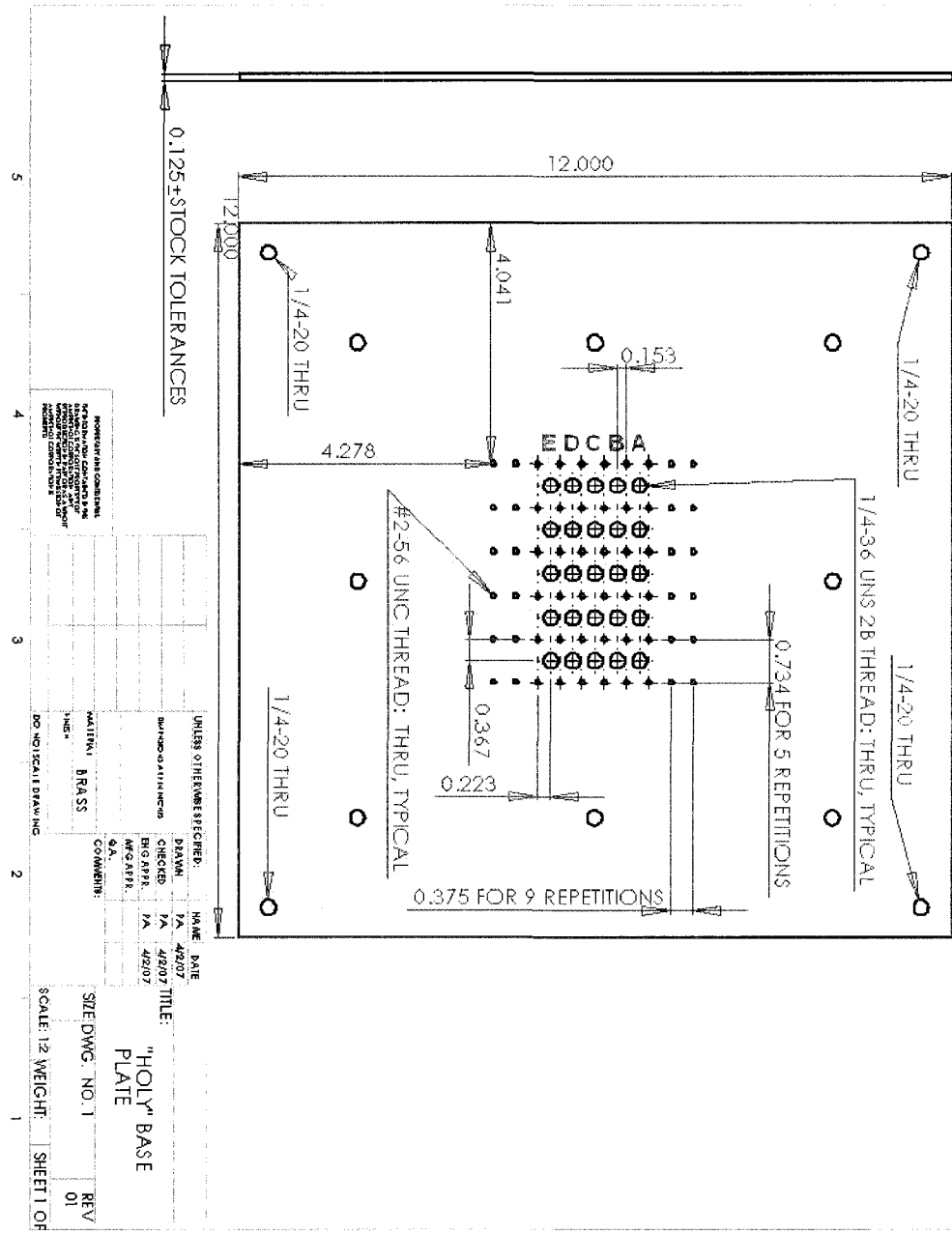
Figure 91: Mechanical drawing of the SMTL connector structure feed plates.

The SMTL connector structure return conductors were designed to be easy to remove from and replace into the fixture. Each return conductor was machined from 1/8"-thick brass sheet stock, measuring 3" x 3.5" in length and width dimension respectively, as shown in Figure 92.

Figure 92: Mechanical drawing of the SMTL connector return conductors.

Each return conductor has four evenly-spaced, 0.2"-wide discrete contacts along both of the 3.5" sides of the cross-shield, and were machined to be 0.050" tall. These discrete contact faces on the thickness dimension were then drilled and tapped with 2-56 threaded holes to accept fastener hardware. The 2-56 fastener hardware could then be tightened to result in the flush

112

butting of the 0.20"-wide return conductor contact points on the sample holders against the surface of the feed plates. The resulting attachment of these sample holders created the transmission line return path structures for the SMTL connector structure. The attachment of the return conductors to positions A through E shown in green lettering in Figure 91 define a connector stack. Each connector stack was designed to include two connector return conductors, a primary and a secondary return conductor. For this study, stack positions B and D were unused and skipped. The ¼"-36 UNS 2B threaded holes for stack positions B and D were populated with ¼"-36 threaded rod stock and made flush with the feed plate surface.

The signal conductors of the experimental fixture were constructed of 1/8" diameter circular copper tube, measuring 3.060" in length. Attachment pegs of 0.034" diameter were soldered to the ends of the 1/8" diameter copper tube signal conductors on the longitudinal axis of the copper rods, with 0.10" of length protruding from the ends. A diagram of the signal conductor dimensions is shown in Figure 93.

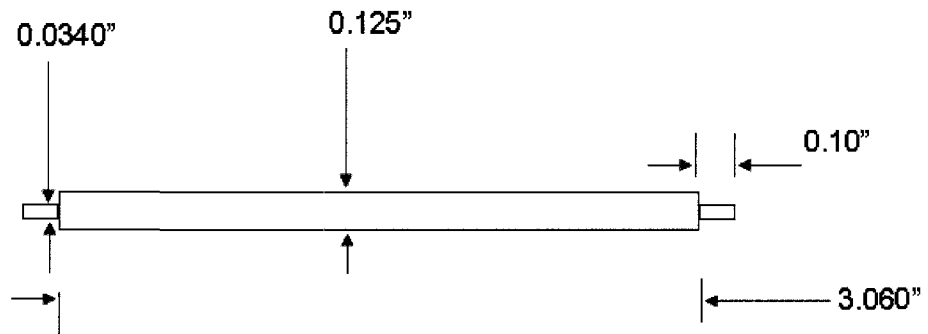**Figure 93: Dimensions of the SMTL connector signal conductors.**

The 0.034" diameter pegs facilitate the mating of the SMTL connector signal conductors with the female centre conductors of the SMA female-female adapters. The outer dimensions of the SMA adapters are shown in Figure 94. The SMA adapters were installed such that the SMA was flush with the feed plate surface as shown in Figure 95.
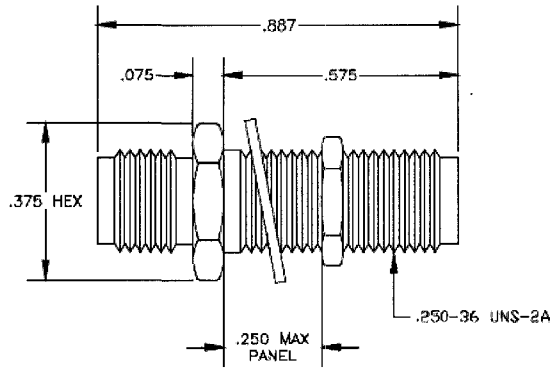
Figure 94: Outer dimensions of the SMA adapters.
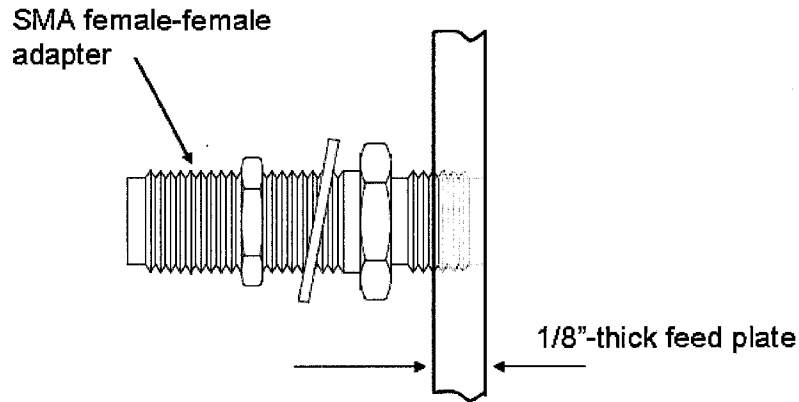
Figure 95: SMA connector is made flush with the surface of the feed plate.

After rigidly holding into place the SMTL return conductors with 2-56 threaded fastener hardware, the SMA adapters and signal conductors were then installed to form a 3-by-5 position SMTL structure in stack positions A, C, and E. A stack for this SMTL connector consists of five separate signal conductors with primary and secondary return conductors, as shown in Figure 14. Therefore the assembled SMTL connector consists of 15 signal conductors, 30 SMA adapters, 2 feed plates, 4 connector return conductors, and a full compliment of fastener hardware. The final assembly resembles the photographs of the SMTL connector structure shown in Figure 13.

APPENDIX E

VALIDATION OF FERRITE MATERIAL PROPERTIES

In order to experimentally verify the datasheet values of the CRS-124 and MCS

ferrite absorber materials, a coaxial discontinuity measurement fixture was created. The

measurement fixture consists of two, 2.0"-long halves of a 0.150" diameter outer

conductor coaxial air dielectric transmission line, and a 0.040"-thick coaxial discontinuity

lossy material sample holder that fits between the two halves when the coaxial fixture is

assembled. At each end of the assembled coaxial fixture are 0-80 threaded holes that

accept the fastener hardware footprint of a female field-replaceable bulkhead SMA

coaxial connector. In order to obtain a characteristic impedance of 50 ohms, the coaxial

center conductor is therefore a 4.040" length of 1/16" diameter copper tubing. A

photograph of the coaxial discontinuity fixture is shown in Figure 96.
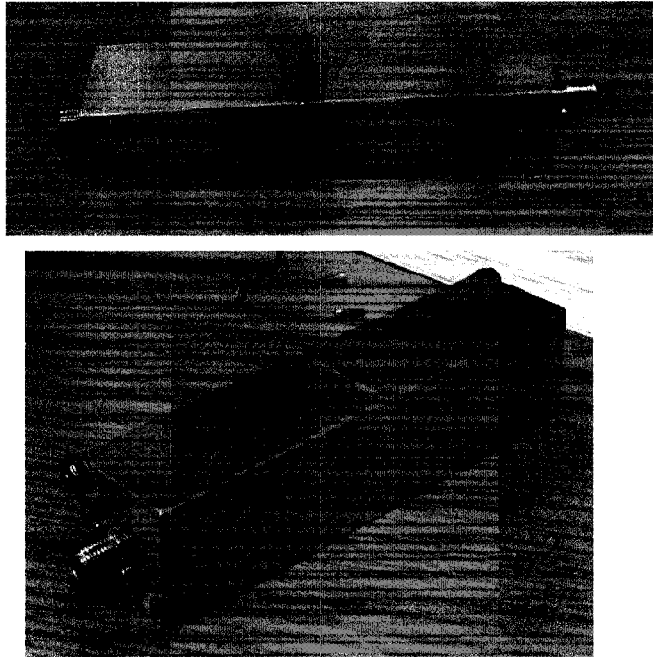
Figure 96: The coaxial discontinuity fixture (top) disassembled and (bottom) assembled.

The center conductor has 0.011" diameter steel wire pegs centered and soldered at the ends of the copper tube to facilitate insertion into the center conductors of the fixture field-replaceable bulkhead SMA connectors and allow the coax line to be measured.

Coaxial discontinuity samples that conform to the sample holder were cut from 0.040"-thick sheets of the ferrite materials using a custom punch and die set shown in Figure 97 (A). A material sample inside the sample holder is shown in Figure 97 (B). The measurement fixture half-assembled with the material sample holder is shown in Figure 97 (C).

116
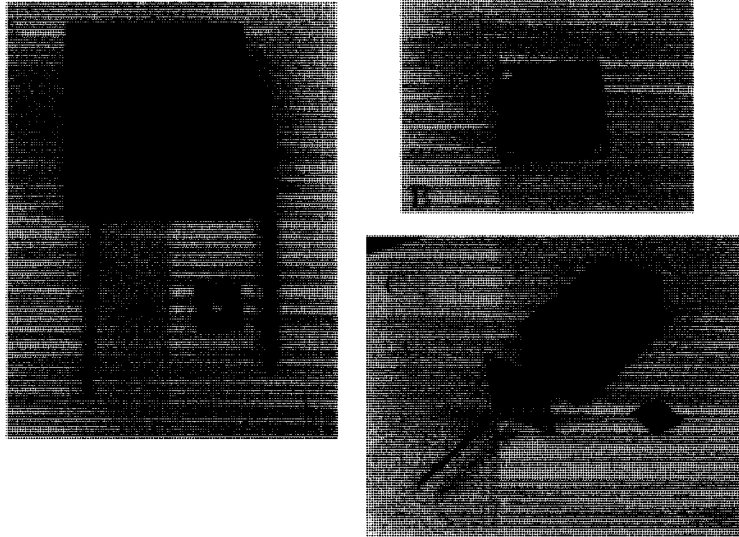
Figure 97: Photographs of (A) ferrite material punch set, (B) ferrite material discontinuity sample holder, and (C) partially-assembled coaxial discontinuity measurement fixture.

To approximately verify the material properties provided in the specification sheets for the CRS-124 and MCS ferrite materials, the insertion loss of the measurement fixture with no lossy material ($S_{21,air}$) was first measured, as shown in Figure 98.

Figure 98: Measurement of S_{21} for coaxial discontinuity fixture with no ferrite sample.

The frequency-dependent attenuation constant α_{DS} due to the ferrite material coaxial samples was then calculated using the complex permittivity and permeability values provided in the manufacturer datasheets and Appendix B. At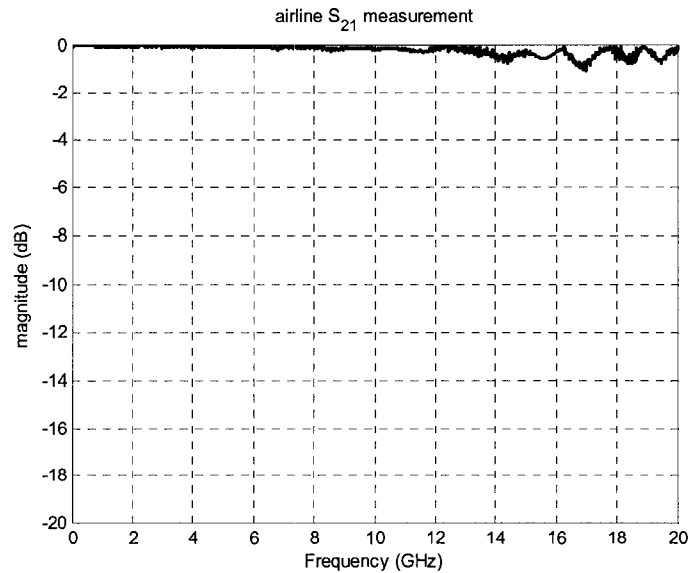tenuation due to the ferrite material datasheet values was calculated as $\exp(-\alpha_{DS})$ and cascaded with $S_{21,air}$ resulting in $S_{21,DS}$ (Equation E-1).

$$S_{21,DS} = S_{21,air} \exp(-\alpha_{DS}) \qquad\qquad\qquad (E-1)$$

The ferrite material samples were then individually placed in the coaxial discontinuity sample holder and S_{21} for each ferrite material was measured. Frequency-dependent plots comparing datasheet $S_{21,DS}$ and measured S_{21} with ferrite samples are shown in Figure 99 for the CRS-124 ferrite material and Figure 100 for the MCS ferrite material. This crude cascading method shows good agreement between the complex permeability and permittivity values provided in the material datasheets and measured loss due to the materials. The ripple in measured S_{21} (blue) in Figures 99 and 100 is a standing wave effect of the discontinuity in characteristic impedance created by the ferrite material samples.
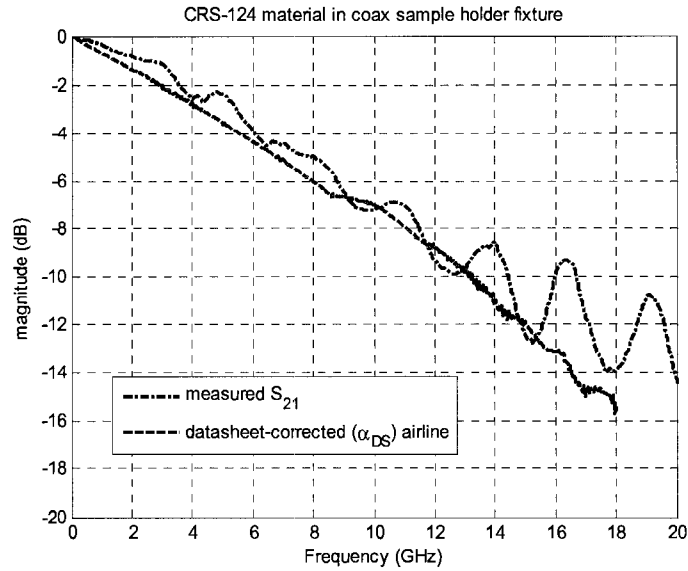
Figure 99: A graph comparing the magnitude of measured S_{21} (blue) to datasheet $S_{21,DS}$ values (green) for the CRS-124 ferrite material.
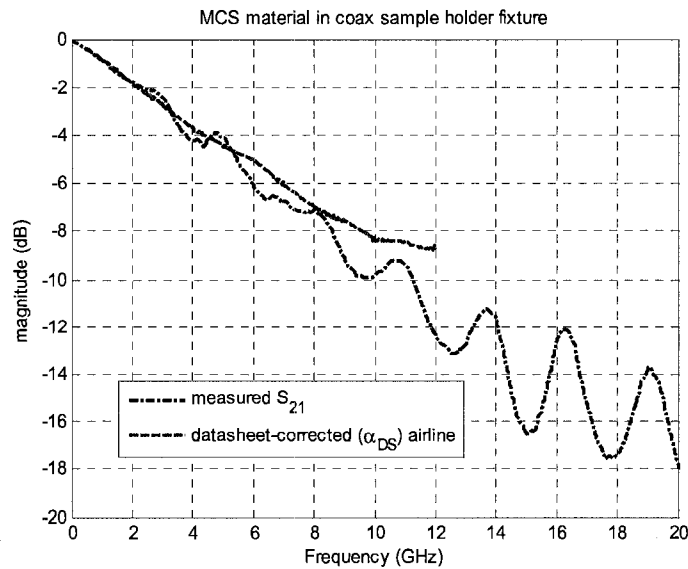

Figure 100: A graph comparing the magnitude of measured S_{21} (blue) to datasheet $S_{21,DS}$ values (green) for the MCS ferrite material.

LIST OF REFERENCES

[1] M. W. Gailus, " Interconnection system with improved high frequency Performance." U. S. Patent 6,786,771, September 7, 2004.

[2] W. S. Rothwell, "Complex Permittivity of Conductor-Dielectric Mixtures." IEEE Transactions on Microwave Theory and Techniques, Vol. 19, No. 4 (Apr 1971), pp. 413 – 414.

[3] I. J. Youngs, "Dielectric measurements and analysis for the design of conductor/insulator artificial dielectrics." IEE Proceedings – Scientific Measurement Technology, Vol. 147, No. 4 (Jul 2000), pp. 202 – 208.

[4] A. G. Gurevich, G. A. Melkov, Magnetization Oscillations and Waves. Boca Raton, FL: CRC Press, 1996, pp. 386 – 389.

[5] P. Lederer, C. Brewitt-Taylor, "Measurement of Microwave Properties of Magnetic Particulate Composites." IEE Proceedings – Scientific Measurement Technology, Vol. 147, No. 4 (Jul 2000), pp. 209 – 211.

[6] S. O. Kasap, Principles of Electronic Materials and Devices. New York: McGraw-Hill, 2002, pp. 721 – 724.

[7] A. J. Baden Fuller, Ferrites at Microwave Frequencies. London: Peter Peregrinus, 1987, pp. 14, 226 - 227.

[8] W. H. von Aulock, C. E. Fay, Linear Ferrite Devices for Microwave Applications. New York: Academic Press, 1968, p. 8.

[9] A. G. Gurevich, Ferrites at Microwave Frequencies. London: Heywood & Company, 1963, pp. 26 - 31.

[10] A. Von Hipple, Dielectric Materials and Applications. New York: Wiley, 1954.

[11] C. R Paul, Analysis of Multiconductor Transmission Lines. New York: Wiley, 1994.

[12] M. Gailus, M.A. Fusi, F. Zanella. "Electrical two and three dimensional modelling of high-speed board to board interconnections." WESCON/'95 Conference record 'Microelectronics Communications Technology Producing Quality Products Mobile and Portable Power Emerging Technologies, p 100, Nov. 1995.

[13] D. Jiao, A. A. Ergin, B. Shanker, E. Michielssen, J. Jin. "A Fast Higher-Order Time-Domain Finite Element-Boundary Integral Method for 3-D Electromagnetic Scattering Analysis." IEEE Transactions on Antennas and Propagation, Vol. 50, No. 9 (Sep 2002), pp 1192 - 1201.

[14] B. Ulrich. "Recent Developments in 3D Electromagnetic and Charged Particle Simulation." Vacuum Electronics Conference, 2007. IVEC '07. IEEE International, May 15-17 2007, pp 1 – 4.

[15] Z. Pantic, R. Mittra, "Quasi-TEM analysis of microwave transmission lines by the finite-element method." IEEE Transactions on Microwave Theory & Techniques, Vol. 34, No. 4 (Apr 1986), pp 1096 – 1103.

[16] J. Lo Vetri, D. Mardare, A.Z. Elsherbeni, C.E. Smith. "Full field and quasi-TEM time domain numerical analysis of coupled microstrip circuits." Antennas and Propagation Society International Symposium, Vol. 3, June 1995, pp. 1514 – 1517.

[17] A. E. Engin, W. John, G. Sommer, W. Mathis, H. Reichl. "Modeling of Striplines Between a Power and a Ground Plane." IEEE Transactions on Advanced Packaging, Vol. 29, No. 3 (Aug 2006), pp. 415-425.

[18] F. Broydé, E. Clavelier. "A New Method for the Reduction of Crosstalk and Echo in Multiconductor Interconnections." IEEE Transactions on Circuits and Systems – I: Regular Papers, Vol. 52, No. 2 (Feb 2005) pp. 405-415.

[19] T. Ciamulski, W. K. Gawarek. "On Eliminating Crosstalk Within Multiconductor Transmission Lines." IEEE Microwave and Wireless Components Letters, Vol. 14, No. 6 (Jun 2004), pp. 298-300.

[20] N. Kim, M. Sung, H. Kim, S. Baek, W. Ryu, J. An, J. Kim. "Reduction of Crosstalk Noise in Modular Jack for High-Speed Differential Signal Interconnection." IEEE Transactions on Advanced Packaging, Vol. 24, No. 3 (Aug 2001), pp. 260-266.

[21] T. Tarvainenn. "Simplified Modeling of Parallel Plate Resonances on Multilayer Printed Circuit Boards." IEEE Transactions on Electromagnetic Compatibility, Vol. 42, No. 3 (Aug 2000), pp. 284-289.

[22] N. Georgieva, Z. Chen, W. Oberhammer. "On Resonant Effects in Multilayer RF/Microwave Printed Circuit Board Applications." IEEE Transactions on Advanced Packaging, Vol. 22, No. 2 (May 1999), pp. 200 - 205.

[23] T. Yuasa, T. Nishino, H. Oh-hashi. "Simple Design Formula for Parallel Plate Mode Suppression by Ground Via-Holes." Microwave Symposium Digest, 2004 IEEE MTT-S International, Vol. 2 (June 6-11, 2004), pp. 641 – 644.

[24] L. W. Couch, Digital and Analog Communication Systems. Englewood Cliffs, NJ: Prentice Hall, 2001, pp. 479-484.

[25] D. Derickson. Fiber Optic Test and Measurement. Englewood Cliffs, NJ: Prentice Hall, 1997, p. 313.

[26] I. S. Ganga (Editor-in-Chief). <u>IEEE Draft P802.3ap / Draft 2.3</u>. Part 3 (December 4, 2006), pp. 193-4.

[27] K. Kurokawa. "Power Waves and the Scattering Matrix." IEEE Transactions on Microwave Theory and Techniques, Vol. 13, No. 2 (March 1965), pp. 194-202.

[28] R. Ramaswami, S. N. Kumar. <u>Optical Networks: A Practical Perspective.</u> San Francisco, CA: Kaufmann, 1998, p. 632.